2019

3D printed pneumatic soft actuators and sensors: their modeling, performance quantification, control and applications in soft robotic systems

Charbel Y. Tawk
University of Wollongong

3D PRINTED PNEUMATIC SOFT ACTUATORS AND SENSORS: their modeling, performance quantification, control and applications in soft robotic systems

BY
CHARBEL Y. TAWK
B.E. in Mechanical Engineering

DISSERTATION
Submitted in partial fulfillment of the requirements
for the Degree of Doctor of Philosophy in Soft Robotics

University of Wollongong, Australia
School of Mechanical, Material, Mechatronic and Biomedical Engineering

ARC Centre of Excellence for Electromaterials Science
Soft Robotics for Prosthetic Devices

August 2019

Abstract

Continued technological progress in robotic systems has led to more applications where robots and humans operate in close proximity and even physical contact in some cases. Soft robots, which are primarily made of highly compliant and deformable materials, provide inherently safe features, unlike conventional robots that are made of stiff and rigid components. These robots are ideal for interacting safely with humans and operating in highly dynamic environments. Soft robotics is a rapidly developing field exploiting biomimetic design principles, novel sensor and actuation concepts, and advanced manufacturing techniques.

This work presents novel soft pneumatic actuators and sensors that are directly 3D printed in one manufacturing step without requiring post-processing and support materials using low-cost and open-source fused deposition modeling (FDM) 3D printers that employ an off-the-shelf commercially available soft thermoplastic poly(urethane) (TPU). The performance of the soft actuators and sensors developed is optimized and predicted using finite element modeling (FEM) analytical models in some cases. A hyperelastic material model is developed for the TPU based on its experimental stress-strain data for use in FEM analysis. The novel soft vacuum bending (SOVA) and linear (LSOVA) actuators reported can be used in diverse robotic applications including locomotion robots, adaptive grippers, parallel manipulators, artificial muscles, modular robots, prosthetic hands, and prosthetic fingers. Also, the novel soft pneumatic sensing chambers (SPSC) developed can be used in diverse interactive human-machine interfaces including wearable gloves for virtual reality applications and controllers for soft adaptive grippers, soft push buttons for science, technology, engineering, and mathematics (STEM) education platforms, haptic feedback devices for rehabilitation, game controllers and throttle controllers for gaming and bending sensors for soft prosthetic hands. These SPSCs are directly 3D printed and embedded in a monolithic soft robotic finger as position and touch sensors for real-time position and force control. One of the aims of soft robotics is to design and fabricate robotic systems with a monolithic topology embedded with its actuators and sensors such that they can safely interact with their immediate physical environment. The results and conclusions of this thesis have significantly contributed to the realization of this aim.

Acknowledgments

I want to thank my supervisors, Prof. Gursel Alici, Prof. Geoffrey M. Spinks, and Prof. Marc in het Panhuis, for their valuable guidance, precious time, support and constructive feedback throughout my Ph.D. journey.

I want to thank Dr. Rahim Mutlu and Dr. Vitor Sencadas for their time, help and support.

I want to thank the Australian Research Council and the ARC Centre of Excellence for Electromaterials Science (ACES) for offering me a full scholarship to undertake this fundamental research.

I want to thank my parents, Youssef and Therese, for their tremendous support throughout my journey and for all the sacrifices they made throughout the years. Mom and Dad, I love you and thank you for everything. I want to thank my two brothers, Amin and Dany, for their love, support, and presence every time I needed help and guidance. I want to thank my two sisters, Judy and Mary, for their love and kindness. I want to thank my uncle and aunt, Assaad and Mona, for their tremendous love and support throughout the years. I want to thank Nour, Sayed, and Hala for their love and for always being there for me. I want to thank our beautiful angel, Sayde, for her unconditional love. You are in a better place now watching over us; we love you. I want to thank Miriam, my first cousin and my best friend, for everything and for always being there for me.

I want to thank my grandmother, Najiah, who taught me through her life how to remain a loving, caring, humble, optimistic, responsible, and resilient person despite all the hardships I encounter in life.

I want to thank my best friend and brother, Issa Ayoub, for his tremendous love and care and for always being there as a mentor, friend, and brother. I want to thank my friend, Ghostine Tawk, for motivating me to start exercising and to take care of my health by following a healthy diet from the beginning of my Ph.D.

Peer-Reviewed Articles

The following peer-reviewed articles and conference papers are based on the work presented in this dissertation.

[1]. C. Tawk, M. in het Panhuis, G. M. Spinks, and G. Alici, "Bioinspired 3D Printable Soft Vacuum Actuators for Locomotion Robots, Grippers and Artificial Muscles," *Soft Robotics,* vol. 5, no. 6, pp. 685-694, 2018.

[2]. C. Tawk, M. in het Panhuis, G. M. Spinks, and G. Alici, "Soft Pneumatic Sensing Chambers for Generic and Interactive Human–Machine Interfaces," *Advanced Intelligent Systems,* vol. 1, no. 1, p. 1900002, 2019.

[3]. C. Tawk, G. M. Spinks, M. in het Pnahuis, and G. Alici, “3D Printable Linear Soft Vacuum Actuators (LSOVA): their modeling, performance quantification and application in soft robotic systems,” *IEEE/ASME Transactions on Mechatronics*, vol. 24, no. 5, pp. 2118-2129, 2019.

[4]. C. Tawk, G. M. Spinks, M. in het Pnahuis, and G. Alici, “A 3D Printed Omni-Purpose Soft Gripper,” *IEEE Transactions on Robotics*, vol. 35, no. 5, pp. 1268-1275, 2019.

[5]. C. Tawk, H. Zhou, E. Sariyildiz, M. in het Pnahuis, G. M. Spinks, and G. Alici, “Design, Modeling and Control of a 3D Printed Monolithic Soft Robotic Finger with Pneumatic Self-Sensing Chambers,” *IEEE Transactions on Robotics*, Under Review, 2019.

[6]. C. Tawk, G. M. Spinks, M. in het Pnahuis, and G. Alici, “3D Printable Vacuum-Powered Soft Linear Actuators,” in *Proc. IEEE/ASME International Conference on Advanced Intelligent Mechatronics*, Hong Kong, 2019, p.p. 50-55.

Certification

I, Charbel Y. Tawk, declare that this thesis, submitted in partial fulfillment of the requirements for the award of Doctor of Philosophy at the University of Wollongong, Australia, is wholly my work unless otherwise referenced or acknowledged. This document has not been submitted for qualification at any other academic institution.

Charbel Y. Tawk
21 August 2019

Table of Contents

List of Figures

List of Tables

Chapter 1

Introduction

1.1. Soft Robotics

Recent technological advances have had a remarkable impact on the field of robotics. Robots are becoming smarter and capable of performing more complex tasks autonomously. However, conventional robots are still limited to factories where they perform tasks requiring high precision, high accuracy, large forces, and high speeds [1]. These traditional robotic systems cannot operate safely alongside humans in unstructured environments [2]. To overcome these safety limitations, and to bring robots and humans together as task partners, a new paradigm in robotics has emerged to establish "soft" robots that can safely conform and interact with delicate environments better than rigid-bodied robotic systems [3]. Soft robots made of highly deformable and compliant materials are ideal for interacting safely with humans and operating in dynamic environments. The soft robotics field has expanded rapidly in recent years, during which many soft robots have emerged [4-6]. The development of these soft systems is inspired by soft biological structures such as elephant trunk, octopus arm, squid tentacles, and worms that are made primarily of compliant materials and liquids [7-9].

Soft robots have multiple advantages compared to conventional robotic systems [10]. First, soft robots are made of soft and compliant materials that make them safe to interact directly with humans and fragile objects and to operate in highly dynamic physical environments [11]. Second, soft robots are made of low-cost soft materials that make them accessible and affordable. Third, soft robots are made of soft monolithic bodies. Therefore, these systems require minimal or no assembly processes in some cases. Fourth, soft robots can be directly fabricated using various additive manufacturing technologies [12-15]. Fifth, soft robotic systems can be used and implemented in diverse robotic applications such as locomotion robots, grippers, artificial muscles, parallel manipulators, prostheses, robotic hands, and many others. Finally, the compliance of soft robots makes them ideal for handling extreme external mechanical deformations without any damage and for manipulating delicate and fragile objects without damaging them [16].

1.2. Soft Robotics Challenges

Ideally, a soft robot should be made primarily of soft materials. The structure, actuators, sensors, electronics, and power sources of such robots should be soft, deformable, and compliant, and if possible, they should be incorporated seamlessly in the same continuum body [10]. However, the realization of entirely soft robots is still a great challenge for scientists and engineers [17-21]. Intensive research is being conducted to develop soft and compliant structures, central controllers, power supplies, sensors, and actuators for soft robots. For instance, soft materials such as silicone and other elastomers are being used to form the structural shape of a robot [1, 22]. It has been demonstrated that central control units and sensing elements can be made stretchable and flexible due to advancements in the field of soft electronics [1, 23-25]. Also, electrical power derived from stretchable batteries is progressing toward developing high energy density compliant power supplies that are suitable for soft robotic applications [26].

The development of soft and compliant actuators and sensors is the most critical challenge. Soft robots require soft actuators that can perform dexterous movements with favorable relative precision, sufficient forces, and fast and large reversible deformations. Moreover, these soft systems require robust, flexible, and stretchable soft sensors. Soft robots need stable soft sensors that can sustain large deformations repeatedly while providing useful and reliable data about their state and their external environment. These sensors are essential for developing reliable feedback control systems for soft robots.

1.3. Statement of Research Problem: 3D Printable Soft Pneumatic Actuators and Sensors

The objectives of this work are (i) to develop directly 3D printed and low-cost soft pneumatic actuators and sensors that can be integrated into diverse soft robotic applications [27-32], (ii) to optimize their geometric design before 3D printing, (iii) using finite element models to optimize and predict their behavior and to achieve the desired performance, and (iv) to experimentally quantify their performance to validate the numerical results obtained from the finite element models. Our aim is to directly 3D print soft robots with integrated actuation and sensing capabilities using low-cost and open-source 3D printers that employ soft and flexible commercially available materials.

The soft pneumatic actuators developed in this work are compatible with various 3D printable soft pneumatic actuators based on multiple additive manufacturing technologies [33-45]. This work presents novel 3D printable soft pneumatic sensing chambers to deliver a new class of soft 3D printed sensors to complement the soft pneumatic actuators proposed in this study and the already existing actuation concepts based on pneumatics and other actuation methods for soft robots.

1.4. Soft Actuators

Establishing the soft actuation concept and its realization is the first and most important step in building a soft robot. Soft robotic systems demand dexterous soft actuators, which can facilitate the adaptive interaction between the robots and their environments. Therefore, significant research efforts are dedicated to developing soft actuators and artificial muscles that can be used to articulate soft robots. To this aim, smart materials and structures such as shape memory alloys [46-50], dielectric elastomers [51, 52], ionic polymer-metal composites [53], coiled polymer fibers [54, 55], hydrogels [56, 57], humidity-responsive materials [58] and magnetic responsive structures [59] have been used to establish actuation concepts for soft robots. Chemical reactions such as combustion [60], electrolysis [61], and catalytic reactions [62] have been integrated within soft robots and soft structures as energy sources to drive them. Phase-change materials such as water [63] and wax [64] were also embedded in soft robotic systems to generate internal pressures. Soft structures, coupled with tendons and driven by electric motors, have also been used to develop underactuated and adaptive soft grippers [65, 66].

One of the most common actuation methods employed in soft robotics is pneumatics. There are several types of pneumatic actuators, including McKibben actuators [67], fiber-reinforced actuators [68-70], and PneuNets [71-73] that are activated using positive pressure. Various soft robots and soft structures are designed and actuated based on conventional pneumatic actuators [74-81].

There is also a group of soft pneumatic actuators that uses jamming as a mechanism for conformal gripping [82]. These jamming grippers are activated using a vacuum source instead of a positive pressure source as in conventional soft pneumatic actuators. Various soft pneumatic actuators that are activated using vacuum were recently developed for soft robotic applications [83-86]. Soft vacuum actuators have multiple advantages compared to positive pressure actuators. First, the actuators rely on negative pressure, which provides a fail-safe feature in contrast to conventional pneumatic actuators where the structure expands upon activation resulting in high stress gradients. Second, vacuum actuators shrink upon activation, which makes them suitable for applications where space requirements are limited. Finally, this actuation method improves the lifetime and durability of the actuators. All the soft vacuum actuators in the literature rely on sophisticated manufacturing techniques that require multiple steps to fabricate them [87].

1.5. Soft Sensors

Several types of soft sensors have been developed for soft robotic applications. However, most of these sensors require several fabrication steps before their integration in soft robotic systems. Resistive strain sensors including flex sensors [88, 89], conductive inks [90-92], ionic conductive liquids [93], liquid metals [24, 94, 95], fabrics and textiles [96, 97], resistive 3D printable thermoplastics [98], and ultra-thin piezoresistive sensors [99] combined with 3D printable soft monolithic structures [100] were developed to sense large deformations in soft robotic structures. Capacitive soft sensors were also established as pressure sensors [101, 102], tactile sensors [103], and strain sensors [104] for various soft robotic applications. Optical sensors were also developed for use in soft prosthetic hands as strain, curvature, texture, and force sensors [105].

Pneumatic sensors based on soft deformable structures have also been developed for numerous soft robotic applications, including human gait monitoring systems, soft grippers, tactile sensors, force and pressure sensors, soft interactive robotic structures, and active controls. An air bladder that can be embedded in a shoe to monitor and detect human gait phases was developed [106]. The air bladder was formed by winding a soft silicone tube that is connected to a pressure sensor. A soft pneumatic sensor for measuring the contact force and curvature in a soft gripper was fabricated using conventional molding and casting techniques that use commercial silicone rubbers [107]. A soft three-axis force sensor based on radially symmetric pneumatic chambers was designed for force measurement [108]. The sensor was also fabricated by casting silicone rubber. A tactile soft sensor for co-operative robots was demonstrated and built using a commercially available latex tube connected to a pressure sensor [109]. A method for rapidly prototyping interactive robot skins using 3D printing and analog pressure sensors was presented where different building blocks were designed to offer various modes of deformation, such as bending and twisting [110]. Similarly, 3D printed pneumatic controls based on the same printing method were developed for use in haptic feedback applications [111].

In these previous studies, the 3D printed soft pneumatic structures were fabricated using high-cost 3D printers and flexible materials with limited performance in terms of deformation. The other pneumatic soft structures were built using either conventional casting and molding techniques to develop soft robots [87] or using commercially available flexible and stretchable silicone tubes. The other types of sensors integrated into soft robotic structures are usually limited by hysteresis, drift over time, nonlinearity, cross-talk, short lifetime, or slow response.

1.6. Significance of 3D Printability

The use of conventional manufacturing techniques that involve multiple fabrication steps to develop soft pneumatic structures is not time-efficient and limits the development of soft pneumatic actuators and sensors that can perform different functions based on complex geometric designs [87]. Alternatively, 3D printing technologies can be used to directly 3D print soft actuators and sensors and to prototype various designs rapidly and efficiently. Also, 3D printing can be used to program the motion of soft actuators [38], produce soft robots with diverse capabilities [35], and control the elasticity of soft and complex structures [112]. There are several additive manufacturing techniques including 3D printing based on fused deposition modeling (FDM) [27, 33, 34], stereolithography [37], silicone 3D printing [38, 113], and multi-material 3D printing [35, 114]. FDM is the most affordable, accessible, and easy to use technology among all available and developed 3D printing technologies. This 3D printing method aligns with our aim of developing low-cost, accessible, and programmable soft actuators and sensors that can be integrated into diverse soft robotic applications.

FDM 3D printing has several advantages compared to other 3D printing technologies. First, FDM 3D printers are commercially and widely available. Second, these low-cost, affordable, and accessible 3D printers are capable of printing different materials with different colors, mechanical properties (i.e., soft and hard materials), and functions (i.e., soluble support materials, conductive materials, magnetic materials, and reinforced materials) simultaneously. Third, most of these printers are open-source, which means that they can be modified to meet specific printing requirements. Finally, these printers can be operated using various 3D printing slicers that are freely available. This approach of using FDM 3D printers will democratize soft robotics and lead to a greater spread and impact of these emerging technologies.

1.7. Contributions

The principal contributions of this thesis are:

- It proposes directly and rapidly 3D printed bending and linear soft actuators that can be activated using negative pressure and it demonstrates the potential use of these actuators in various soft robotic applications including locomotion robots (i.e., walking robots, hopping robots, and crawling robots), adaptive grippers, artificial muscles, parallel manipulators, prosthetic hands, prosthetic fingers, and modular robots.

- It proposes directly 3D printed soft pneumatic sensing chambers that have a very fast response to any change to their internal volume under four main mechanical input modalities of compression, bending, torsion, and rectilinear displacement, and it demonstrates the potential use of these soft chambers in various soft robotic applications including soft wearable gloves for virtual reality applications and telecontrol of soft adaptive grippers, soft touch buttons for interactive soft robotic platforms for STEM education and haptic devices for rehabilitation, controllers and throttles for gaming applications and bending sensors for soft prosthetic fingers tracking and control.

- It proposes directly 3D printed soft monolithic robotic fingers with embedded soft pneumatic sensing chambers that can be accurately and directly controlled in terms of position and force using the feedback signals from the soft embedded chambers in the finger that act as position and touch sensors.

- It presents several soft robotic prototypes that can be efficiently printed, assembled, and built based on the proposed soft pneumatic actuators and sensors developed. Therefore, it extends the soft actuators and sensors presented to practical, accessible, affordable, and functional soft robotic technologies.

- It presents and describes how to directly 3D print airtight and functional soft actuators and sensors using low-cost and open-source FDM 3D printers without requiring post-processing and support material using an off-the-shelf soft and commercially available material.

- It presents accurate finite element and analytical models in some cases that can be used to accurately model, predict and optimize the performance of the soft pneumatic actuators and sensors proposed.

1.8. Organization of this Thesis

The remainder of this thesis is organized as follows:

Chapter 2 presents the design criteria and fabrication technique used to fabricate the soft pneumatic actuators and sensors proposed in this work. Also, it describes and explains the 3D printing parameters used in the 3D printing software along with some guidelines to obtain functional and airtight soft pneumatic structures. Finally, it presents the material model developed and implemented in the finite element simulations for the soft thermoplastic poly(urethane) (TPU) used to 3D print the soft structures. Chapter 3 and Chapter 4, also published in [27-29], present the fabrication, modeling, characterization, and applications of the developed soft bending and linear actuators. Also, Chapter 4 reports on a soft 3D printed omni-purpose soft gripper (OPSOG) [30] that is activated by the linear actuators proposed.

Chapter 5, also published in [31], presents the fabrication, modeling, characterization, and applications of the soft sensing chambers. Chapter 6, which is published in [32], presents the fabrication, modeling, characterization, and force and position control of the soft robotic monolithic finger with embedded soft pneumatic sensing chambers. Chapter 7 concludes the work presented and describes the future research work envisioned.

Chapter 2

Materials and Methods

2.1. Introduction

The computer-aided design (CAD) models are designed to 3D print functional airtight soft pneumatic structures in one manufacturing step without requiring support structures and post-processing. The minimum thickness of the thin walls involved in the soft pneumatic structures is optimized to obtain airtight prototypes. It is a significant challenge to fabricate airtight and thin-wall chambers, which can efficiently expand and contract under positive and negative pressures, respectively. For example, as presented in Chapter 4, the linear soft actuator with thinner walls (0.55mm) was able to sustain 80,000 actuation cycles before failure, which was approximately four times the lifetime of the linear soft actuators with thicker walls (0.68mm).

2.2. 3D Printing Technology

Low-cost and open-source FDM 3D printers are used to 3D print the soft pneumatic actuators and sensors developed.

2.3. 3D Printing Software and Parameters Optimization

A commercially available slicer, Simplify3D (Simplify3D, LLC, OH), is used to slice the STL files produced from the CAD models of the soft pneumatic structures. The optimized printing parameters, set in Simplify3D, are provided in each chapter separately.

Here, we briefly explain the optimized printing parameters provided in each chapter and suggest some guidelines to obtain 3D printed airtight and functional soft pneumatic structures using FDM 3D printing. The layer height is set to the minimum value supported by the 3D printers used, which was ideal for obtaining airtight structures and high-quality exteriors. The Coast at End option is activated to turn off the extruder before the end of a loop (i.e., printed line) to relieve any excessive pressure in the nozzle and, therefore, to ensure that no blobs accumulate at the end of each printed loop that might cause air gaps in the structures. The values of the retraction settings are set to ensure that no excess material is extruded due to excess pressure in the nozzle that might cause uneven printed layers and printed plastic residuals on the thin walls. The print speed is set to ensure that a consistent and continuous flow of plastic is preserved throughout the printing process. High printing speeds might lead to under extrusion since the printed material is soft. The first layer speed is set to a lower value compared to the actual printing speed to ensure that the first layer adheres to the heated bed. The first layer is the most critical, and its quality affects the whole printed part. Therefore, the bed must be accurately leveled, and the speed of printing must be adequate to obtain a consistent and complete first layer. The horizontal movement speed of the extruder is reduced to ensure that the extruder does not drift from its proper position. Any drift in the position of the extruder leads to shifted printed layers in the horizontal direction that can result in air gaps in the printed structures. The temperature is set to a value that is high enough to ensure that the printed layers are well bonded and fused to prevent any air gaps from developing between two consecutive ones. The heated bed temperature is set to ensure that the first layer adheres to the bed. High bed temperatures might lead to melting or softening the first few printed layers.

The cooling load is set to ensure that the extruded layers cool down and solidify immediately to prevent any sagging. When overhangs are present in a CAD model, the cooling load should be increased to avoid any thin walls or overhangs sagging. The infill overlap value is dramatically increased so that the shells and the infill are well fused. The Perimeter Only option for External Thin Wall Type is activated to account for any thin walls printed. The value of the Perimeter Overlap is increased to avoid any separation and air gaps between two printed shells. Also, the Avoid Crossing Outline option is activated to prevent the nozzle from moving above and over the extruded outer shells where it might leave some plastic residuals that result in air gaps. Finally, the extrusion multiplier is increased to account for any inconsistencies in the diameter of the TPU filament.

2.4. Soft Material Characterization and Modeling

A commercially available soft TPU, known commercially as NinjaFlex (NinjaTek, USA), is used to 3D print the soft actuators and sensors. The stress-strain relationship of the TPU is obtained experimentally by conducting tensile tests. The TPU samples are prepared and tested according to the ISO 37 standard where the samples are stretched by 800% at a rate of 100mm/s using an electromechanical Instron Universal Testing machine (Instron8801). A TPU sample with its corresponding dimensions is shown in Fig. 2.1. Two types of samples are printed using two different infill patterns, crosswise and longitudinal, to assess the effect of the infill on the behavior of the TPU. The samples showed similar behavior, which proved that the infill pattern has a minor effect on the behavior of the TPU, as shown in Fig. 2.2 and Fig. 2.3.

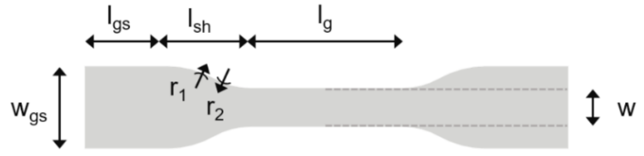

Fig. 8.1. TPU testing sample dimensions. l_{gs}:8.5, l_{sh}:8.5, l_g:16.0, w_{gs}:8.5, w:4.0, r_1:10.0, r_2:7.5. The thickness of the TPU sample is 2.0. All dimensions are in mm.

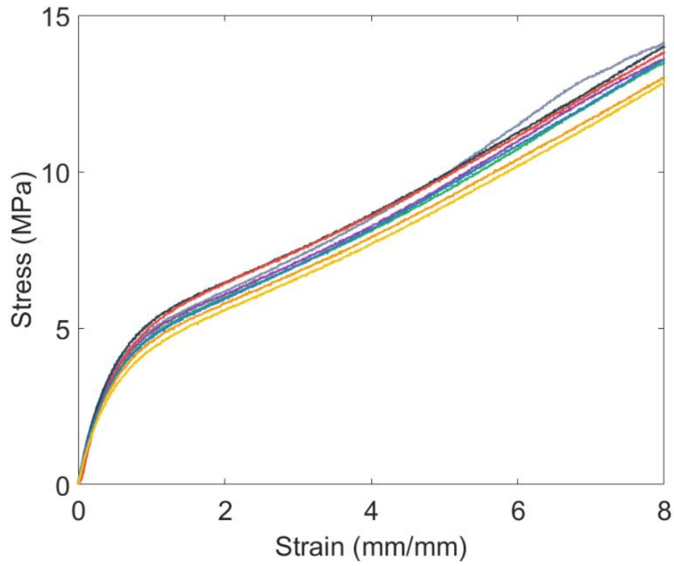

Fig. 8.2. TPU experimental stress-strain curves. Eight TPU samples printed with a crosswise pattern.

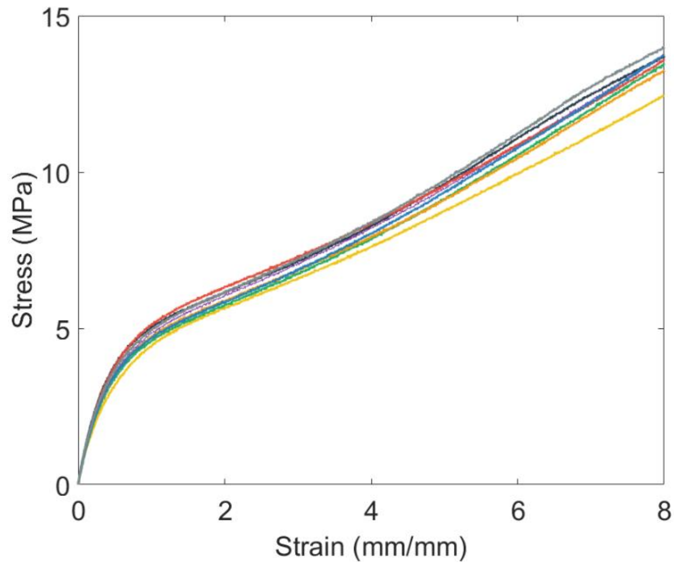

Fig. 8.3. TPU experimental stress-strain curves. Eight TPU samples printed with a longitudinal pattern.

The TPU is modeled as a hyperelastic material. The Mooney-Rivlin 5-parameter model is identified using the average experimental stress-strain curves of the TPU for both types of infill. The parameters of the hyperelastic material model are listed in Table 2.1. The model is implemented in ANSYS Workbench (ANSYS, Inc.), which provides various hyperelastic material models and curve-fitting tools. The material model is used in the finite element simulations of the soft actuators and sensors to predict their behavior and to optimize their performance by optimizing their geometric models efficiently.

Table 8.1. TPU Hyperelastic Material Model Constants

Hyperelastic Material Model	**Material Constant**	**Value (MPa)**
Mooney Rivlin 5-parameter	C10	-0.233
	C01	2.562
	C20	0.116
	C11	-0.561
	C02	0.900
	Incompressibility	0.000

Chapter 3

3D Printable Bending Soft Vacuum Actuators (SOVA)

3.1. Introduction

This chapter reports on the establishment of novel bioinspired 3D printable soft actuators that can be activated through vacuum, as shown in Fig. 3.1A and Fig. 3.1B. The actuation concept is inspired by the sporangium of the fern tree shown in Fig. 3.1E. More specifically, the actuation mechanism is inspired by the structure and function of the annulus of the sporangium. The thin outer walls of the annulus allow water to evaporate from the cells when the sporangium is exposed to air [115]. Consequently, the annulus bends, due to a negative pressure developed in each cell, which forces the radial walls to collapse [116]. These 3D printable actuators can achieve bending motion using the same principle when air is evacuated from each cell. When a negative pressure is applied to the internal chambers of the actuator, they shrink in volume, causing the actuator to bend, as shown in Fig. 3.2.

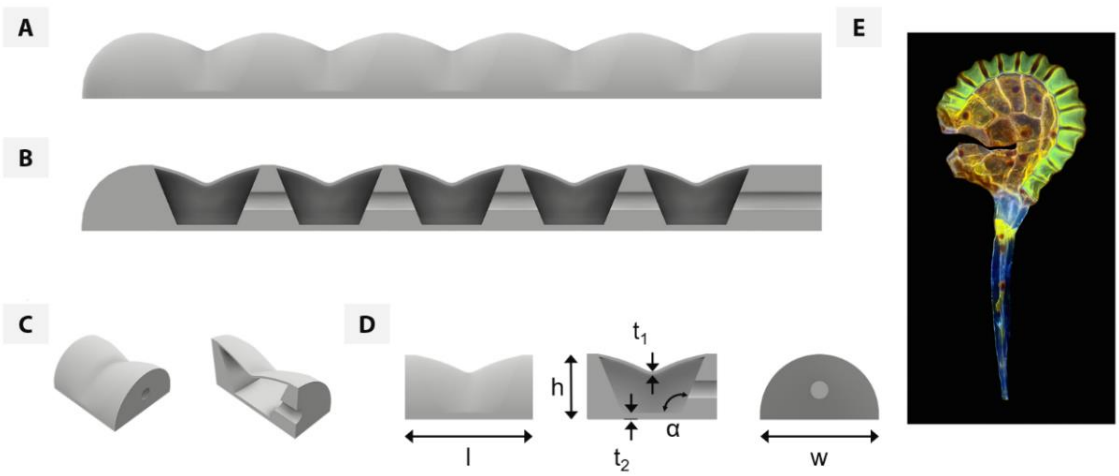

Fig. 9.1. Soft vacuum actuators (SOVA).(A) Soft actuator CAD model (B) Cross-sectional view of the soft actuator CAD model. (C) Pneumatic hinge CAD model (D) Pneumatic hinge dimensions: l: 22.0, h: 10.0, t_1: 1.0, t_2: 0.50, α: 112.5°, w: 20. All dimensions are in mm. The pneumatic hinges are connected through a 3.0mm diameter hole. (E) The annulus of fern sporangia [117].

These bioinspired soft actuators have many advantages. First, the soft actuators are fully 3D printed, which allows easy, efficient and rapid manufacturing and customization. Second, soft pneumatic hinges can be printed separately, which allows the realization of modular designs. The modular hinges allow the realization of soft actuators with multiple degrees of freedom and variable length. Third, two or more of such bending actuators can be connected in parallel to produce a linear actuator with a rectilinear stroke and a higher force output. Fourth, the actuation is accomplished through vacuum, which eliminates the possibility of burst and bulging as in conventional pneumatic actuators and, therefore increases the lifetime and reliability of the actuators. Finally, many soft and hybrid robots, grippers, and artificial muscles can be developed and activated using these soft vacuum actuators (SOVA).

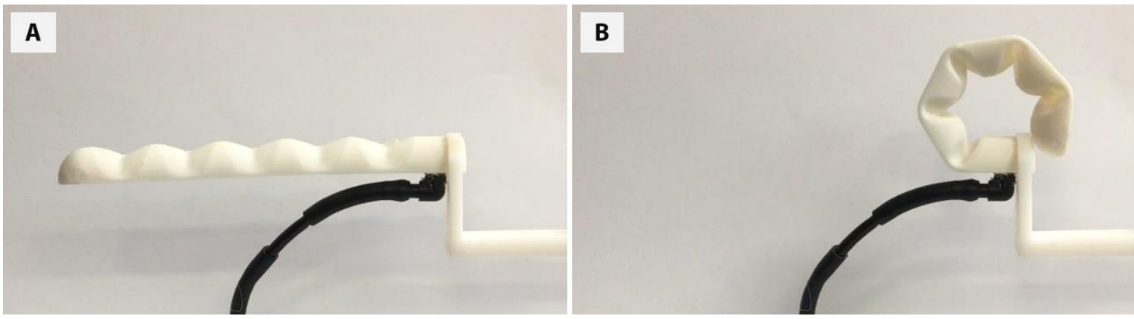

Fig. 9.2. Soft vacuum actuators (SOVA) activated prototype. (A) The initial position of the soft actuator before a negative pressure is applied. (B) The final position of the soft actuator after a negative pressure is applied.

3.2. Developing Bioinspired Soft Vacuum Actuators

The objective is to develop bioinspired 3D printable soft actuators that can be activated through vacuum. These soft vacuum actuators can be used in diverse soft robotics applications, including locomotion robots, grippers, artificial muscles, and modular robots.

3.3. Modeling and Fabrication

The first step is to model a 3D dimensional CAD model of the SOVA that is inspired by the annulus of the sporangium. The process started with modeling a single pneumatic hinge that bends under an applied negative pressure. The design of a single hinge is very critical. A series of designs are modeled, printed, and tested to ensure that the pneumatic hinges are airtight and could achieve a bending angle higher than 80 degrees under an applied negative pressure. The 3D CAD models of a hinge and an actuator are shown in Fig. 3.1. The geometries are modeled in SOLIDWORKS (Dassault Systèmes SOLIDWORKS Corp.). The actuators were 3D printed using an FDM 3D printer (FlashForge Inventor, FlashForge Corporation). To ensure that the printed hinges and actuators are airtight many printing parameters in the software were adjusted and optimized. It is important to note that the hinges and actuators are printed without supporting material and required no post-processing. Table 3.1 lists all the 3D printing parameters that were fine-tuned in the slicing software after many trials, along with their corresponding optimal values.

Table 9.1. Optimized printing parameters for 3D printing SOVAs.

Parameter	Value	Unit
Resolution Settings		
Primary Layer Height	0.1	mm
First Layer Height	0.09	mm
First Layer Width	0.125	mm
Extrusion Width	0.4	mm
Retraction Settings		
Retraction Length	3	mm
Retraction Speed	30	mm/s
Speed Settings		
Default Printing Speed	10	mm/s
Outline Printing Speed	8	mm/s
Solid Infill Speed	8	mm/s
First Layer Speed	8	mm/s
Temperature Settings		
Printing Temperature	240	°C
Heat Bed Temperature	35	°C
Cooling Settings		
Fan Speed	30	%
Infill Settings		
Infill Percentage	100	%
Infill/Perimeter Overlap	20	%
Thin Walls and Movements Behavior		
Allowed Perimeter Overlap	15	%
External Thin Wall Type	Perimeters Only	-
Internal Thin Wall Type	Allow Single Extrusion Fill	-
Avoid Crossing Outline	ENABLED	-
Additional Settings		
Extrusion Multiplier	1.15	-
Wipe Nozzle	DISABLED	-
Support Material	DISABLED	-

The thickness of each wall is chosen according to the movement of the sporangium. The outer walls are modeled as thin as possible (t_1: 0.5mm). The thick walls (i.e., ribs) are modeled to imitate the movement of the fern trees. The wall/cavity angle (α) is chosen based on the maximum bending angle upon activation with vacuum. The actuators are modeled with a wall thickness of 0.5mm and base thickness (t_2) of 1.0mm. A critical aspect of the modeling process is to make sure that the connecting ribs of the actuator are thick enough since they should rotate and not bend, which is a characteristic of the fern's sporangium [115, 116].

3.4. Finite Element Modeling

Finite element simulations are performed to simulate the deformation of the SOVAs under a negative pressure. The 3D modeled geometries are imported to ANSYS Design Modeler, where the holes connecting the internal chambers are ignored. Moreover, the thickness of the thin walls is adjusted to match the measured thickness of the walls of the 3D printed prototypes (0.70mm). A Static Structural Analysis is performed. The models are meshed using higher-order tetrahedral elements. In terms of boundary conditions, a Fixed Support is imposed at the base of the actuators, and a negative pressure is applied normal to the internal walls of the chambers. Also, frictional contact pairs are defined between the inner walls since they come into contact when the soft actuators deform under the applied load.

The finite element simulation results accurately predict the deformation and blocked force of the SOVA, as shown in Figs. 3.3 and Fig. 3.4. For the blocked force, the finite element results deviate from the experimental data (Fig. 3.8) at higher pressures. This difference in blocked force may be attributed to the slight movement of the force sensor in the experimental setup. The main advantage of finite element simulations is that they allow a user to iterate efficiently through multiple designs by varying geometrical parameters to optimize any design to achieve the desired performance.

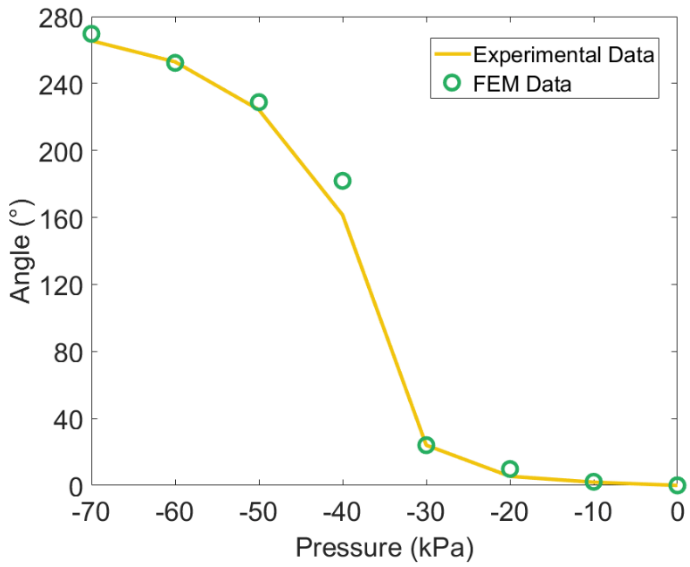

Fig. 9.3. Experimental bending angle and FEA bending angle of SOVA.

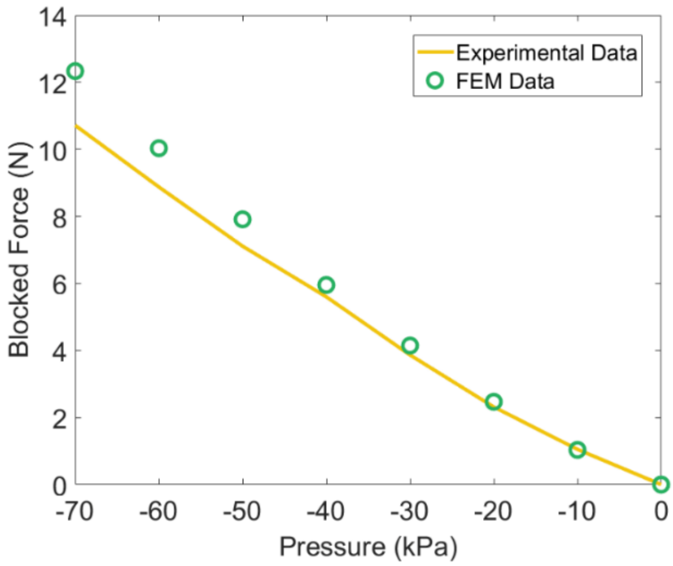

Fig. 9.4. Experimental blocked force and FEA blocked force of SOVA.

3.5. SOVA Characterization

3.5.1. Step Response

The step response of the actuator was obtained using a vision processing algorithm implemented in MATLAB (R2017a, The MathWorks, Inc., Natick, Massachusetts, USA) (Fig. 3.5). The algorithm tracks two red-colored dots on the tip of the actuator. The motion of the actuator was captured using a high-speed digital camera with a set frame rate of 500 frames per second (Phantom V611, Vision Research Inc.). The tip angle of the actuator was extracted from the video frames in MATLAB. The actuator rise time is $\tau_R = 132$ms, which is obtained from the step response data. The actuator shows a very fast response to an applied negative pressure (90% Vacuum). The time needed to return to the initial position is $\tau_{decay,1} = 62$ms. However, the actuator oscillates after reaching the initial position, and a decay time of $\tau_{decay,2} = 400$ms, was required for the actuator to settle.

3.5.2. Creep

The actuator was evacuated from ambient pressure for 30 minutes while the internal pressure of the system was measured using a vacuum pressure sensor (MPXV6115V, -115 to 0kPa, Gauge, and Absolute Pressure Sensor, NXP Semiconductors). The pressure changed by 2kPa, which was 2.82% of the original applied negative pressure. This change in pressure can be attributed to a slight leakage from fittings and connectors. These connectors are plastic tubes that connect the actuator to a pressure source. This slight leakage does not affect the results obtained since all the experiments are performed in a very short duration compared to holding the actuator activated for 30 minutes. Also, considerable optimization of the 3D printing conditions was required to achieve this degree of airtightness. The tip position of the actuator was also monitored to detect any drift from the original position with time. Despite the small loss of vacuum pressure, the position of the actuator remained almost unchanged with time, as shown in Fig. 3.5.

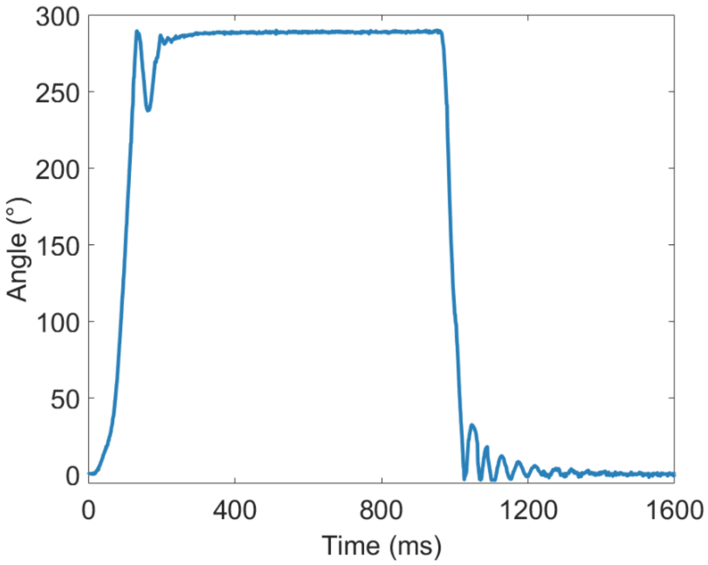

Fig. 9.5. Step response of SOVA.

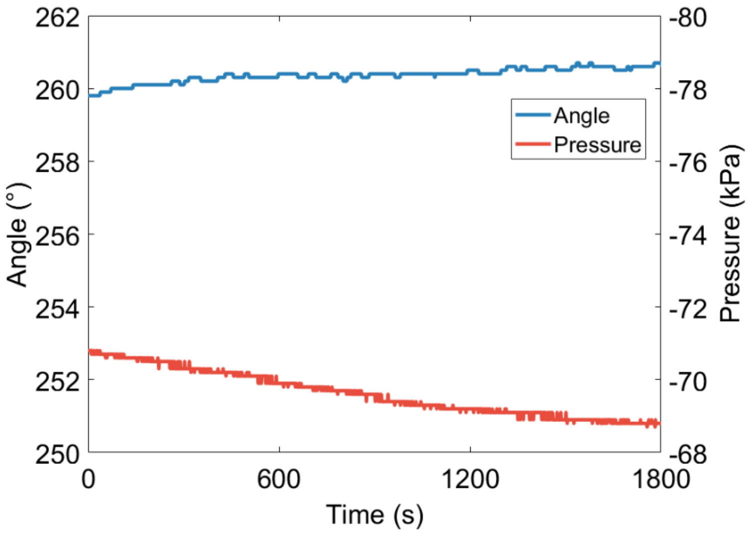

Fig. 9.6. Creep curve of SOVA.

3.5.3. Hysteresis

The tip angle of the actuator was monitored when the applied pressure was ramped up and down by a negative pressure of 10kPa in each step. The soft actuator exhibited hysteresis to a maximum extent of approximately 40% in regards to the tip angle at a pressure of -30kPa, as shown in Fig. 3.6. In the forward actuation phase, the actuator experiences buckling, which is one of the reasons for hysteresis. Enough vacuum is needed to overcome the stiffness of the thin walls. Once the thin walls buckle, the actuator bends forward and becomes highly sensitive to any further change in the pressure. This buckling behavior is shown in Fig. 3.7. In the forward actuation phase, when the pressure is ramped up, a steep trend in the bending angle of the actuator is observed between -20kPa and -50kPa. The second reason for hysteresis is the internal contact friction between the thin walls and the ribs.

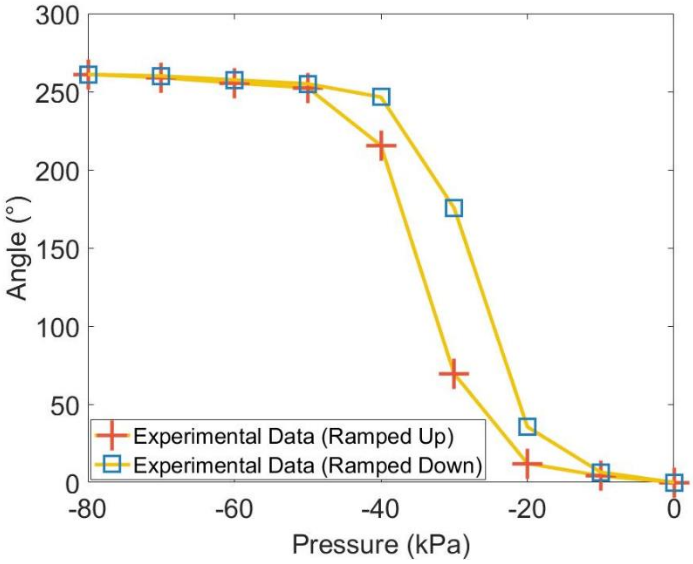

Fig. 9.7. Hysteresis curve of SOVA.

3.5.4. Repeatability and Durability

To assess the performance of the actuators in terms of lifetime, we have actuated a single hinge and a soft actuator consisting of 5 hinges to failure. The pneumatic hinge and soft actuator were activated using a diaphragm vacuum pump that can achieve 90% vacuum (Gardner Denver Thomas GmbH). The pneumatic hinge was actuated with a frequency of 1.50Hz where a bending angle of approximately 80° was achieved in each cycle, and the soft actuator consisting of 5 hinges was actuated with a frequency of 0.50Hz where a bending angle of 285° was achieved. An Arduino UNO microcontroller was used along with a solenoid valve to drive the actuator.

A single pneumatic hinge failed after Lt_{Hinge} = 130,000 cycles. The hinge was still airtight before failure, and no air leaks were detected. The hinge and actuator were inflated using a positive pressure input after they were submerged in a water medium to check for air leaks every 2000 cycles. In addition, no degradation in bending performance was observed since the hinge was still able to achieve the original bending angle upon actuation. Likewise, a soft actuator was actuated Lt_{Actuator} = 123,000 cycles until failure, and no degradation in performance was observed before failure. Therefore, the new actuation concept offers an advantage in terms of lifetime and reliability compared to conventional positive pressure pneumatic actuators [33, 37].

3.5.5. Blocked Force

The blocked force of the actuator (F_B) was measured using a force gauge (5000g, FG-5005, Lutron Electronic Enterprise CO., LTD). Two soft actuators were fixed facing each other to measure the blocked force. The two actuators generated $F_{B,\ Dual}$ = 31.41N under 90% vacuum, as shown in Fig. 3.8. Since the actuators are placed symmetrically, it can be concluded that a single soft actuator can generate $F_{B,\ Single}$ = 15.71N. In addition, the relationship between the force and pressure is nearly linear. The negative pressure was ramped up and down by a step of 10kPa, reaching a maximum negative pressure of -70kPa. The minimal hysteresis in the blocked force can be attributed to the fact that the actuator does not change shape (i.e., bend) in this specific setup (Fig. 3.9).

Usually, for positive pressure soft bending actuators, the tip force is measured and considered as the blocked force. However, this tip force does not reflect the actual blocked force of such actuators since they bend backward upon activation. This behavior decreases the maximum output force that can be achieved by such actuators. To overcome this limitation, we have designed the setup shown in Fig. 3.9, where the actuators are placed facing each other in a fixed position.

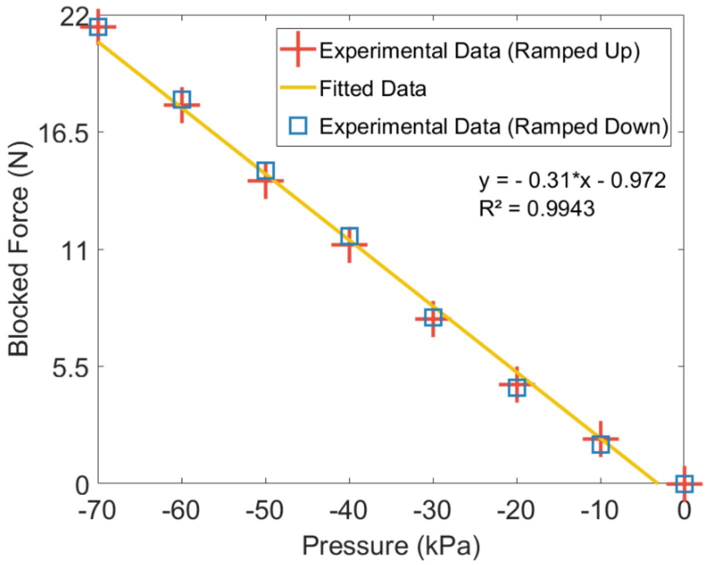

Fig. 9.8. Blocked force of SOVA.

3.5.6. Actuation Frequency and Bandwidth

The soft actuator achieved a maximum actuation frequency of f_{max} = 4.55Hz experimentally. A series of actuation frequencies were imposed on the actuator until it reached its limit. However, the bandwidth of the actuator is predicted to be ω_b = 5.45Hz. The actuator bandwidth was obtained by estimating a transfer function using the experimental step response data. Beyond the maximum experimental actuation frequency, the actuator did not have enough time to get back to atmospheric pressure and recover its initial position to confirm the estimated bandwidth of 5.45Hz. The actuation frequency is a very critical performance parameter. Soft actuators need to be fast enough for specific robotic applications that involve gripping and locomotion to achieve the desired performance. Therefore, these soft vacuum actuators can be tailored to applications that require high actuation frequencies. Also, SOVA showed significantly higher actuation frequencies compared to other vacuum actuators [83-85].

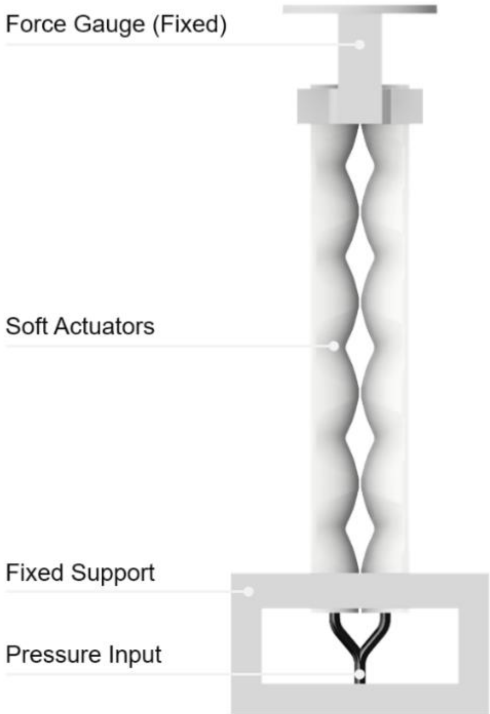

Fig. 9.9. SOVA blocked force experimental setup.

3.5.7. Payload to Actuator Weight Ratio

The weight of a single SOVA is $m_{actuator}$ = 13.14g. A single SOVA lifted m_{lifted} = 341.50g when a negative pressure of -90 kPa was applied. The actuator can approximately lift 26 times its weight.

3.6. Applications

The soft actuation concept developed can be used in a wide range of robotic applications such as grippers, locomotion robots, and artificial muscles. Furthermore, modular actuators can be realized by connecting a series of single negative pressure pneumatic hinges.

3.6.1. Soft Grippers

A three-finger gripper is built from three separate 3D printed SOVAs. The gripper grasps and picks up cups and different types of fruits, as shown in Fig. 3.10. These soft grippers can find applications in the food industry, where picking and placing fruits and vegetables is needed. The advantage is that no sensory feedback and position control are required since the actuators are highly compliant and naturally adapt to the geometry of the objects handled.

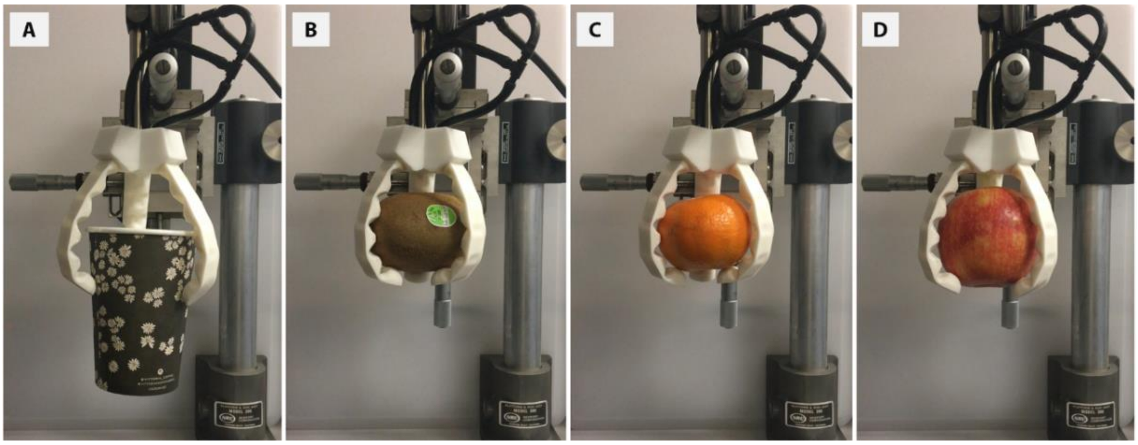

Fig. 9.10. Three-finger soft adaptive pneumatic gripper. The soft gripper grasping (A) a cup (11.13g), (B) a kiwi fruit (103.03g), (C) a mandarin (170.27g), and (D) and an apple (163.85g).

3.6.2. Walking Robot

A walking robot is fabricated and actuated using four soft legs, as shown in Fig. 3.11. Each leg is composed of two chambers. The main body of the actuator is made of 3D printed Acrylonitrile Butadiene Styrene (ABS) plastic. The robot can move forward, backward, and steer. In this scenario, the front and rear legs are actuated independently. Ideally, each leg should be actuated separately so that the robot can steer by actuating specific legs. The actuation was achieved by applying vacuum for 900ms and then returning the internal pressure of the legs to ambient pressure by opening a solenoid valve for a duration of 150ms. The robot can move with an average forward speed of v_f = 3.54cm/s which is v_{fb} = 0.25body−length/s.

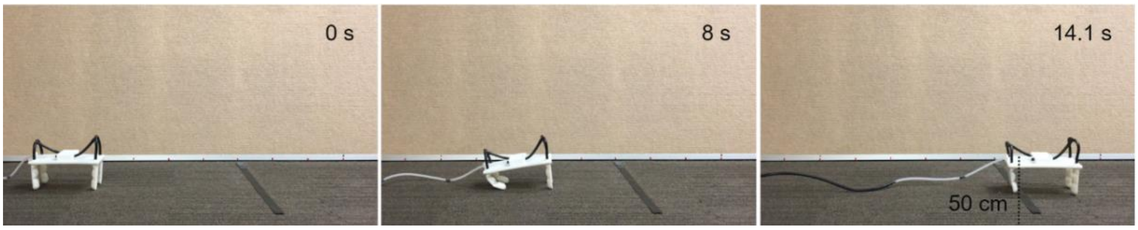

Fig. 9.11. Walking robot based on SOVA.

3.6.3. Hopping Robot ('Gongaroo')

A hopping robot, named Gongaroo inspired by our city of Wollongong and Australian kangaroos, is fabricated and actuated using two main legs, as shown in Fig. 3.12. The hopping is achieved by applying vacuum for 400ms to the legs and quickly returning their internal pressure to the atmospheric pressure through a solenoid valve that opens for 150ms. The average hopping speed of the robot is v_f = 3.75cm/s or v_{fb} = 0.39body−length/s.

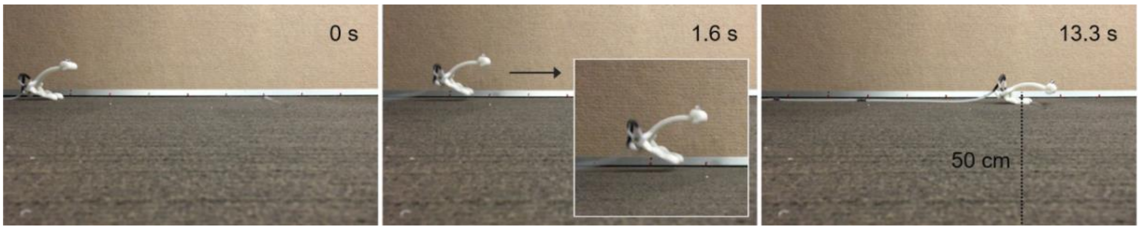

Fig. 9.12. Hopping robot, "Gongaroo," based on SOVA.

3.6.4. Artificial Muscle

Two SOVAs are used as an artificial muscle to rotate an elbow joint that moves an arm, as shown in Fig. 3.13A. The actuators are placed facing each other where their end is free to move. The top ends are connected to the vacuum tubes and the bottom ones to the link representing the forearm through tendons. The maximum angular stroke of the muscle is $\theta = 115°$ when no load is applied. It took 1.03s to reach the final position when vacuum was applied. In this specific scenario, the muscle lifted a mass of m = 28.48g by a height of h = 30cm.

3.6.5. Modular Actuators

One key feature of the SOVA is the capability to 3D print pneumatic hinges that allow the construction of modular SOVAs. The hinges can be attached using magnets, as shown in Figs. 3.13B and Fig. 3.13C. Solid links can be 3D printed from a wide range of materials, including ABS, Polylactic Acid (PLA), Nylon, and many others, depending on the desired application. These links can be used to separate the hinges by a desired distance, which can be useful for building robotic manipulators. Small rare-earth ring and rod magnets are inserted in the hinges to connect them. Here, we have demonstrated a soft actuator made of five hinges. The pneumatic hinges were connected using small plastic tubes. When negative pressure is applied, the modular actuator bend. The modular hinges can be designed in a way that each one can be actuated separately instead of being connected through plastic tubes to achieve multiple degrees of freedom. Therefore, the new actuation concept can be adapted to realize distinctive designs according to specific needs.

3.7. Discussion

Since soft robots are made of elastic materials, they cannot generate significant output forces when desired [118]. Furthermore, soft robots must be able to change their stiffness actively. Many variable stiffness concepts are reported in the literature where a soft actuation concept is coupled with a variable stiffness approach [118]. Although softness is an advantage, sometimes it stands as a limitation when high output forces are desired. However, our soft actuators serve the main objective of soft robots, which is softness and compliance. Also, they are well suited for applications where light and delicate objects are involved. The stiffness of the actuators can be controlled by integrating a variable stiffness approach along with the actuation concept.

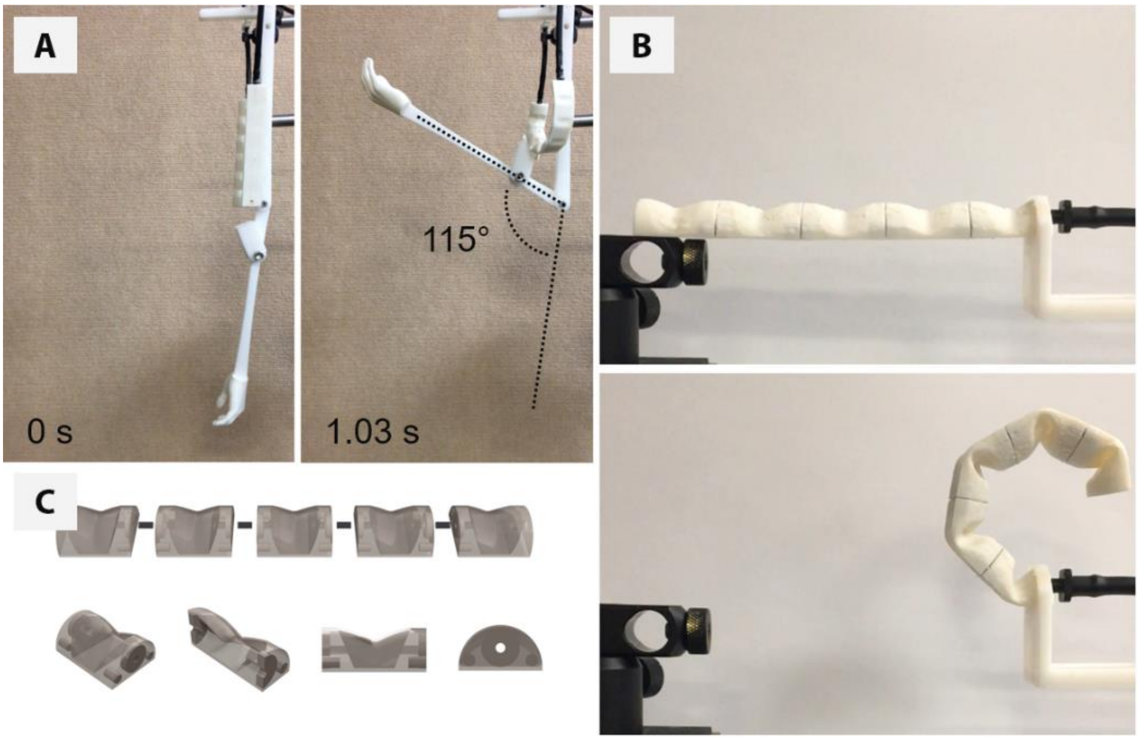

Fig. 9.13. Artificial muscles and modular robots based on SOVA. (A) Soft artificial muscle and elbow angular stroke. (B) Bending behavior of modular SOVA. (C) 3D CAD model of a modular actuator and a single modular hinge.

3.8. Conclusions

We have developed bioinspired soft pneumatic actuators, SOVA, that can be actuated using negative pressure. The actuators have four distinct advantages compared to conventional positive pressure soft pneumatic actuators. First, the actuators are fully 3D printed and customized according to specific applications. These actuators can be easily and rapidly manufactured using commercial and affordable FDM 3D printers. Second, they are safe and reliable since they have shown repeatability and a long lifetime. Maintenance and replacement costs can be significantly decreased since such actuators can undergo thousands of actuation cycles before failure.

Third, the concept can be used in a wide variety of robotic applications, including grippers, locomotion robots, and artificial muscles. Finally, they allow users to create modular designs of soft actuators by printing single pneumatic hinges separately.

Therefore, these actuators are suited for do-it-yourself projects where engineers, scientists, and hobbyists can print and operate them. Furthermore, the characterization of the actuators showed that they could achieve high actuation frequencies and generate significant output forces. These performance parameters are very critical since soft actuators are highly deformable and compliant. Additionally, the behavior of the actuators can be well predicted using FEM, which can significantly enhance the design and optimization process. Therefore, the newly developed soft actuation concept can play a significant role in the development of soft actuators for soft robots.

Chapter 4

3D Printable Linear Soft Vacuum Actuators (LSOVA)

4.1. Introduction

This chapter presents directly 3D printed soft actuators that generate a linear motion when activated with negative pressure, as shown in Fig. 4.1. These linear soft vacuum actuators (LSOVA) have multiple advantages compared to existing soft vacuum actuators. First, they can be easily and rapidly manufactured using an affordable open-source FDM 3D printer, without requiring any secondary manufacturing process or multiple manufacturing steps. Second, they generate high output forces. The actuators generate a blocked force of 27N and a lifting force of 26N upon activation with 95.7% vacuum, applied by a pump that can achieve this level of vacuum. Third, the actuators are scalable. The output force increases linearly with an increase in the internal volume of a single actuator. Moreover, there is a linear relationship between the output force and the number of actuators connected in parallel to a common output frame. It follows that multiple actuators can be used to amplify the output force for applications requiring a high force. Fourth, the actuators have a high actuation speed. The bandwidth of the LSOVA reported in this study ranges between 3.47Hz and 6.49Hz. Fifth, the behavior of the actuators can be accurately predicted using FEM and a geometric model. Sixth, the actuators remain functional, under a continuous supply of vacuum, after failure where their performance is not affected by minor air leaks or structural damage. Finally, the LSOVA can be used in different robotic applications such as soft navigation robots, soft parallel manipulators, artificial muscles, prosthetic hands, and adaptive grippers.

4.2. Modeling and Fabrication

The LSOVA actuators are designed with 3mm thick horizontal walls that separate the different vacuum chambers to prevent the structure from collapsing in the lateral direction, as shown in Fig. 4.1A. Samples are prepared with 1 to 5 vacuum chambers in series and are designated XC-LSOVA with X representing the number of vacuum chambers in each 3D printed linear actuator. The dimensions of LSOVA are shown in Fig. 4.1A and listed in Table 4.1. The printing parameters for LSOVA listed in Table 4.2 are optimized to obtain airtight actuators. The actuators were printed using an open-source FDM 3D printer (FlashForge Inventor, USA).

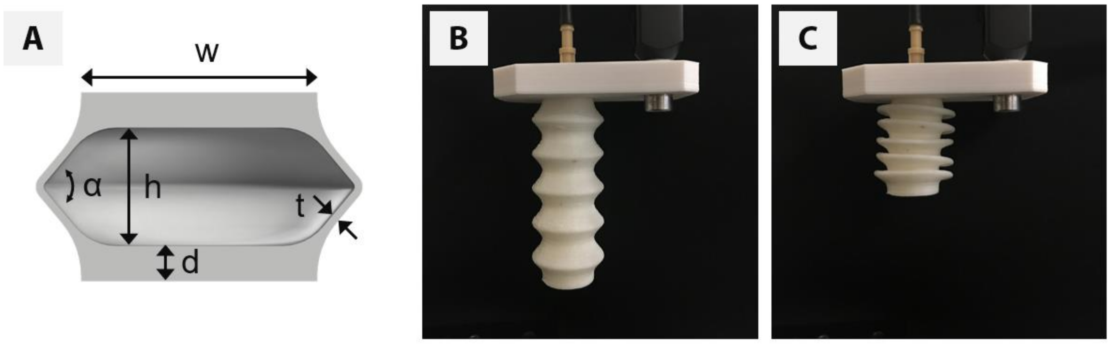

Fig. 10.1. Linear soft vacuum actuators (LSOVA). (A) The dimensions and the cross-sectional view of a 1C–LSOVA. w: 20, h: 10, d: 3.0, t: 0.90, α: 110°. These dimensions are the same for each cell of the actuator. All dimensions are in mm. (B) The initial position of a 5C–LSOVA when no vacuum is applied. (C) The final position of 5C–LSOVA when 95.7% vacuum is applied (Table 4.1).

Table 10.1. Performance parameters of LSOVA.

Parameter	1C– LSOVA	2C– LSOVA	3C– LSOVA	4C– LSOVA	5C– LSOVA
L_0	16.00	29.00	42.00	55.00	68.00
V_i	3922.72	7883.13	11843.55	15803.97	19764.40
m	3.16	5.27	7.49	9.46	11.09
δ	6.05	14.58	21.95	28.63	35.03
T_r	60.00	59.00	60.00	64.00	94.00
T_d	631.00	578.00	564.00	570.00	560.00
F_b	27.02	26.56	27.27	27.62	27.66
ω_b	6.49	5.91	5.62	4.69	3.47
L_t	21571	24981	23857	25046	22450
L_0: Original Length (mm), V_i: Internal Volume (mm^3), m: Mass (g), δ: Linear Deformation (mm), T_r: Rise Time (ms), T_d: Decay Time (ms), F_b: Blocked Force (N), ω_b: Estimated Bandwidth (Hz), L_t: Lifetime (Cycles).					

4.3. Finite Element Modeling

The soft actuators are meshed using higher-order tetrahedral elements. Both ends of LSOVA were constrained, and a negative pressure is applied to the internal walls. Also, frictional contact pairs are defined between the inner walls since they touch when the actuators deform. The blocked force and linear deformation of the actuators are predicted using FEM in ANSYS Workbench. The experimental blocked force data matches the FEM results with an acceptable difference of less than 5% in most cases, as shown in Table 4.3.

Table 10.2. Optimized printing parameters for 3D printing LSOVAs.

Parameter	**Value**	**Unit**
	Resolution Settings	
Primary Layer Height	0.1	mm
First Layer Height	0.09	mm
First Layer Width	0.125	mm
Extrusion Width	0.4	mm
	Retraction Settings	
Retraction Length	3	mm
Retraction Speed	30	mm/s
	Speed Settings	
Default Printing Speed	10	mm/s
Outline Printing Speed	8	mm/s
Solid Infill Speed	8	mm/s
First Layer Speed	8	mm/s
	Temperature Settings	
Printing Temperature	240	°C
Heat Bed Temperature	35	°C
	Cooling Settings	
Fan Speed	30	%
	Infill Settings	
Infill Percentage	100	%
Infill/Perimeter Overlap	20	%
	Thin Walls and	
Allowed Perimeter Overlap	15	%
External Thin Wall Type	Perimeters Only	-
Internal Thin Wall Type	Single Extrusion Fill	-
	Movements Behavior	
Avoid Crossing Outline	ENABLED	-
	Additional Settings	
Extrusion Multiplier	1.15	-
Wipe Nozzle	DISABLED	-
Support Material	DISABLED	-

There is a larger discrepancy between the experimental and FEM displacement results. The main reason for the discrepancy in the FEM and experimental displacement values is the presence of printing artifacts that reduced the linear displacement. The printed upper horizontal walls of the actuators are not clean and smooth. During the 3D printing process, the first few layers of each horizontal wall sag and fall due to the poor bridging performance by NinjaFlex, which results in thick plastic residuals that interfere with the linear displacement of the LSOVA.

To verify this hypothesis, a 1C−LSOVA was cut in half, and its interior walls were cleaned. Then, the cleaned 1C−LSOVA was glued back together, and its displacement was measured upon activation with 95.7% vacuum. The actuator displacement increased from 6.05mm to 8.57mm, which resulted in a difference of 0.93% when compared to the FEM. During the blocked force experiment, the walls of LSOVA remain undeformed since the actuators are restricted from moving (Fig. 4.7), which results in very accurate blocked force results.

The only challenge encountered was the distortion of some elements due to the large mechanical deformations. However, this issue was alleviated by incorporating a coarser mesh that is suitable for hyperelastic materials. The mesh used was selected to verify that the results are accurate and not affected by the mesh size. Therefore, FEM can be used to optimize the performance of LSOVA rapidly and efficiently.

Table 10.3. FEM results for LSOVA deformation and blocked force.

Parameter	1C– LSOVA	2C– LSOVA	3C– LSOVA	4C– LSOVA	5C– LSOVA
δ_e	6.05	14.58	21.95	28.63	35.03
δ_{FEM}	8.65	16.55	23.97	31.94	39.47
$\Delta\delta$	42.98	13.51	9.20	11.56	12.67
$F_{b,\,exp}$	27.02	26.56	27.27	27.62	27.66
$F_{b,\,FEM}$	28.30	28.49	28.59	28.56	28.66
ΔF_b	4.72	7.26	4.85	3.39	3.62

δ_e: Experimental Deformation (mm), δ_{FEM}: FEM Deformation (mm), $F_{b,\,exp}$: Experimental Blocked Force (N), $F_{b,\,FEM}$: FEM Blocked Force (N), $\Delta\delta$: Difference between δ_e and δ_{FEM} (%), ΔF_b: Difference between $F_{b,\,exp}$ and $F_{b,\,FEM}$ (%).

4.4. Analytical Modeling

We derived an analytical model to estimate the blocked force of the actuators. The free-body diagram of a 1C–LSOVA is shown in Fig. 4.2 and all the parameters of the model are listed in Table 4.4.

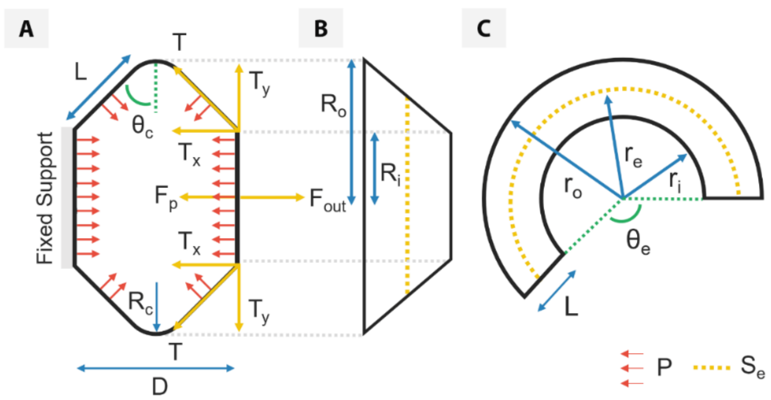

Fig. 10.2. Free-Body Diagram (FBD) of a 1C–LSOVA. (A) LSOVA FBD (B) Frustum side view (C) Flattened frustum.

Table 10.4. 1C−LSOVA analytical model parameters.

Parameter	Value
F_{out}	28.97
F_p	24.05
T_x	4.92
P	98.19
R_i	8.83
R_o	12.87
R_c	0.50
r_i	14.04
r_o	20.47
r_e	17.05
L	6.43
S_e	67.35
D	9.85
θ_c	50.00
θ_e	226.35

F_{out}: Output Force (N), F_p: Pressure Force (N), T_x: Thin Wall Horizontal Tension (N), P: Input Negative Pressure (kPa), R_i: LSOVA Inner Radius (mm), R_o: LSOVA Outer Radius (mm), Rc: Radius of Curvature (mm), r_i: Flattened Frustum Inner Radius (mm), r_o: Flattened Frustum Outer Radius (mm), r_e: Flattened Frustum Effective Radius (mm), L: Thin Wall Length (mm), S_e: Thin Wall Width (mm), D: Linear Stroke (mm), θ_c: LSOVA Angle (°), θ_e Frustum Effective Angle (°).

The output blocked force is expressed as:

$$F_{out} = F_p + 2T_x \tag{4.1}$$

where

$$F_p = \pi R_i^2 P \tag{4.2}$$

From Laplace's law, we can write:

$$T = R_c P S_e \tag{4.3}$$

where S_e is the effective width of the thin walls, which is computed by considering the flattened frustum shown in Fig. 4.2C.

The relationship between LSOVA inner and outer radii and the flattened frustum inner and outer radii is expressed as follows:

$$r_i = R_i L/(R_o - R_i) \tag{4.4}$$

$$r_o = R_o L/(R_o - R_i) \tag{4.5}$$

and the effective radius of the flattened frustum is computed from the following equation:

$$r_e = L/\ln(r_o/r_i) \tag{4.6}$$

The effective length of the frustum is now computed as follows:

$$S_e = r_e\theta_e \tag{4.7}$$

where

$$\theta_e = (R_o - R_i)/L \tag{4.8}$$

The horizontal component of the tension is now written as follows:

$$T_x = T\sin\theta_c = R_c P S_e \sin\theta_c \tag{4.9}$$

Finally, the output blocked force becomes

$$F_{out} = P(\pi R_i{}^2 + 2R_c S_e \sin\theta_c) \tag{4.10}$$

Using the data in Table 4.4 and comparing it with the experimental blocking force in Table 4.3 for 1C−LSOVA, the difference between the experimental and analytical blocked force for 1C−LSOVA is 7.20%. The analytical model can be used to predict the blocked force of LSOVA with reasonable accuracy. The main difference between the analytical and experimental blocked forces can be attributed to the fact that the analytical model does not consider the mechanical properties of the TPU used. The analytical model assumes that the walls are rigid and behave like rigid links. Therefore, the experimental blocked force is less compared to the analytical blocked force due to the softness of the TPU used to 3D print the soft actuators.

From Fig. 4.2, we can find the relationship between the linear stroke, D, and the angle θ_c, by assuming that the walls are undeformable, which is written as follows:

$$D = 2L\sin\theta_c \tag{4.11}$$

The difference between the predicted linear stroke by the analytical model and the experimental linear stroke of 8.57mm is 14.94%, which is reasonable considering that the real deformation is limited by the thick plastic residuals (i.e., printing artifacts) that interfered with the linear displacement of the LSOVA, as explained above. Therefore, the analytical model is effective enough to estimate the blocked force and linear output stroke of the LSOVA. Therefore, this analytical model can be used to efficiently design the LSOVA actuators, before 3D printing, to meet the desired performance in terms of blocked force and deformation.

4.5. LSOVA Characterization

4.5.1. Step Response

The step responses of five linear actuators that consist of a different number of vacuum chambers were obtained using a high-resolution laser sensor (Micro-Epsilon, optoNCDT 1700-50) that measured their linear displacement upon activation with 95.7% vacuum. As shown in Fig. 4.3, the actuators responded rapidly when vacuum was applied and recovered their initial position quickly when their internal pressure was returned to the atmospheric pressure using a solenoid valve (12 VDC Solenoid Valve, Air Leakage 1.0 cc/min). The rise time and decay time of each LSOVA are listed in Table 4.1.

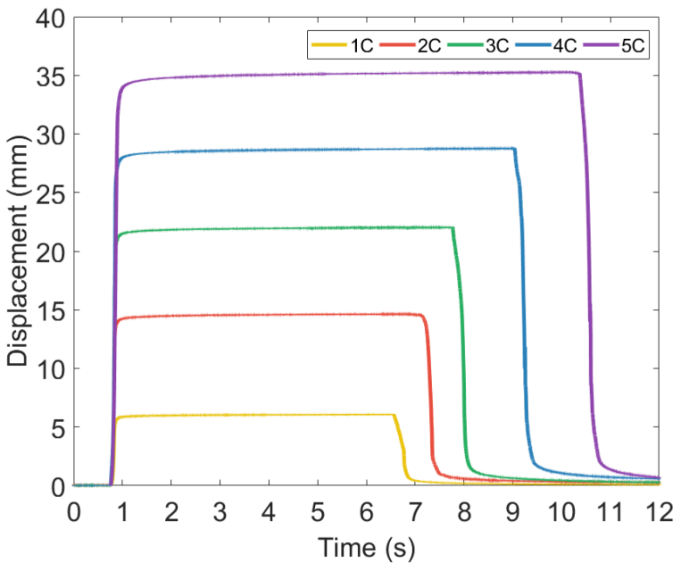

Fig. 10.3. Step response curves of LSOVAs.

The rise time of LSOVA is 25 times less than the rise time reported in [84], at least 3 times less than the rise time reported in [85] and 8 times less than the rise time reported in [86]. The rise time of LSOVA increased with the number of vacuum chambers. Also, the decay times of LSOVA were more significant compared to their rise times since the actuators' internal pressure was returned to atmospheric pressure using a solenoid valve, and consequently, the actuators were not forced to recover their initial position. Moreover, the buckling of the thin walls affected the recovery speed of LSOVA. The thin walls did not recover their initial shape directly upon the activation of the solenoid valve. The linear stroke of the actuators changed drastically after the vacuum pressure reached P = -20kPa, as shown in Fig. 4.4.

4.5.2. Hysteresis

The linear displacement of a 5C−LSOVA was measured when the negative input pressure was ramped up and down by a step of ΔP = -10kPa. The actuator exhibited hysteresis with the largest difference of 26.27mm occurring at P= -20kPa, as shown in Fig. 4.4. The buckling of the thin walls upon activation is the main reason for the hysteresis. The actuator contracts rapidly after the internal pressure reaches P= -20kPa.

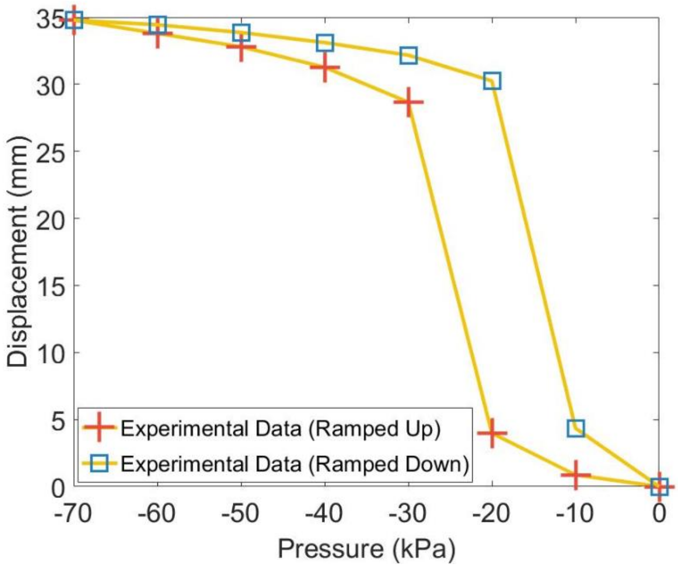

Fig. 10.4. Hysteresis curve of a 5C–LSOVA.

4.5.3. Actuation Frequencies and Bandwidths

The maximum actuation frequency (i.e., bandwidth) of LSOVA was obtained by activating the structure with 95.7% vacuum. The experimental actuation frequencies were limited by the speed of the solenoid valves and the inconsistent rate of discharge of the vacuum pump at high frequencies. Consequently, higher actuation frequencies were not achieved due to the limitations imposed by the pneumatic equipment. The actuation frequency decreased with an increase in the number of vacuum chambers, which is mainly because the actuators with a high number of cells have a larger internal volume to evacuate, and subsequently, more time is needed to fill them with air at the atmospheric pressure. This process will naturally increase the response time (i.e., decrease the bandwidth) of the actuators. The bandwidths of the distinct LSOVAs were estimated from their experimental step responses (Fig. 4.3), from which the corresponding Bode plots (e.g., Fig. 4.5 and Fig. 4.6) were obtained for 1C−LSOVA and 5C−LSOVA. The bandwidths of LSOVA are listed in Table 4.1.

The bandwidth of a 1C−LSOVA is 32 times greater than the bandwidth reported in [83] and 5.9 times higher than the bandwidth reported in [84]. The bandwidths of the other soft vacuum actuators in [85, 86] are not reported. Similarly, the bandwidth of a 5C−LSOVA is 17 times higher than the bandwidth reported in [83] and 3.5 times higher than the bandwidth reported in [84]. The design and material properties of the LSOVA contributed to their high bandwidths. First, the design of the thick horizontal walls and the thin walls allow a single chamber to collapse quickly in the vertical direction under a negative pressure. Also, since NinjaFlex is soft but not stretchable, a single chamber is deformed rapidly without any loss of energy due to the softness of the material.

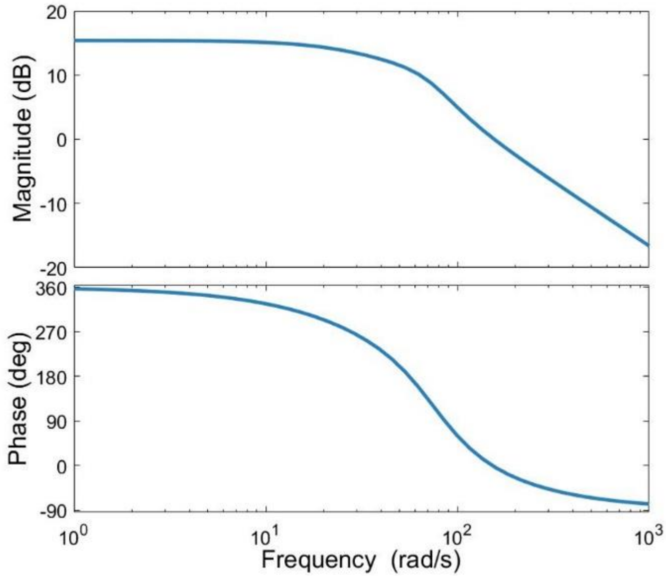

Fig. 10.5. Bode plot for 1C-LSOVA.

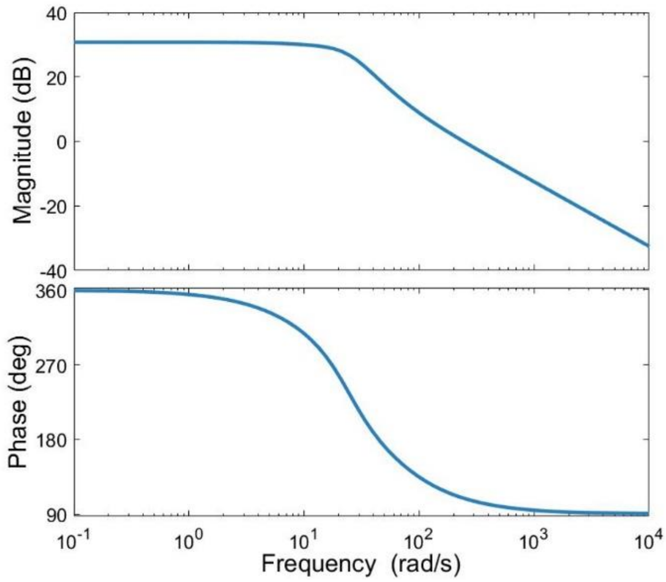

Fig. 10.6. Bode plot for 5C-LSOVA.

4.5.4. Blocked Force

The blocked force of the actuators was measured using a force gauge (5000g, FG-5005, Lutron Electronic Enterprise CO., LTD). The actuators were restricted from moving by constraining both ends when 95.7% vacuum was applied to measure the blocked force. The forces generated by various actuators consisting of a different number of vacuum chambers are presented in Table 4.1, and the blocked force experimental setup is shown in Fig. 4.7.

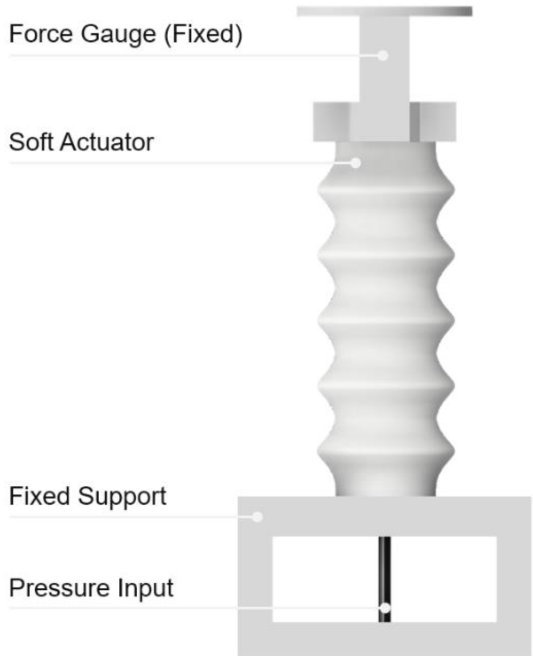

Fig. 10.7. LSOVA blocked force experimental setup.

The blocked force reported in [49] varied between 90N and 428N based on various designs. The blocked force produced by LSOVA is lower compared to the blocked force reported in [84]. However, it is important to note that a 30mm diameter LSOVA generated a blocked force of 60.58N, as presented in the "Scalability" section about LSOVA. Therefore, LSOVA can be scaled up to produce higher output forces. In [85], two types of soft vacuum linear actuators with different material properties were reported where the blocked force of a 20mm diameter LSOVA is 8 times larger than the blocked force of the first actuator reported and comparable with the blocked force of the second actuator reported. Similarly, the blocked force of a 20mm diameter LSOVA is 68 times larger compared to the blocked force of the first design reported in [86] and 30 times larger compared to the blocked force of the second design reported. The blocked force of LSOVA was larger compared to soft vacuum actuators made of softer materials. Although NinjaFlex is soft, it cannot stretch. This property enhanced the blocked force and payload of LSOVA.

The output force was consistent for the various linear actuators. The experimental and FEM results showed that the output blocked force is not dependent on the length of the actuators. To explain this consistency in the blocked force, we refer to the free-body diagram shown in Fig. 4.2. By taking a section cut on the first cell of a 5C−LSOVA, the output blocked force is equal to the internal force in this section. This internal force is equal to the output force of a 1C−LSOVA since an equilibrium of forces in the horizontal direction must be satisfied. Therefore, long actuators can be used without affecting the output force to target applications where large linear strokes are desired or required.

4.5.5. Creep

The internal pressure of the actuators was kept constant for 35 minutes while their position was monitored to detect any drift resulting from creep. The actuators experienced no creep, as shown in Fig. 4.8, which confirms that creep is independent of the number of cells. The position of the actuators remained unchanged during the activation period. The pressure of the system changed slightly by 0.32% for the longest actuator during the experiment, causing a negligible change in the strokes of the actuators. This small change in the pressure can be attributed to a slight leakage from fittings and connectors.

4.5.6. Lifetime and Durability

The number of cycles that the actuators sustained before failure was measured by activating them using 90% vacuum generated by a vacuum pump (Gardner Denver Thomas GmbH). It must be noted that the vacuum pump used in the previous experimental results could generate up to 95.7% vacuum. However, this pump was not practical and powerful enough to apply multiple thousands of cycles of the same level of vacuum. Therefore, we used this more powerful vacuum pump to apply 90% vacuum for the lifetime and durability experiments. In each actuation cycle, the actuators were activated to achieve full contraction. The LSOVA performance remained unchanged before failure. The internal pressure of LSOVA was returned to atmospheric in each cycle to recover their initial position after they were fully contracted. The lifetimes of the actuators are listed in Table 4.1. The lifetime of LSOVA is significantly higher compared to the reported lifetime of other 3D printed soft actuators [33, 37].

The main reason for the failure was the separation of the layers at the edges where the actuator cells experience high stress concentrations. It was observed that thicker walls result in high stress gradients at the edges of LSOVA upon activation. Even though the actuators failed, they were still able to lift the same load under a continuous supply of vacuum. It follows that they are fault-tolerant during operation. The main reason that these actuators are fault-tolerant is that the pressure loss due to the air gaps developed, after failure, can be compensated by a continuous vacuum supply. Also, the contraction of the walls of the actuator upon activation blocks the air gaps created. An airtight 1C–LSOVA with thinner walls (0.55mm) was tested and was able to sustain 80,000 actuation cycles before failure, which was approximately four times the lifetime of an LSOVA with thicker walls (0.68mm).

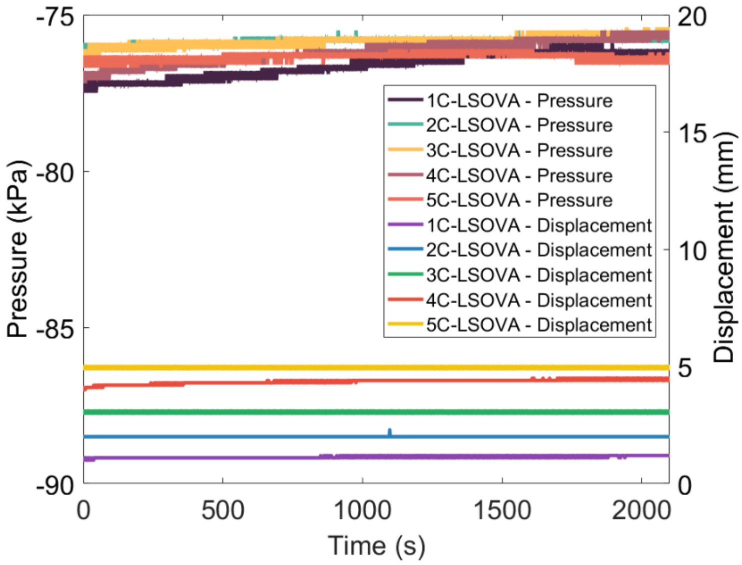

Fig. 10.8. Creep experiment pressure and displacement curves.

4.6. Scalability

One of the advantages of LSOVA is the possibility of assembling them in parallel to generate high output forces. There is a linear relationship between the number of actuators and the output force generated. Although the actuators are soft, high output forces and large linear displacements can be generated by implementing them as a bundle of linear actuators, as shown in Fig. 4.9. A bundle of two and four 3C–LSOVA can lift 5.0kg and 10.0kg, respectively, when activated with 95.7% vacuum. Also, the output force increases linearly with an increase in the internal volume of a single actuator for the same vacuum pressure (Fig. 4.9). A 10mm diameter 1C–LSOVA generated a blocked force of 6.86N and lifted a maximum load of 0.6kg when activated with 95.7% vacuum (Fig.4.9). Similarly, a 30mm diameter 1C–LSOVA generated a blocked force of 60.58N and lifted a maximum load of 5.1kg. Using Eq. 4.10 from the analytical model, we have obtained a blocked force of 7.16N for a 10mm diameter LSOVA with a difference of 4.42% compared to the experimental blocked force of 6.86N. Similarly, we have obtained a blocked force of 66.41N for a 30mm diameter LSOVA with a difference of 8.77% compared to the experimental blocked force of 60.59N. Therefore, the area of a single actuator can be chosen depending on the output force required for a specific application.

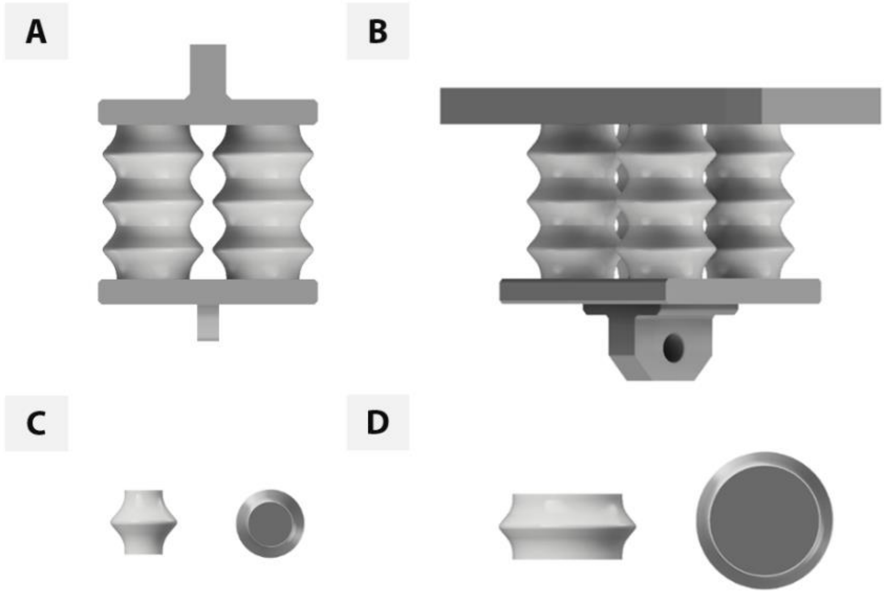

Fig. 10.9. LSOVA output force amplification. (A) A bundle of two 3C−LSOVA (B) A bundle of four 3C−LSOVA (C) 1C−LSOVA with a diameter of 10mm, an area of 591mm2, and a volume of 1226mm3 (D) 1C−LSOVA with a diameter of 30mm, an area of 2514mm2 and a volume of 8191mm3. The area of a 20mm diameter 1C−LSOVA is 1396mm2.

The scalability of the actuators presented in [84] is challenging, as reported since the actuators are composed of a soft skin and an internal skeleton. The performance of these scaled actuators was experimentally obtained. Also, the reported actuators in [85] and [86] are scalable. However, they should be carefully fabricated to obtain specific material properties that lead to the desired performance as opposed to LSOVA, which can be directly scaled up or down using 3D printing. Moreover, the performance of the scaled LSOVA can be accurately predicted using the FEM and analytical models before fabrication. However, it is important to note that since NinjaFlex has a poor bridging performance during the 3D printing process, the surface area of LSOVA (i.e., large diameters) cannot be increased dramatically.

4.7. Applications

LSOVA can be tailored to various robotic applications where they can be implemented as soft actuators.

4.7.1. Crawling Robot in Transparent Plastic Tube

We developed a crawling robot that moves through plastic tubes, as shown in Fig. 4.10. The robot is composed of three separate LSOVAs. The ends of the robot are designed carefully to push against the wall of the tube upon activation to hold it in place while the middle section of the robot moves it in the desired direction. The total body length of the robot is 70.5mm. Both ends of the robot are made of a 20mm diameter 1C−LSOVA, while the middle section is made of a 15mm diameter 2C−LSOVA. The robot moves with average horizontal and vertical speeds of 1.26mm/s and 1.11mm/s, respectively, upon activation with 95.7% vacuum. The robot can move forward and backward, depending on the actuation sequence imposed.

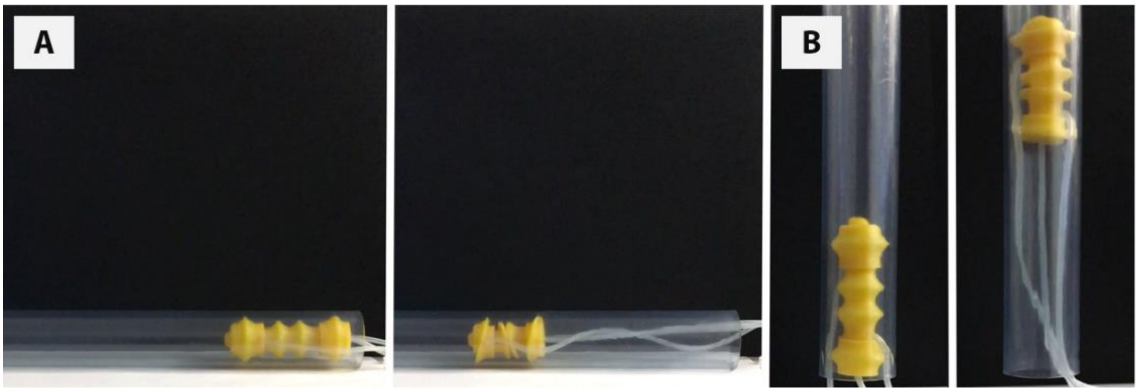

Fig. 10.10. Crawling robot based on LSOVA. The robot in a smooth and transparent 32mm diameter vinyl tube. (A) Horizontal tube (Left: Initial Position, Right: Final Position). (B) Vertical tube.

4.7.2. Soft Manipulator with Vacuum Suction Cup

We developed a soft parallel manipulator based on 3C−LSOVA, as shown in Fig. 4.11A. The manipulator can reach a bending angle of 90° when one of the parallel-connected actuators is activated using 95.7% vacuum. At the tip of the manipulator, we attached a 3D printed suction cup to show the versatility of LSOVAs. The soft manipulator can move to eight various positions while picking and placing objects. Here, we demonstrate that the soft manipulator is capable of picking carton pieces and putting them in different containers, as shown in Fig 4.11B. Also, the manipulator is capable of lifting and manipulating a maximum load of 0.5kg. This kind of soft manipulators can be used in industrial applications on assembly and sorting lines to pick and place delicate structures with moderate weights. These kinds of manipulators can interact safely with their environment since they are made of soft materials.

4.7.3. Soft Artificial Muscle

A single or multiple LSOVAs can be used as soft artificial muscles that can generate high forces. We implemented a 5C−LSOVA actuator to move an elbow joint by an angle of 45°, as shown in Fig. 4.12. The artificial muscle can lift a maximum load of 0.5kg. When no load is imposed on the system, the palm moves vertically upward by 130mm. However, when the system is loaded with a 0.5kg mass, the vertical distance decreases to 115mm.

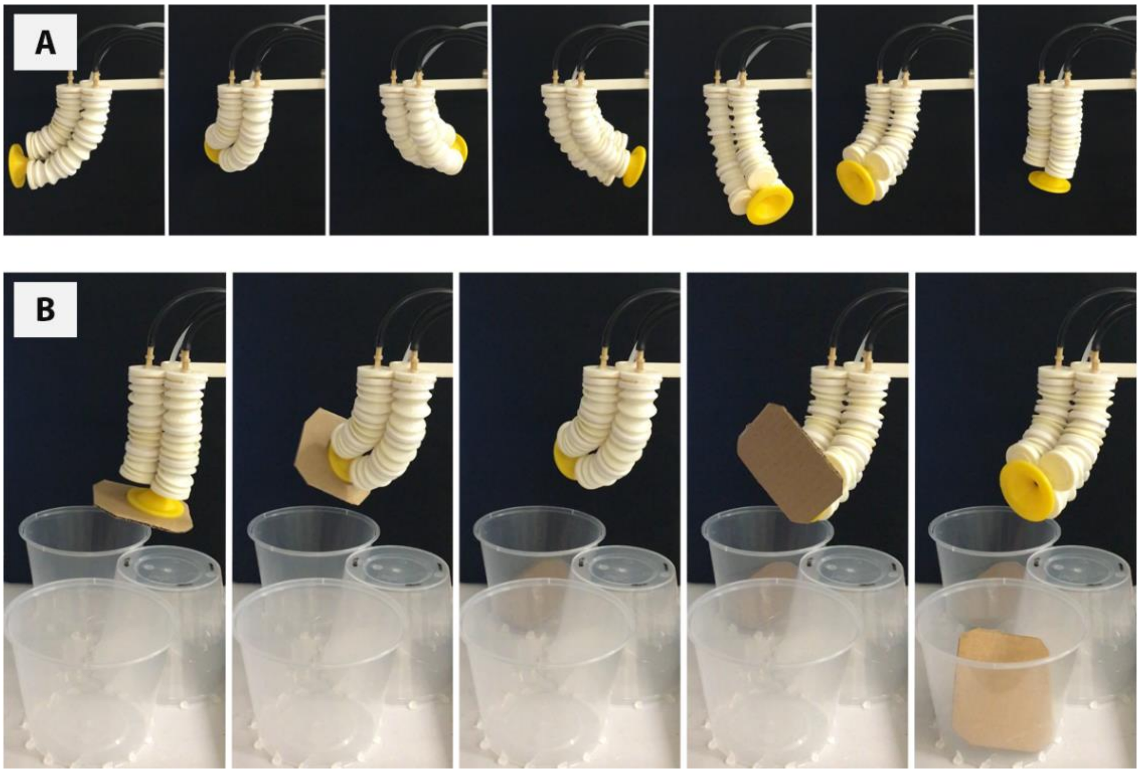

Fig. 10.11. Soft parallel manipulator based on LSOVA. (A) The parallel manipulator in 7 distinct positions. The remaining position where none of the actuators is activated is not shown. (B) The parallel manipulator picking and placing carton pieces in two different containers.

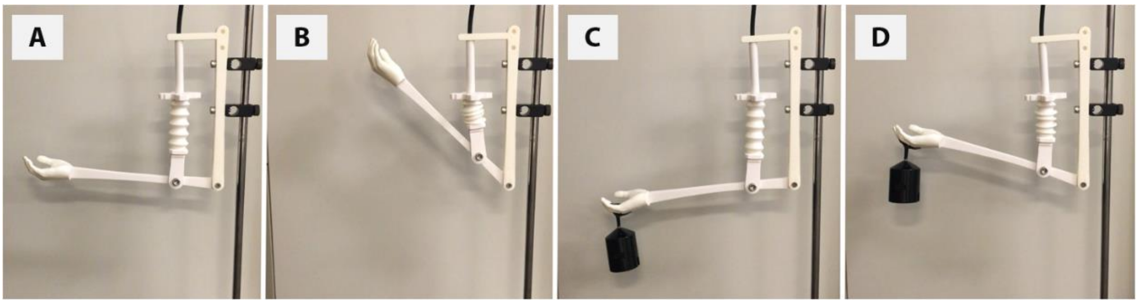

Fig. 10.12. Soft artificial muscle based on LSOVA. The elbow joint (A) unloaded, (B) unloaded and activated with 95.7% vacuum, (C) loaded with a 0.5kg weight and not activated, and (D) loaded with a 0.5kg weight and activated with 95.7% vacuum.

4.7.4. Soft Prosthetic Fingers and Grippers

Using the same 3D printing technique in [65], we fabricated a monolithic body with flexural joints, so that it can be configured as a tendon-driven soft prosthetic finger when activated using a 5C−LSOVA. The actuator pulls the tendon upon activation with 95.7 % vacuum causing the prosthetic finger to bend, as shown in Fig. 4.13. The LSOVA actuators can be coupled with tendons for soft prosthetic applications requiring high forces. The soft prosthetic finger can grasp various objects, as shown in Fig. 4.13.

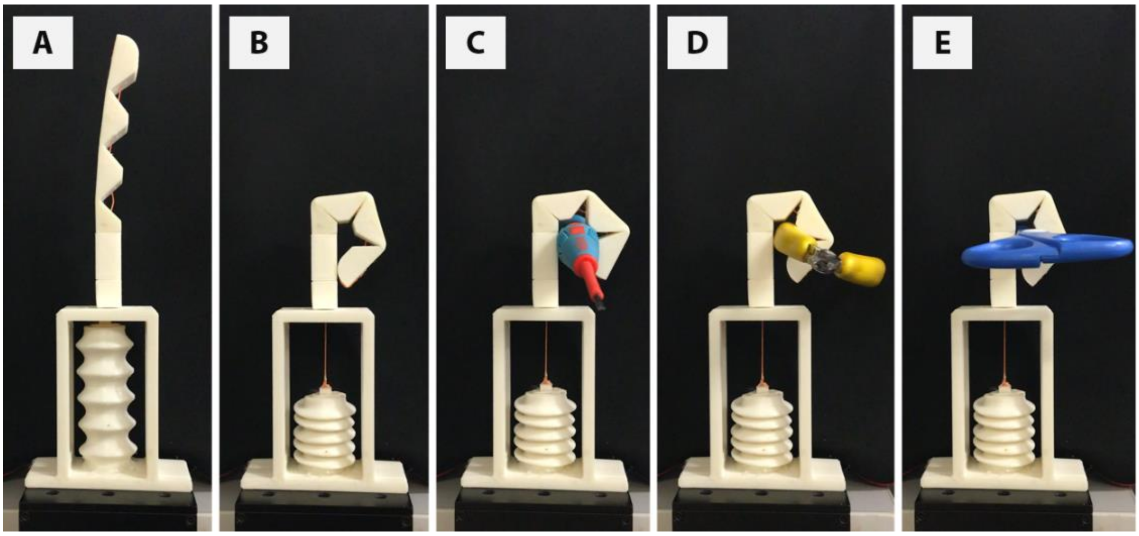

Fig. 10.13. Soft prosthetic finger based on LSOVA. Soft finger (A) Open position (B) and closed position. Soft finger grasping (C) a screwdriver (21.61g) (D) a plier (54.35g) (E) and scissors (30.58g) upon activation with 95.7% vacuum.

In addition, we have 3D printed a soft gripper based on these three soft fingers. The gripper is driven by one 5C−LSOVA coupled with tendons that run through its soft finger. The gripper can lift a load of 1.0kg. The load capacity of the soft gripper is highly dependent on the design of the fingers. In this scenario, the geometry of the fingers is not optimized but used only for demonstration purposes. Also, since the gripper is compliant, it can grasp and interact safely with flexible objects, as shown in Fig. 4.14.

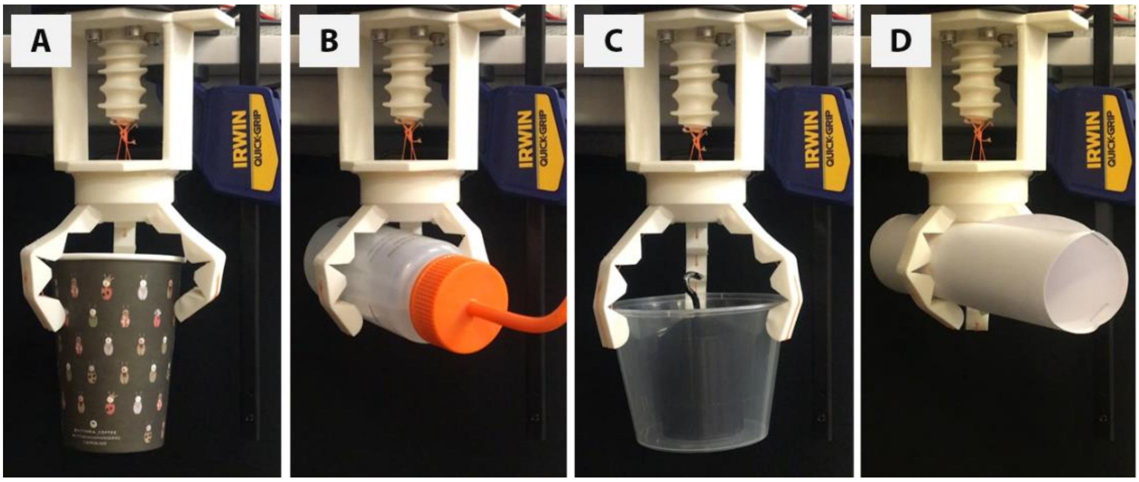

Fig. 10.14. Soft robotic gripper based on LSOVA. Soft gripper grasping (A) a cup (11.32g), (B) a bottle (45.94g), (C) a plastic container (1000g), (D) and a flexible paper cylinder (4.95g) upon activation with 95.7% vacuum.

4.8. A 3D Printed Omni-Purpose Soft Gripper

We have developed a 3D printed omni-purpose soft gripper (OPSOG) capable of grasping a wide variety of objects with different weights, sizes, shapes, textures, and stiffnesses. This versatile soft gripper has a unique design where soft 3D printed fingers and a soft 3D printed suction cup operate either simultaneously or separately to pick and place a wide variety of objects (Fig. 4.15). The soft linear vacuum actuators (LSOVA) that generate a linear stroke upon activation with vacuum are used to activate the tendon-driven soft fingers. OPSOG has a payload-to-weight ratio of 7.06, a maximum gripping force of 31.31N, and a tip blocked force of 3.72N. The soft gripper is mounted on a 6-DOF robotic manipulator, which is wirelessly controlled through a joystick (i.e., a PlayStation game controller) to pick and place objects in real-time. The user can directly control the position and orientation of the robotic arm and the soft gripper and activate the soft fingers and suction directly through the joystick.

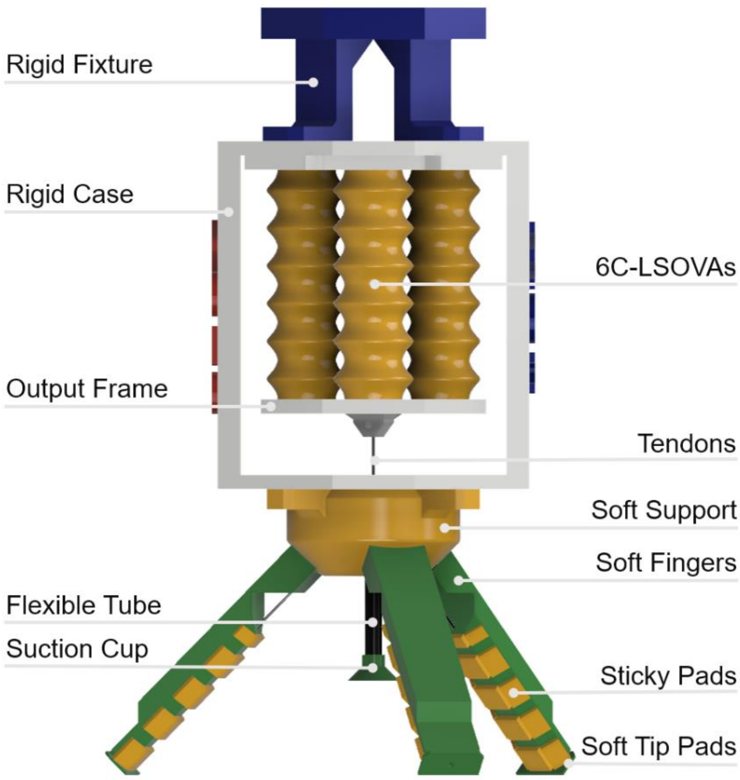

Fig. 10.15. OPSOG and its main components.

4.8.1. Materials and Methods

The soft gripper is modeled in Autodesk Fusion 360 (Autodesk Inc.). The main components of OPSOG are illustrated in Fig. 4.15. The 3D printed parts of OPSOG are 3D printed using an open-source FDM 3D printer (FlashForge Inventor, FlashForge Corporation). The solid support structures of OPSOG are all 3D printed using ABS plastic. The soft actuators, solid and soft supports, soft suction cup, and soft fingers are 3D printed and assembled, as shown in Fig. 4.15. The soft parts of OPSOG are 3D printed using NinjaFlex. Distinct colors of NinjaFlex are used to 3D print the soft parts of OPSOG. The soft fingers of OPSOG are covered with commercially available soft pads that stick to glass or similar objects with a smooth surface. The pads are cut using a laser cutter (VLS2.30 Desktop, Universal Laser Systems, Inc.) from a commercially available smartphone case (Goo.ey, Gooey Solutions Limited, UK) and were glued to the 3D printed soft fingers. A commercially available thin and flexible fishing lines (46.6kg/dia:0.483mm, GRAND PE WX8, JIGMAN, Japan) are used as tendons to drive the soft fingers. The overall cost of OPSOG, which includes the cost of NinjaFlex, ABS, tendons, plastic tubes, soft pads, bolts, and nuts, is approximately AU$33.

4.8.2. Suction Cup and Soft Fingers Design

The design of the suction cup is shown in Fig. 4.16. The suction cup is printed with thin walls (0.8mm wall thickness) that buckle and conform to objects upon activation. The suction cup is placed in the middle between the three soft fingers, which allows both systems to operate either separately or simultaneously without moving.

Each soft finger is designed with three main faces, as shown in Fig. 4.16C. The multiple faces on each finger allow the gripper to interact with objects from different angles, which increases the contact area between the fingers and the grasped objects. This design enables the gripper to grasp objects with irregular shapes and sharp corners. Soft pads that stick to a glossy surface such as glass are placed on the faces of each finger (Fig. 4.16D). It was observed that these pads increased the friction between the fingers and the grasped objects. Soft 3D printable green pads are added on the tip of the fingers. These pads allow the gripper to grasp flat objects that have a small height compared to their width and length.

4.8.3. Robotic Manipulator

A 6-DOF robotic manipulator (CRS A465, CRS Robotics Corporation, Canada) is used to move OPSOG in space to pick and place a wide variety of objects, as shown in Fig. 4.17.

4.8.4. User Input Device

We used a Dual-Shock 4 (DS4) wireless Bluetooth gaming controller (Sony, Australia) that has five analog inputs, a 6-axis motion sensor including a 3-axis gyroscope and a 3-axis accelerometer, twelve digital buttons, four digital direction buttons and a two-point capacitive touchpad with a click mechanism. Also, the DS4 controller contains two eccentric rotating mass vibration motors.

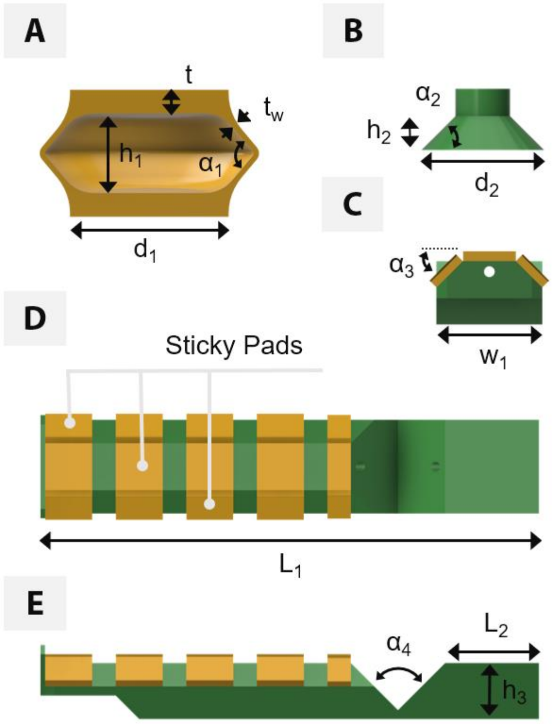

Fig. 10.16. OPSOG principal components design. (a) LSOVA one-unit dimensions: h1: 10.0, t: 3.0, tw: 0.80, d1: 20.0, α1: 110°, (b) Suction cup dimensions: h2: 5.0, d2: 18.0, α2: 45°. Soft fingers Dimensions (d) Front view: w1: 20.0, α3: 45° (d) Top view: L1: 107.0, (e) Side view: h3: 12.0, L2: 20.0, α4: 45°. All dimensions are in mm.

Fig. 10.17. CRS 6-DOF robotic manipulator with OPSOG.

4.8.5. OPSOG Gripping Force

The gripping force (GF) of the actuator was measured using a force sensor (5000g, FG-5005, Lutron Electronic Enterprise CO., LTD). The actuator was activated using 95.7% vacuum when the grasped objects with different shapes were pulled away from the gripper in a vertical direction (Fig. 4.18). The gripping force for the 3D printed cylinder, cube, and sphere was measured in three different states where the soft fingers and suction cup (SC) were activated either separately or simultaneously. The gripping forces in the three distinct states are listed in Table 4.5.

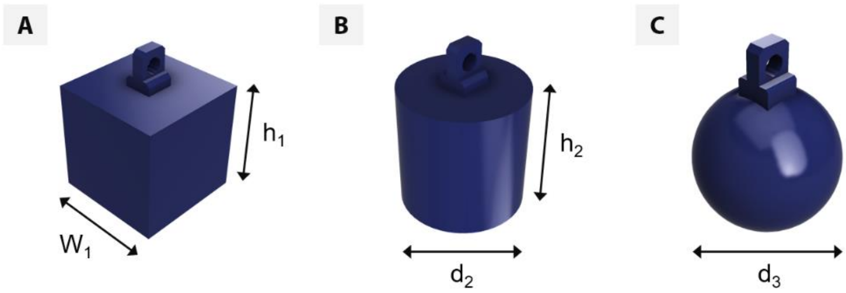

Fig. 10.18. Grasped shapes for gripping force experiments. (A) Cube: W1: 28.00, h1: 28.00 (B) Cylinder: d2: 28.00, h2: 28.00 (C) Sphere: d3: 28.00. All dimensions are in mm.

The maximum gripping force was identified before and after disengagement of the suction cup when both the fingers and suction cup were activated. The gripping force is highly dependent on the shape, size, and texture of the grasped objects. The gripping force of the suction cup depends on its size. 3D printing suction cups with a larger surface increase their gripping force. However, this suction cup size (Fig. 4.16B) is used to target objects having a small surface area. Also, the gripping force of the fingers depends highly on the friction force with the grasped objects. The pads are added on the inner surface of the fingers to enhance the contact friction force between the soft fingers and the grasped objects. Therefore, different suction cups can be used to target specific objects for specific applications. 3D printed suction cups can be replaced and plugged easily and quickly into OPSOG. Finally, the gripping force of the fingers can be enhanced by using soft pads that increase the friction force with the grasped objects. The maximum gripping force achieved by OPSOG is 31.31N, as listed in Table 4.5.

Table 10.5. OPSOG gripping force results.

Shape	**Cube**	**Cylinder**	**Sphere**
Description, Symbol	Value	Value	Value
Fingers Only GF, F_F	25.58N	31.31N	8.66N
SC Only GF, F_{SC}	15.79N	15.61N	11.31N
GF Before SC Disengagement, F_{BSC}	18.99N	21.83N	12.82N
GF After SC Disengagement, F_{ASC}	19.33N	29.02N	6.59N

Compared with the gripping force of other similar soft grippers reported in the literature, this gripping force is comparable with the gripping force of silicone molded underactuated grippers [66]. It is higher than the gripping force reported in [119, 120] and lower than the one reported in [121] for grippers based on fiber-reinforced actuators. It is higher than the gripping force reported in [122] and lower than the one reported in [123] for grippers based on PneuNets. It is higher than the gripping forces reported in [124, 125] for grippers and hands based on hybrid fingers made of soft and rigid materials. It is higher than the blocked force reported in [126] for a gripper based on compliant mechanisms and higher than the blocked forces reported in [33, 34] for FDM 3D printed soft actuators. It is reasonable to note that the gripping force of OPSOG is lower compared to the gripping force of some soft robotic grippers driven by positive pressure actuators. This difference in the gripping force is due to several reasons, such as enhanced gripping capabilities using Gecko-like adhesives in [123] and using positive pressure soft pneumatic actuators such as PneuNets and fiber-reinforced actuators as the fingers of the soft grippers where the gripping force is related to the positive pressure applied. The gripping force increases with an increase in the positive pressure applied. However, for soft vacuum actuators, the output force is limited by the maximum vacuum pressure that can be practically used.

4.8.6. Fingertip Blocked Force

The blocked force of the soft fingers was measured using a force sensor (5000g, FG-5005, Lutron Electronic Enterprise CO., LTD) when the gripper was activated using 95.7% vacuum. Two fingers were left to move freely upon activation of the soft gripper while the remaining third finger was restricted from moving at its tips where the force sensor was attached perpendicularly. The maximum blocked force generated by the soft finger is 3.72N. This blocked force of 3.72N is higher than the tip blocked force reported in [36, 120, 127, 128], lower than the tip force reported in [33] and comparable with the one reported in [126]. The blocked force in [33] is relatively higher compared to the tip force generated by the soft fingers of OPSOG since the fingers of the gripper in [33] are based on positive pressure bellow-like soft actuators where the gripping force is related to the amount of pressure applied.

4.8.7. Payload of Fingers and Suction Cup

The weight of the gripper including the fixture used to attach it to the robotic arm is 389.69g. We obtained the maximum load lifted by the gripper by activating the soft fingers and suction cup simultaneously. OPSOG lifted a load of 2.7kg when the 6C−LSOVA bundle was activated using 95.7%

vacuum. The maximum payload to weight ratio of OPSOG is 7.06. The maximum load of 2.7kg lifted by OPSOG is higher than the load lifted by the soft grippers and hands reported in [34, 119, 120, 124, 126-128] and lower than the load lifted by the soft grippers activated by positive pressure in [33, 121, 123, 129]. The load lifted by other similar soft grippers that OPSOG outperformed in terms of gripping force and blocked force was not reported [36, 66, 122, 125].

4.8.8. Grasped Objects

The gripper can pick and place a wide variety of objects with different weights, shapes, stiffnesses, and textures, as shown in Fig. 4.19. The objects grasped are chosen based on the common objects used in daily activities. The soft fingers and suction cup of OPSOG are activated either separately or simultaneously, where the gripping is achieved using both systems. For the gripping process, the suction cup is activated first if there is enough room for it to attach to the grasped object. Then, the fingers are activated to achieve a firm and stable grip. In this case, the fingers acted as a support for the grasped object. The soft fingers wrap around the grasped object after activating the suction cup to provide additional support and a firm grip during the movement of the robotic manipulator. This approach is crucial since it enhances the range of objects the gripper can grasp and interact with and it provides a firm grip during movement and against external disturbances. OPSOG showed its versatility and dexterity and the effectiveness of using suction cups along with soft fingers to grasp and manipulate a wide variety of objects. However, it is essential to note that OPSOG is not capable of picking and placing very large objects compared to its size.

4.8.9. Discussion on OPSOG

The OPSOG gripper can grasp a wide variety of objects with different weights, sizes, shapes, textures, and stiffnesses. In addition, OPSOG can be used in a wide variety of picking and placing applications where rigid and soft objects are involved. The gripper is lightweight and has a low manufacturing cost. OPSOG is 3D printed from commercially available low-cost materials using an inexpensive and open-source FDM 3D printer. This feature drastically reduces the replacement and maintenance costs and makes it suitable for do-it-yourself applications. Moreover, OPSOG is customizable. The gripper can be designed to meet specific or desired requirements for applications. First, the core of OPSOG, which is the set of linear actuators, can be scaled depending on the force required or desired for a specific application. Second, the stiffness and the softness of the soft fingers can be changed by changing some printing parameters such as infill percentage and the number of flexural joints in each finger. Third, the suction cup can be easily replaced and sized according to specific applications.

OPSOG is a gold medal award winner at the 2018 IEEE International Conference on Robotics and Automation (ICRA). The Soft Grip Competition aimed to determine the most effective soft robot for gripping tasks. Objects with various weights, sizes, shapes, and stiffnesses were set for the soft gripper to grip and transport. The objects included a baseball cap, a banana, an apple, a pair of scissors, a tissue box, a power bank, a USB memory stick, a shuttlecock, a notebook, a chewing gum box, a cotton swab box, a potato chips bag, a double-faced adhesive tape, a bar of soap, and a bunch of grapes. OPSOG installed at the endpoint of a robot manipulator picked and placed all the specified objects successfully. OPSOG showed its versatility and effectiveness in soft robotic applications by picking and placing the different objects successfully.

4.9. Discussion

One main downside of LSOVA is the nonlinear relationship between the negative input pressure and the stroke (i.e., displacement) of the actuator, as shown in Fig. 4.4. The walls of the actuators buckle after a certain level of vacuum, which causes a rapid deformation. We postulate that the main reason behind the large hysteresis exhibited by LSOVA is the buckling of the thin walls. This nonlinear behavior makes the control of LSOVA very challenging, which is one of the future research topics. The objective of this work is to directly 3D print or fabricate low-cost and airtight linear soft actuators that can be activated through vacuum.

The soft actuators developed were not comprehensively optimized to operate at their maximum performance. The geometry of the actuators dramatically affects their performance in terms of blocked force, lifting force, rectilinear displacement, actuation frequency, and lifetime. The wall thickness of LSOVAs is the main parameter that needs to be optimized. It was proved experimentally that actuators with thinner walls had a higher output force, higher lifting force, longer lifetime, and higher payload-to-weight ratio. However, airtightness becomes a major concern when printing soft actuators with thin walls. Therefore, the thickness of the walls should be optimized to ensure airtightness and a maximum possible performance. In addition, only circular shapes were considered in this study. However, LSOVA can be printed in different shapes, such as rectangular and elliptical, with various aspect ratios to target specific applications.

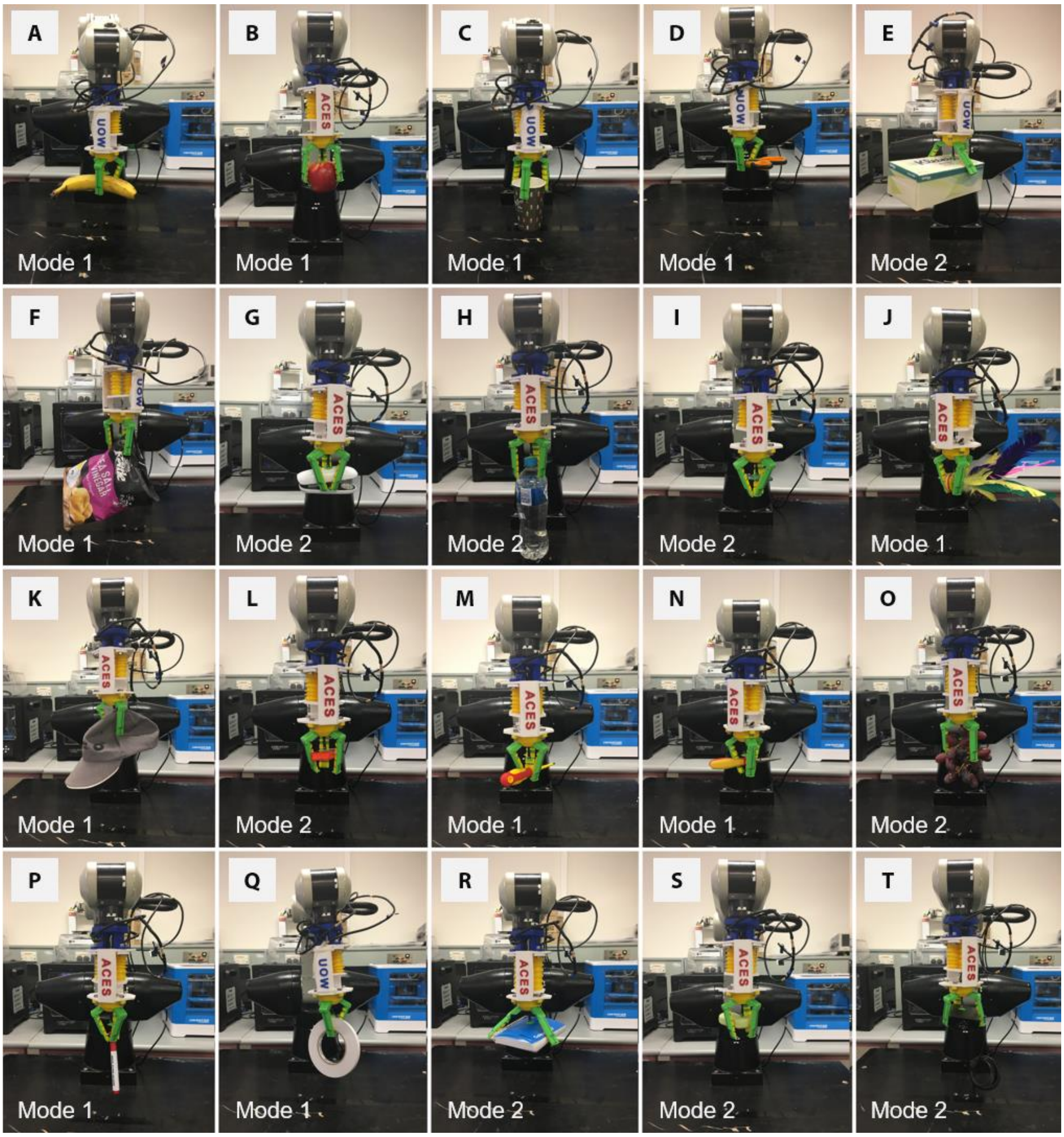

Fig. 10.19. OPSOG picking and placing a wide variety of objects. OPSOG grasping (A) a banana (213.05g), (B) an apple (203.16g), (C) a cup (10.90g), (D) a pair of scissors (83.01g), (E) a tissue box (203.20g), (F) a bag of potato chips (186.46g), (G) a stapler (161.93g), (H) a bottle of water (630.43g), (I) a USB (7.88g), (J) a shuttlecock (21.56g), (K) a cap (75.46g), (L) a chewing gum box (32.77g), (M) a screwdriver (56.72g), (N) a pliers (146.93g), (O) a few grapes (316.31g), (P) a pen (10.60g), (Q) a tape (125.46g), (R) a notebook (207.39g), (S) a soap (116.47g), (T) a power adapter (338.34g). Mode 1: Only soft fingers are activated. Mode 2: Soft fingers and suction cup are activated.

4.10. Conclusions

We have established 3D printable linear soft actuators, LSOVA, that can be activated through vacuum. The actuators were directly manufactured using a low-cost open-source FDM 3D printer, without requiring any secondary manufacturing or assembly process. The vacuum actuators generate high output forces and large rectilinear displacements. In addition, the quasistatic behavior of LSOVA can be accurately predicted in terms of the linear displacement and blocked force using FEM and a geometric model.

Chapter 5

3D Printable Soft Pneumatic Sensing Chambers (SPSC)

5.1. Introduction

We present airtight soft pneumatic sensing chambers (SPSC) that are directly 3D printed, without requiring any support material and post-processing. The SPSC have multiple advantages such as very fast response to any change to their internal volume under four main mechanical input modalities of compression, bending, torsion and rectilinear displacement, favorable linearity, negligible hysteresis, stability over time, repeatability, reliability, long lifetime, and very low power consumption. The SPSC as the soft and interactive interfaces between humans and machines shown in Fig. 5.1 can be used as soft pneumatic push buttons (SPPB), linear sensors (SPLS), bending sensors (SPBS), and torsional sensors (SPTS). The performance of the various SPSC was optimized and predicted using FEM to obtain a linear relationship between the input mechanical deformations and the output pressure. These soft pneumatic structures can be rapidly designed, customized, and 3D printed to target various applications, including wearable gloves for virtual reality applications and telecontrol of adaptive grippers, touch buttons for interactive robotic platforms for STEM education and haptic devices for rehabilitation, controllers and throttles for gaming applications and bending sensors for prosthetic fingers tracking and control.

5.2. Developing 3D Printable Pneumatic Soft Sensors

We aim to design and develop multipurpose and robust 3D printable soft pneumatic sensors that have multiple advantages such as fast response, linearity, negligible hysteresis, stability over time, long lifetime, and low power consumption using a low-cost FDM 3D printer that employs a commercially available soft TPU. The objective is achieved by optimizing the soft chambers developed using FEM simulations that predict their performance. The main reason for developing such chambers as pressure sensors is to provide a new class of robust soft sensors that can be easily manufactured and directly integrated into diverse soft robotic systems.

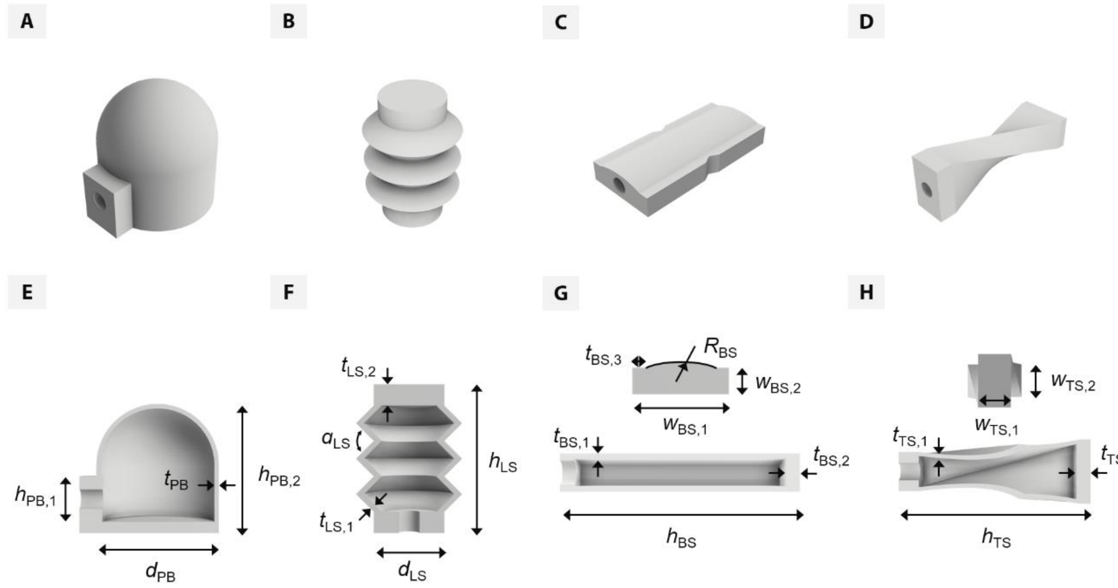

Fig. 11.1. SPSC dimensions and CAD models. (A) Soft Pneumatic Push Sensor (SPPB) (B) Soft Pneumatic Linear Sensor (SPLS) (C) Soft Pneumatic Bending Sensors (SPBS) (D) Soft Pneumatic Torsional Sensor (SPTS) (E) SPPB dimensions: d_{PB}: 20.0, $h_{PB,1}$: 8.0, $h_{PB,2}$: 22.8, t_{PB}: 0.80. (F) SPLS dimensions: d_{LS}: 10.0, h_{LS}: 21.0, $t_{LS,1}$: 0.80, $t_{LS,2}$: 3.0, α_{LS}: 90.0°. (G) SPBS dimensions: h_{BS}: 34.0, R_{BS}: 15.0, $t_{BS,1}$: 0.80, $t_{BS,2}$: 2.0, $t_{BS,3}$: 3.0 $w_{BS,1}$: 15.6, $w_{BS,2}$: 4.35. A triangular groove with a base of 4.0mm and a height of 1.0mm is added to obtain a local bending joint. (H) SPTS dimensions: h_{TS}: 38.0, $t_{TS,1}$: 0.80, $t_{TS,2}$: 2.8, $w_{TS,1}$: 7.8, $w_{TS,2}$: 12.8. The top wall of the SPTS is twisted by an angle of 90° with respect to its base. All dimensions are in mm.

5.3. Modeling and Fabrication

The SPSC are designed and modeled in Autodesk Fusion 360 (Autodesk Inc.). The SPSC are modeled with a minimum wall thickness of 0.8mm to ensure that the 3D printed prototypes are airtight. The printing parameters are optimized to obtain functional airtight prototypes. The stability of the SPSC over time is highly dependent on the degree of their airtightness. The optimized 3D printing parameters are listed in Table 5.1. The SPSC are printed using a low-cost and open-source FDM 3D printer (FlashForge Inventor, FlashForge Corporation).

5.4. Finite Element Modeling

Finite element simulations are performed on the various SPSC to optimize their topology in order to obtain a linear relationship between the applied mechanical loads and the change in their internal volume (Fig. 5.2) and to predict their behavior under such mechanical loads. A Static Structural Analysis is implemented in ANSYS. The CAD models are meshed using higher-order tetrahedral elements. Contact pairs are defined between thin walls that come into contact when large mechanical deformations are applied to the SPSC. In terms of boundary conditions, a Fixed Support is defined on one side of each structure, and an appropriate Displacement Support is imposed on their opposite ends to simulate the mechanical deformations applied for each mode of deformation (Fig. 5.3). The FEM simulations prove that a linear relationship exists between the applied mechanical loads and the change in the internal volume of each SPSC, as shown in Fig. 5.2. Ideally,

Table 11.1. Optimized printing parameters for 3D printing SPSCs.

Parameter	Value	Unit
	Resolution Settings	
Primary Layer Height	0.1	(mm)
First Layer Height	0.09	(mm)
First Layer Width	0.125	(mm)
Extrusion Width	0.4	(mm)
	Ooze Control	
Coast at End	0.2	(mm)
	Retraction Settings	
Retraction Length	4	(mm)
Retraction Speed	40	(mm/s)
	Speed Settings	
Default Printing Speed	10	(mm/s)
Outline Printing Speed	8	(mm/s)
Solid Infill Speed	8	(mm/s)
First Layer Speed	8	(mm/s)
X/Y Axis Movement Speed	50	(mm/s)
Z-Axis Movement Speed	20	(mm/s)
	Temperature Settings	
Printing Temperature	240	(°C)
Heat Bed Temperature	32	(°C)
	Cooling Settings	
Fan Speed	50	(%)
	Infill Settings	
Infill Percentage	100	(%)
Infill/Perimeter Overlap	30	(%)
	Thin Walls and Movements Behavior	
Allowed Perimeter Overlap	25	(%)
External Thin Wall Type	Perimeters Only	(-)
Internal Thin Wall Type	Allow Single Extrusion Fill	(-)
Avoid Crossing Outline	ENABLED	(-)
Detour Factor	100	(-)
	Additional Settings	
Extrusion Multiplier	1.15	(-)
Top Solid Layers	5	(-)
Bottom Solid Layers	5	(-)
Outline/Perimeter Shells	25	(-)
Wipe Nozzle	DISABLED	(-)
Support Material	DISABLED	(-)

a relationship exists between the change in the internal volume and the actual pressure change obtained experimentally when the mechanical loads are applied to the various SPSC. Therefore, FEM can be used to predict the behavior of the SPSC and to optimize their topology to meet specific design requirements quickly and efficiently without wasting potential 3D printing resources.

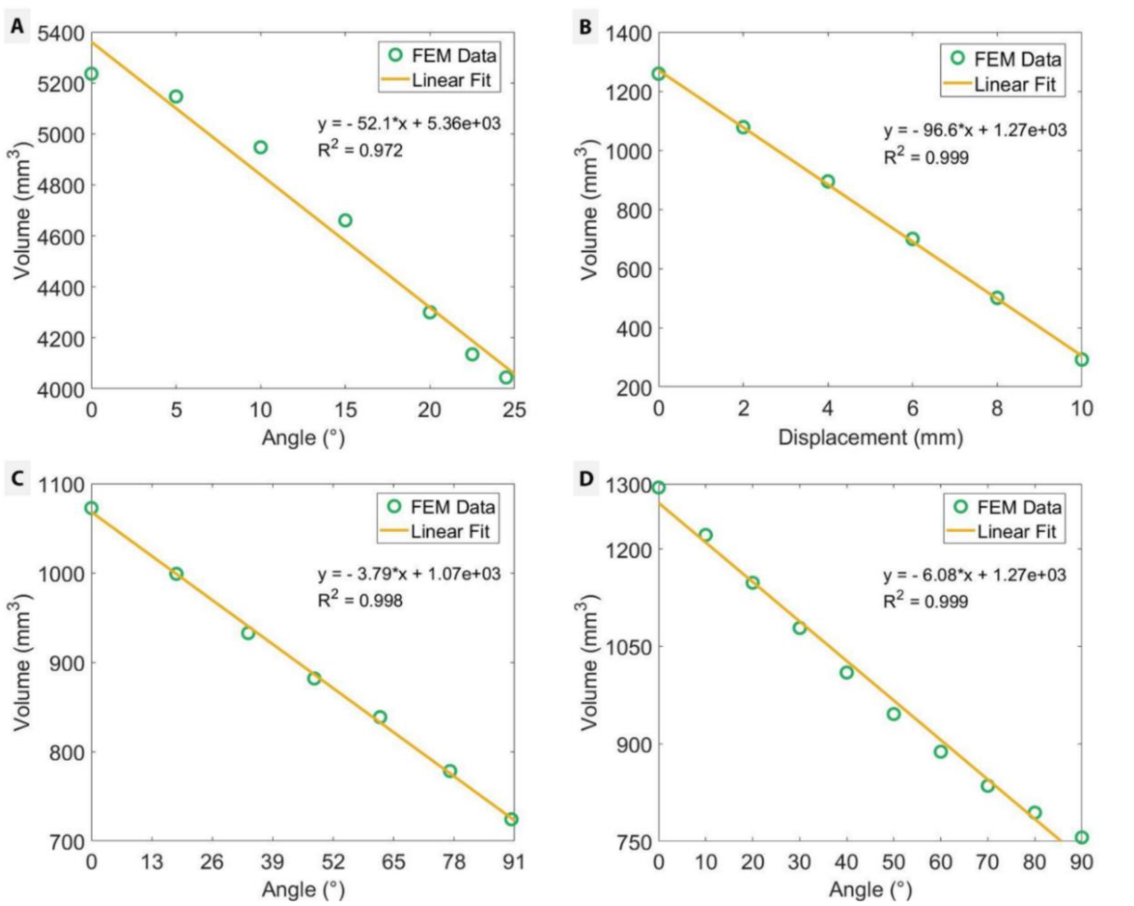

Fig. 11.2. Finite element modeling results for the SPSCs. The relationship between the input mechanical load and the corresponding change in the volume of the pneumatic chamber for a (A) SPPB, (B) SPLS, (C) SPBS, and (D) SPTS.

5.5. Characterization

We activated the SPSC to characterize their performance in terms of linearity, hysteresis, repeatability, reliability, lifetime, and stability over time. The boundary conditions applied to each type of SPSC are shown in Fig. 5.3.

5.5.1. Linearity and Hysteresis

We activated all the SPSC to obtain a relationship between the mechanical inputs (i.e., deformations) applied to each type and the corresponding output pressure. In each case, the mechanical deformation applied was ramped up and down to assess the hysteresis exhibited by each structure. Fig. 5.4 shows that all the SPSC have a linear relationship between the mechanical deformations applied and the corresponding output pressure and that they exhibit negligible hysteresis. The linearity and negligible hysteresis exhibited by the SPSC make them ideal to be used directly in diverse soft robotic applications without requiring sophisticated control approaches. Also, this linearity means that the sensors can be directly 3D printed and used. The relationship between the input displacement and output pressure can be obtained by using two data points to be used consistently since the SPSC are stable over time, reliable, and repeatable. Therefore, there is no need for an empirical formula that requires an experimental evaluation using a specific experimental setup to obtain and describe the relationship between the input displacement and the output pressure for each 3D printed SPSC. Linearity is one of the desired performance metrics for actuators and sensors.

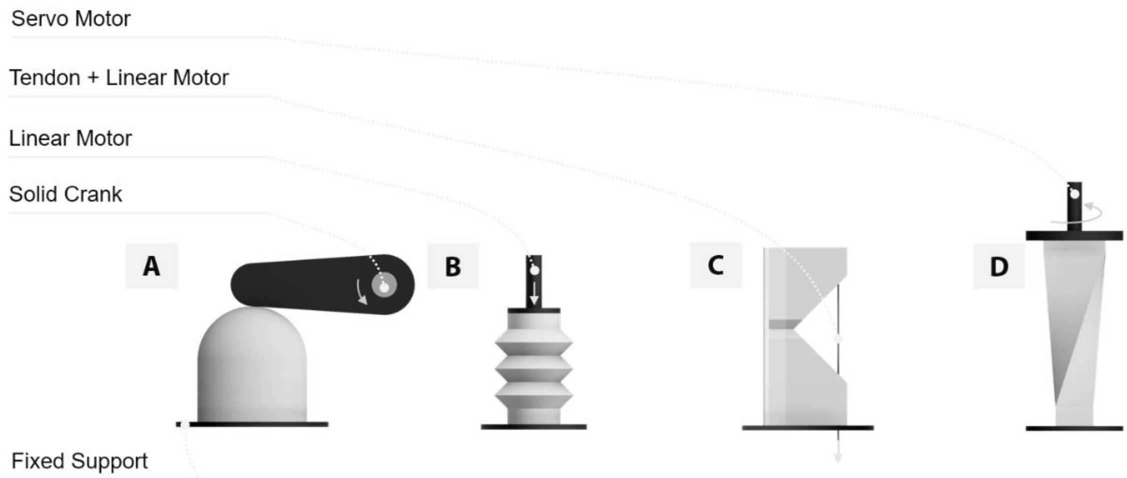

Fig. 11.3. Boundary conditions applied to the SPSC. (A) SPPB activation through a solid rotating crank that pushes through its soft deformable wall. (B) SPLS attached to a linear motor that generates a linear stroke of 10mm. (C) SPBS attached to a soft flexure joint that generates a bending angle between 0° and 90° when the tendon is pulled using a linear motor. (D) SPTS attached to a servo motor that generates an angular displacement between 0° and 90°.

5.5.2. Repeatability and Reliability

All the SPSC were activated repeatedly to assess their reliability and consistency over time. Fig. 5.5 shows that all the SPSC generated a consistent output pressure signal under the same mechanical load applied repeatedly. These results prove that the SPSC are repeatable and generate a reliable pressure signal without any noticeable drift. Also, these results confirm that the SPSC are airtight. This repeatability is crucial in soft robotic applications involving repeatable movements that need to be monitored or controlled.

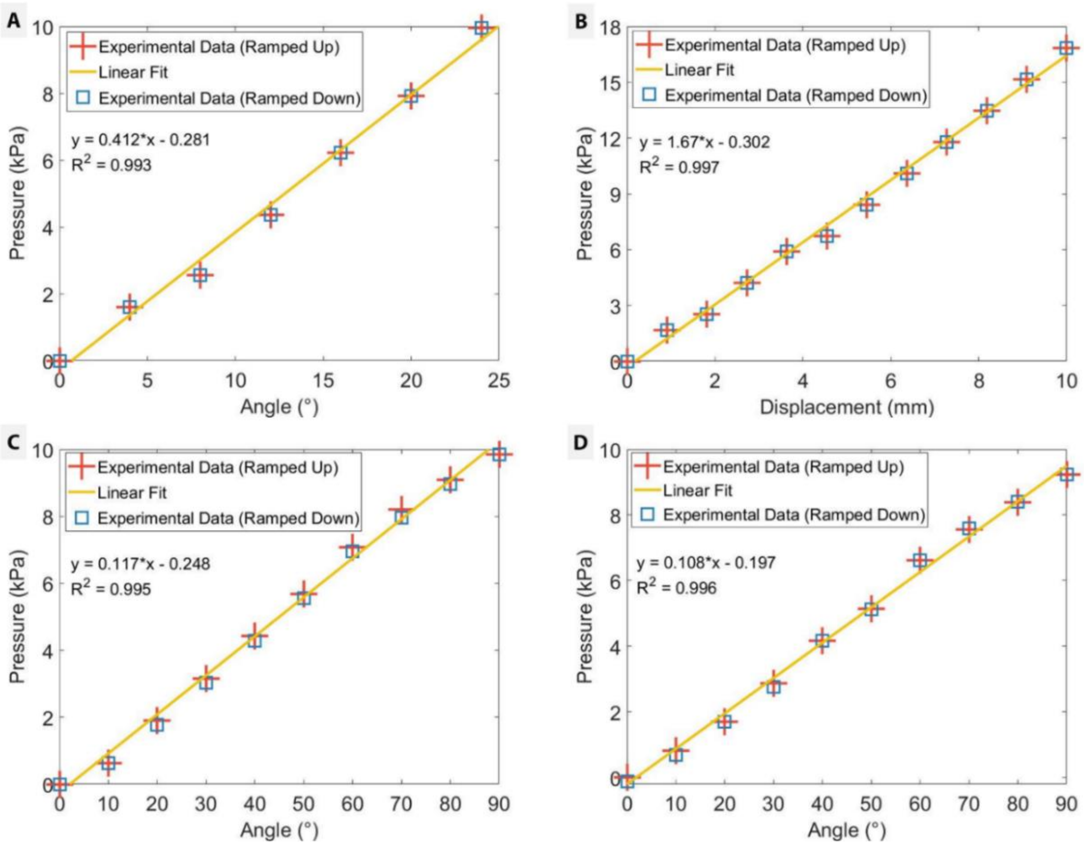

Fig. 11.4. Linearity and hysteresis experimental results for the SPSCs. (A) SPPB, (B) SPLS, (C) SPBS, (D), and SPTS output pressure as a function of the applied input mechanical deformation.

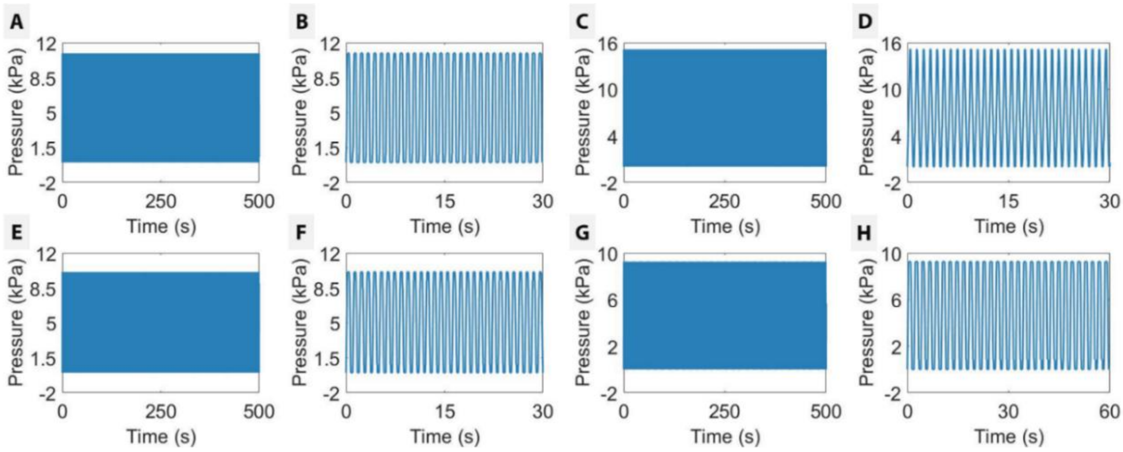

Fig. 11.5. Repeatability and reliability experimental results for the SPSCs. (A) SPPB 500 activation cycles with a frequency of 1.0Hz. (B) SPPB 30 out of 500 activation cycles. (C) SPLS 500 activation cycles with a frequency of 1.0Hz. (D) SPLS 30 out of 500 activation cycles. (E) SPBS 500 activation cycles with a frequency of 1.0Hz. (F) SPBS 30 out of 500 activation cycles. (G) SPTS 500 activation cycles with a frequency of 0.5Hz. (H) SPTS 60 out of 500 activation cycles. It is important to note that the SPTS was activated with a frequency of 0.5Hz, which was the maximum value the servo motor used could handle.

5.5.3. Lifetime

The SPSC were activated repeatedly to assess their durability. A single SPBP sustained 60,000 activation cycles before failure. The remaining SPSCs sustained 150,000 activation cycles without any noticeable failure. All the SPSC showed a relatively long lifetime. The SPPB, SPLS, and SPBS were activated with a frequency of 1.0Hz. The SPTS was activated with a frequency of 0.5Hz, which was the maximum value the servo motor used could handle. The main reason for the difference between the lifetime of the SPPB and the other SPSCs is that the SPPB topology involves overhangs, which resulted in thinner curved walls.

5.5.4. Stability Over Time

The SPSC were activated for 30 minutes continuously to assess their stability over time. The internal pressure of the SPSC remained unchanged during the activation period, as shown in Fig. 5.6. This result proves that the SPSC are very stable and do not experience any drift over time. Therefore, the SPSC can be used reliably in soft robotic applications for extended periods.

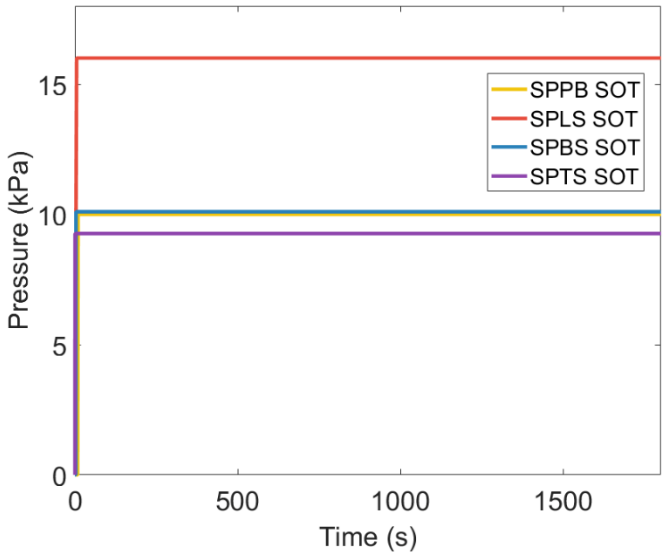

Fig. 11.6. Stability over time experimental results for the SPSCs. Stability over time for all SPSC.

5.6. Applications

Here we demonstrate that the SPSC can be tailored to various soft and interactive robotic applications, including virtual reality, telecontrol of soft robotic systems, STEM education, haptic feedback devices, rehabilitation devices, gaming controllers, and master/slave robotic fingers.

5.6.1. Soft Wearable Glove for Virtual Reality Applications

A soft glove composed of five SPBS is developed to track the motion of a human hand, as shown in Fig. 5.7 and Fig 5.8. Each soft bending chamber of the glove is connected to a separate pressure sensor to track the position of a distinct finger.

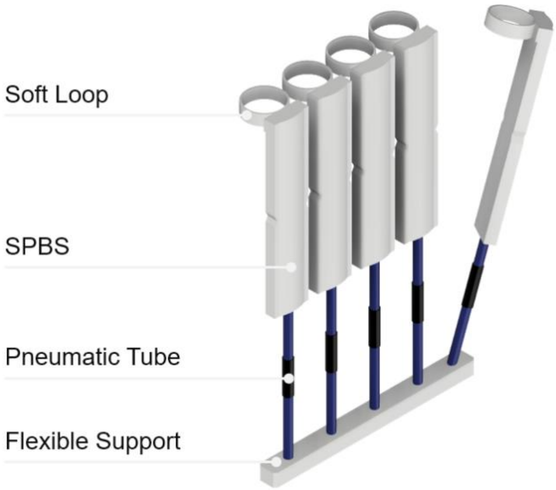

Fig. 11.7. Soft wearable glove 3D model.

The position of each finger is directly tracked and visualized using a 3D virtual hand simulation model. The soft glove can be useful for virtual reality applications to track the movements of the various human body parts.

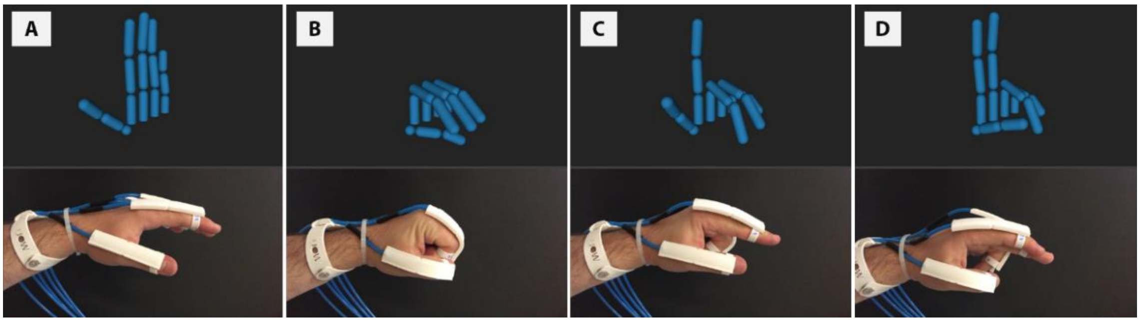

Fig. 11.8. Soft wearable glove for virtual reality applications. (A to D) The soft wearable glove used to track various hand gestures.

5.6.2. Soft Glove as a Remote Controller for Soft Adaptive Grippers

The same soft glove is used to drive a three-finger soft gripper using a servo motor, as shown in Fig. 5.9. The glove can be used to directly drive the gripper to pick and place fruits, vegetables, and other objects with various weights, shapes, textures, and stiffnesses. The position of the fingers can be precisely controlled using the glove directly without requiring any control algorithms to grasp the objects and to manipulate them finely. With this straightforward implementation, the glove proves to be robust and reliable to drive the gripper with relatively high precision and stability. These soft gloves can be used to telecontrol other soft robotic structures with precision using very minimal control.

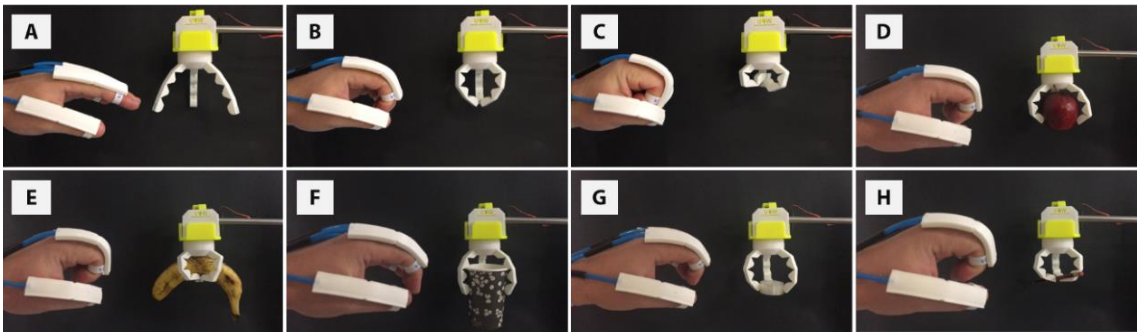

Fig. 11.9. Soft glove as a remote controller for soft adaptive grippers. The wearable glove controlling a soft adaptive gripper (A to C). The gripper can be precisely controlled to grasp various objects, including (D) an apple, (E) a banana, (F) a cup, (G) a tape, and (L) a pencil.

5.6.3. Soft Interactive Piano for STEM Education

A piano keyboard composed of six keys printed in different colors is developed, as shown in Fig. 5.10 and Fig. 5.11. The SPPBs used are directly connected to separate pressure sensors. The soft piano keys can generate six different musical notes, including Do (C), Re (D), Mi (E), Fa (F), Sol (G), and La (A).

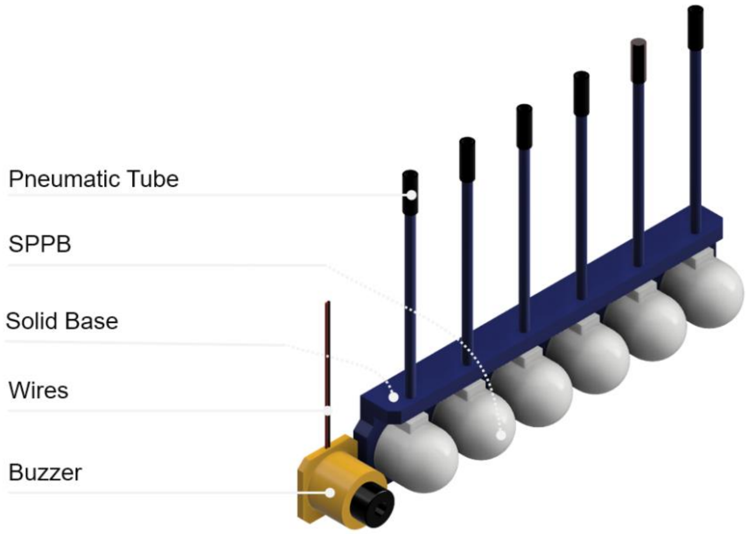

Fig. 11.10. Soft interactive piano 3D model.

When a specific key is activated, a buzzer generates a corresponding note with a specified frequency. The piano can be used to play a music piece interactively, as shown in Fig. 5.11. An interactive screen shows graphically the changes in the pressure for each key and its corresponding representation using a virtual colored light-emitting diode (LED). The sensitivity of the soft keys to any mechanical deformation can be directly changed by changing a pressure threshold.

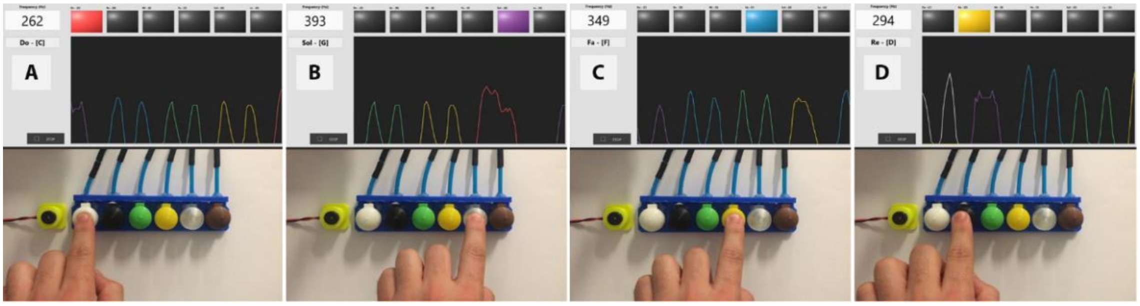

Fig. 11.11. Soft interactive piano for STEM education. A user playing "Twinkle, Twinkle, Little Star" on the soft piano.

5.6.4. Haptic Soft Push Button for Rehabilitation

A simple and effective soft haptic device is developed based on a single SPPB that activates a vibration motor disc, as shown in Fig. 5.12. The vibration level of the motor varies linearly with the linear increase in the pressure when the SPPB is activated.

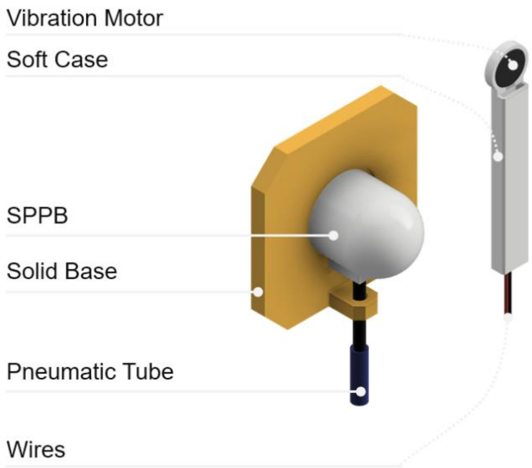

Fig. 11.12. Haptic soft push button 3D model.

The amount of pressure applied which is directly related to the level of vibration is displayed graphically using a bar graph that changes its height and color depending on the pressure applied by a user to provide visual feedback in addition to the mechanical feedback provided by the vibration motor (Fig. 5.13). This application can be useful for rehabilitation applications requiring training to gain back a sense of touch where the vibration motor disk can be placed on different body parts (Fig. 5.13D).

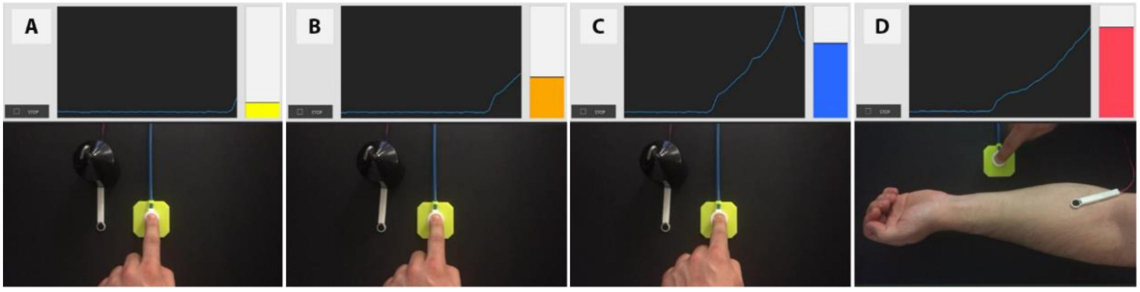

Fig. 11.13. Haptic soft push button for rehabilitation. (A to C) A user activating a vibration motor using the soft push button with mechanical and visual feedback. (D) The haptic feedback push button used with the vibration motor placed on the forearm of a user.

5.6.5. Soft Joystick for Gaming Applications

A soft joystick is fully printed and assembled based on four SPLS, as shown in Fig. 5.14 and Fig. 5.15. Each SPLS is connected to a separate pressure sensor. Ten different possible states can be achieved based on the number of SPLS activated simultaneously.

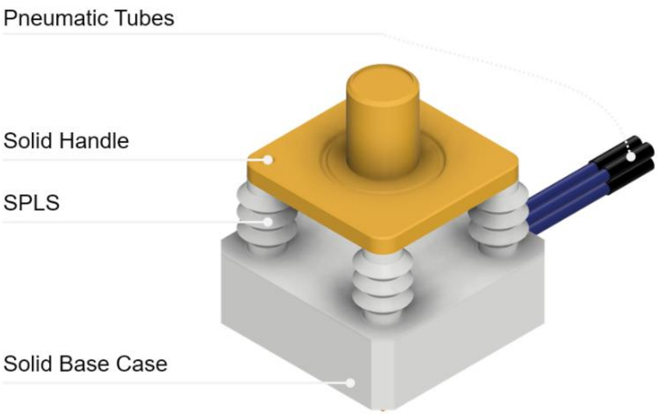

Fig. 11.14. Soft joystick 3D model.

The ten possible states include forward, forward-left, forward-right, backward, backward-left, backward-right, left, right, and brake and idle. The advantage of these game controllers is that they can be customized, designed and manufactured easily and rapidly to meet specific requirements such as shape, curvatures, size, and the number of sensors embedded in their structure.

5.6.6. Soft Throttle Controller for Gaming Applications

A soft throttle controller based on an SPTS is developed, as shown in Fig. 5.16 and Fig. 5.17. The throttle controls the rotational speed of a servo motor. The speed of the motor is proportional to the amount of twist generated by the user using the handle. The speed of the servo motor is displayed graphically and numerically. This type of throttle controllers can be used in interactive gaming applications and to control robotic systems.

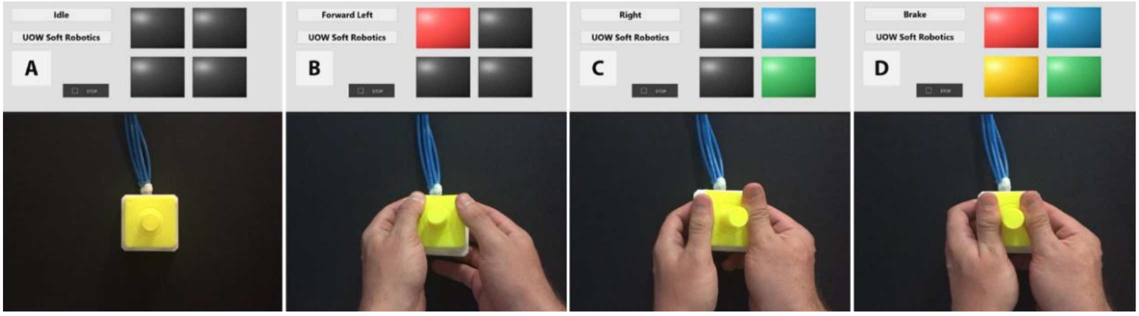

Fig. 11.15. Soft joystick for gaming applications. (A to D) 4 of the 10 possible states are achieved using the joystick and displayed on an interactive screen using virtual LEDs.

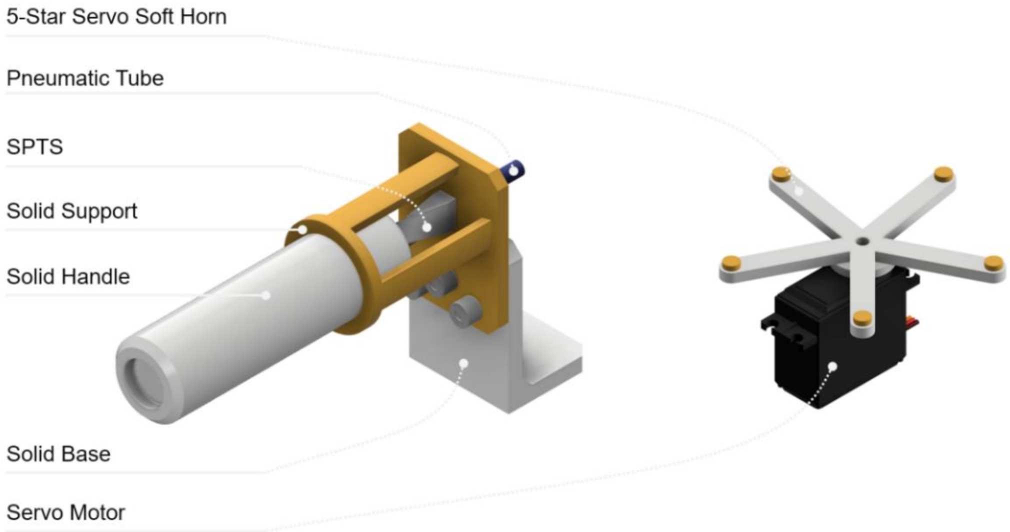

Fig. 11.16. Soft throttle controller 3D model.

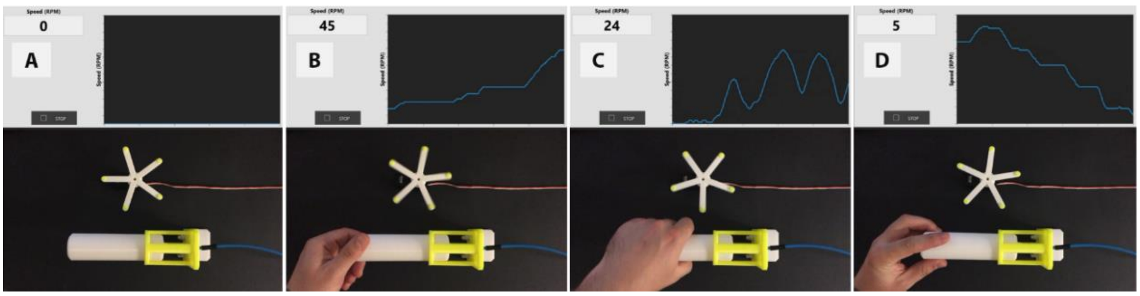

Fig. 11.17. Soft throttle controller for gaming applications. (A to D) Using the throttle controller to control the speed of a servo motor.

5.6.7. Master/Slave Soft Monolithic Robotic Fingers

A master soft monolithic robotic finger integrated with an SPBS is developed to control a tendon-driven slave monolithic robotic finger, as shown in Fig. 5.18 and Fig. 5.19.

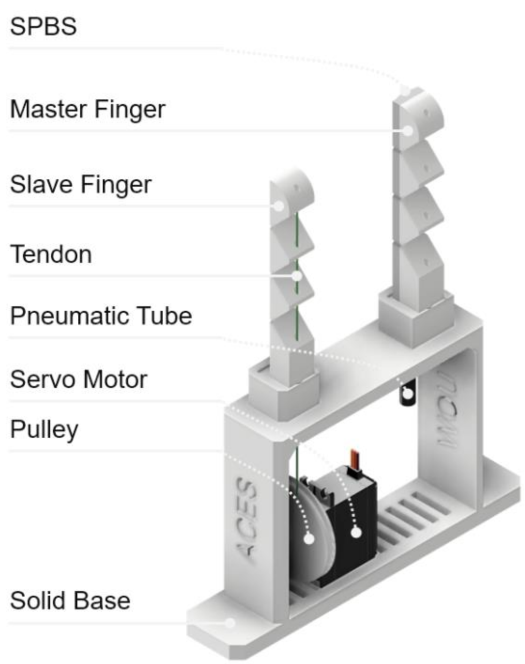

Fig. 11.18. Master/Slave soft monolithic robotic fingers 3D model.

The slave finger connected to the servo motor imitates the master finger movements by articulating it to the same position in space when it is deformed. This result proves that these bending sensors can be used with merely no control to drive soft structures with reasonable accuracy. These SPBS can be integrated into various soft structures as bending sensors.

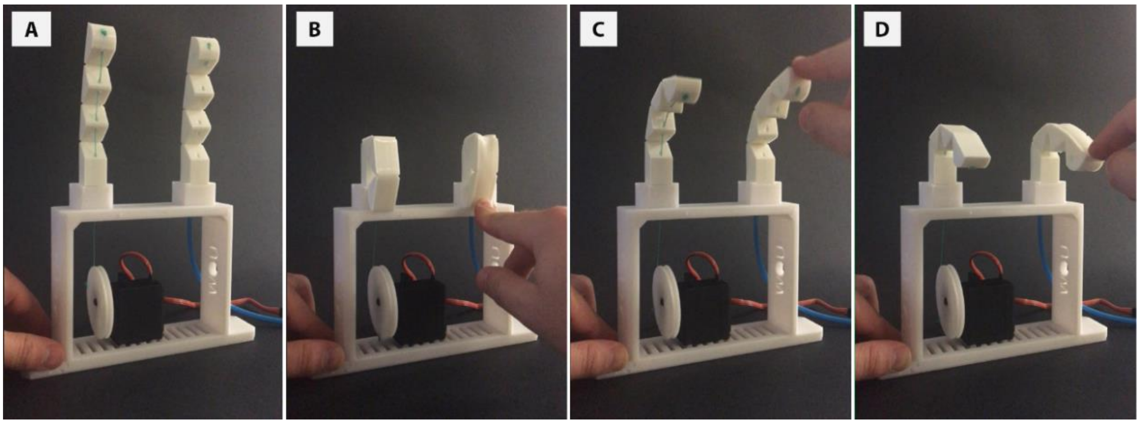

Fig. 11.19. Master/Slave soft monolithic robotic fingers. Using the master soft monolithic robotic finger (right) to drive a tendon-driven slave soft monolithic robotic finger (left).

5.7. Discussion

5.7.1. SPSC Hardware

The 3D printed SPSC presented in this study are not by themselves pressure sensors. However, these soft chambers are used in conjunction with commercially available solid air pressure sensors. Analog pressure sensors

(SSCDANN100PGAA5, 0 to 100psi Gauge, 0.25% accuracy, Honeywell International Inc.) are used to detect any volume change in the 3D printed SPSC. The hardware required to operate these SPSC in soft robotic applications includes a data acquisition system and solid air pressure sensors that sense their internal volume due to the mechanical input modalities, as shown in Fig. 5.20. The solid air pressure sensors which require a power of 13.5mW have a response time of 1.0ms [130].

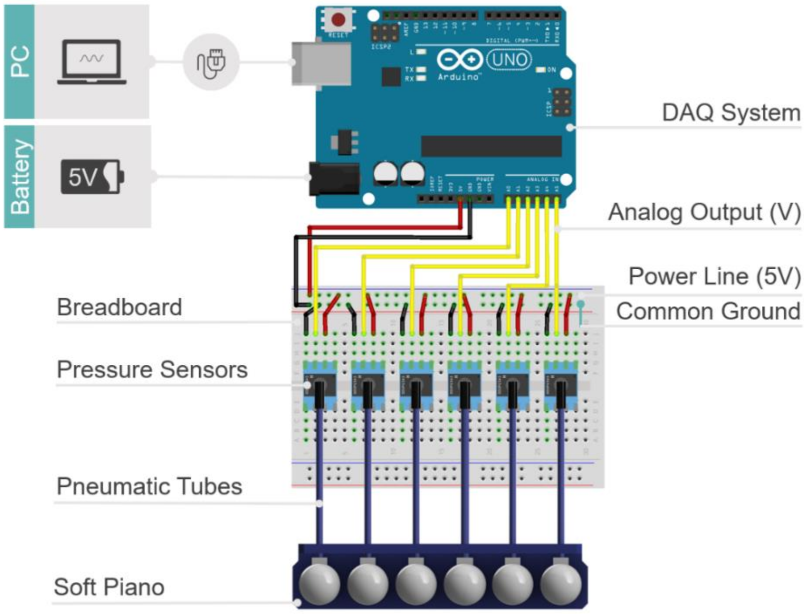

Fig. 11.20. SPSCs hardware schematic. The soft piano connected to the SPSC hardware.

5.7.2. Limitations

Since the SPSC are based on pneumatics, their operating pressure range decreases when very long connecting tubes are used between their output and their input due to pressure losses. However, this limitation can be alleviated either by placing the pressure sensors next to the SPSC or by manufacturing the SPCS with larger internal volumes. Placing the pressure sensors adjacently or within a short distance to the SPSC, especially for untethered devices will automatically eradicate this limitation. A larger internal volume will result in a higher air pressure range.

In addition, thicker walls will affect the sensitivity of the SPSC. The sensitivity of the SPCS will decrease with an increase in the thickness of their walls. Also, the stiffness of the SPSC will increase with an increase in the thickness of their walls, which in turn will affect the experience of the users as larger forces are required to deform them.

5.8. Conclusions

We have developed airtight soft pneumatic sensing chambers, SPSC, that can be directly 3D printed in one manufacturing step without requiring any support material and post-processing using a low-cost and open-source fused FDM 3D printer that uses a commercially available TPU. The SPSC can sense four main mechanical modalities of push, bending, torsional, and rectilinear displacement. These SPSC have multiple advantages, including fast response, linearity, negligible hysteresis, stability over time, repeatability, reliability, and long lifetime. The TPU used to fabricate the SPSC was characterized to understand its behavior, and a hyperelastic material model was developed for use in FEM. Based on this material model, the performance of the SPSC was optimized using FEM to obtain a linear relationship between the change in the internal volume and the input mechanical deformations applied.

The SPSC were tailored to diverse soft robotic applications and human-machine interfaces, including soft wearable glove for virtual reality applications and soft grippers, interactive devices for STEM education, haptic feedback devices for rehabilitation applications, game controllers and throttles for gaming applications, and bending sensors for master/slave soft robotic systems. These low-cost SPSC can be manufactured easily and rapidly using FDM 3D printing, which makes them ideal for hobbyists, engineers, scientists, and communities interested in STEM education and soft robotics. Also, since these soft chambers are linear, repeatable, stable over time, and exhibit insignificant hysteresis, they can be directly implemented in diverse robotic applications that require minimal power consumption without requiring sophisticated control approaches. Finally, since these SPSC are based on pneumatics, they are ideal for integration in soft robotic applications based on pneumatic actuation concepts.

Chapter 6

3D Printable Soft Monolithic Robotic Fingers

6.1. Introduction

Due to the control performance limitations in soft robotics, almost all robotic hands in the market are based on conventional rigid mechanisms [131]. These robotic systems require complex mechanisms and laborious assembly processes since they are made of numerous components. Moreover, their complex control algorithms require various sensors to ensure safe interaction with their environment. In contrast, soft robotic systems can be directly fabricated as monolithic structures seamlessly housing soft sensors using additive manufacturing techniques where minimal or no assembly is needed. This fabrication approach makes soft robotic systems cost-effective, customizable, and lightweight compared to conventional robotic systems [65, 132].

We present a tendon-driven soft monolithic robotic finger embedded with soft pneumatic self-sensing hinges for position sensing and soft touch chambers for mechanical pressure sensing that was 3D printed in one manufacturing step without requiring any post-processing and using a low-cost and open-source FDM 3D printer. This work combines the soft robotic principles involved in developing robotic hands [132] and soft sensing pneumatic chambers connected to low-profile and inexpensive pressure sensors [31]. The design of a single hinge was optimized using FEM to obtain a linear relationship between the internal change in its volume and the input mechanical modality, to minimize its bending stiffness and to maximize its internal volume. These soft self-sensing hinges have several advantages, such as fast response to a minimum change (~0.0026 ml/°) in their internal volume, linearity, negligible hysteresis, repeatability, reliability, and long lifetime. The flexion of the soft robotic finger at its joints or hinges is represented by a geometric model for use in real-time control. The real-time position and pressure/force control of the soft robotic finger were achieved using feedback signals from the soft pneumatic self-sensing hinges and touch pressure sensor. The results demonstrated in this work can be extended to other soft robotic systems where position and force feedback control systems are required. Moreover, lightweight, low-cost, and low foot-print soft robotic hands can be developed based on the soft robotic finger proposed.

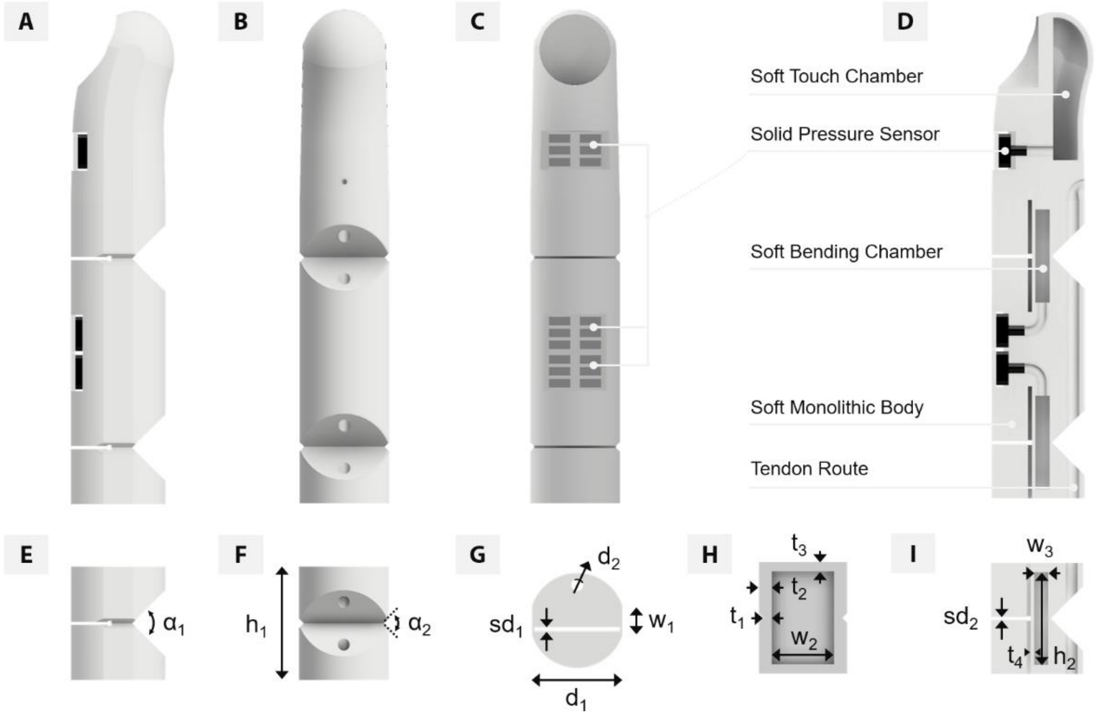

Fig. 12.1. Soft robotic finger with self-sensing pneumatic chambers. (A) Side view (B) Front view (C) Back view (D) Cross-sectional view. A single self-sensing hinge (E) side view, (F) front view, (G) top view, (H) back cross-sectional view, and (I) side cross-sectional view. Dimensions: α_1: 90°, α_2: 90°, h_1: 24.0, h_2: 20.0, sd_1: 0.80, sd_2: 0.60, d_1: 20.0, d_2: 2.50, w_1: 6.24, w_2: 13.40, w_3: 3.0, t_1: 1.80, t_2: 2.80, t_3: 2.0, t_4: 0.80. The thickness of the touch chamber thin wall is 1.20. All dimensions are in mm.

6.2. Developing Soft Monolithic Robotic Finger with Self-Sensing Chambers

We aim to design, fabricate, model and control a soft monolithic robotic finger with self-sensing soft pneumatic sensing chambers embedded in its hinges or joints, and to control the tip force using the touch sensing chambers embedded in its tip. The soft robotic finger and the soft chambers are directly fabricated as a monolithic body in one manufacturing step using a low-cost FDM 3D printer.

6.3. Modeling and Fabrication

The soft self-sensing hinges and the monolithic robotic finger are designed and modeled in Autodesk Fusion 360 (Autodesk Inc.). The minimum wall thickness of the embedded soft chambers considered during the design process is 0.8mm, which is needed to ensure that the 3D printed soft chambers are airtight. The dimensions of the self-sensing hinge and the monolithic robotic finger are shown in Fig. 6.1. The printing parameters are listed in Table 6.1. A low-cost and open-source FDM 3D printer (FlashForge Creator Pro, FlashForge Corporation, China) is used to print the soft hinges and the finger.

Table 12.1. Optimized printing parameters for 3D printing soft monolithic robotic fingers with self-sensing pneumatic chambers.

Parameter	Value	Unit
Resolution Settings		
Primary Layer Height	0.1	mm
First Layer Height	0.09	mm
First Layer Width	0.125	mm
Extrusion Width	0.4	mm
Ooze Control		
Coast at End	0.2	mm
Retraction Settings		
Retraction Length	4	mm
Retraction Speed	40	mm/s
Speed Settings		
Default Printing Speed	10	mm/s
Outline Printing Speed	8	mm/s
Solid Infill Speed	8	mm/s
First Layer Speed	8	mm/s
X/Y Axis Movement Speed	50	mm/s
Z-Axis Movement Speed	20	mm/s
Temperature Settings		
Printing Temperature	240	°C
Heat Bed Temperature	32	°C
Cooling Settings		
Fan Speed	100	%
Infill Settings		
Infill Percentage	0	%
Infill/Perimeter Overlap	30	%
Thin Walls and Movements Behavior		
Allowed Perimeter Overlap	15	%
External Thin Wall Type	Perimeters Only	-
Internal Thin Wall Type	Allow Single Extrusion Fill	-
Avoid Crossing Outline	ENABLED	-
Detour Factor	100	-
Additional Settings		
Extrusion Multiplier	1.15	-
Top Solid Layers	12	-
Bottom Solid Layers	12	-
Outline/Perimeter Shells	5	-
Wipe Nozzle	DISABLED	-
Support Material Generation		
Support Type	From Build Platform Only	-

6.4. Finite Element Modeling

The design of a single self-sensing hinge is optimized using FEM to obtain a linear relationship between the change in its internal volume and the input mechanical deformation, minimize its bending stiffness, and maximize its internal volume. Ideally, a relationship exists between the change in the internal volume of the soft chamber and the experimental pressure change ($P_1V_1 = P_2V_2$) obtained due to the mechanical deformation applied. The initial design of the hinge shown in Fig. 6.2 produced a nonlinear relationship between the change in volume and the bending angle, as shown in Fig. 6.3. However, successive improvements and modifications to the finger design ultimately produced a linear relationship between the change in volume and the bending angle, as shown in Fig. 6.4. The final design of the self-sensing hinge is shown in Fig. 6.1.

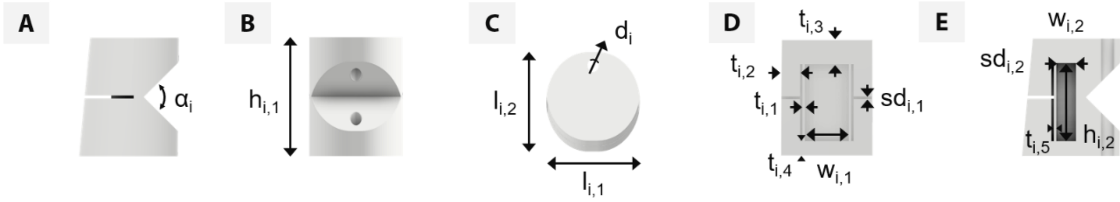

Fig. 12.2. Self-sensing pneumatic chamber initial design. (A) Side view (B) Front view (C) Top view (D) Back cross-sectional view (E) Side cross-sectional view. Dimensions: αi: 90°, hi,1: 23.87, hi,2: 15.84, li,1: 18.67, li,2: 17.79, di: 2.65, sdi,1: 0.60, sdi,2: 0.50, wi,1: 9.0, wi,2: 4.0, ti,1: 0.50, ti,2: 3.86, ti,3: 5.0, ti,4: 3.0, ti,5: 0.50. All dimensions are in mm.

The wall thickness (t_2) is the main critical parameter affecting the linearity of the relationship between the bending angle and the corresponding volume change. The wall thickness of the side walls (t_2 or $t_{i,1}$ for the initial design shown in Fig. 6.2) must be large enough compared to the wall thickness of the thin wall (t_4) to prevent the side walls from deforming inward toward each other when the hinge bends. Also, the separation of the thin wall (t_4) from the back part of the hinge (sd_1) is critical for achieving linearity. The thin wall should be free from any constraints along its length, which is not the case for the initial design. Moreover, the thickness of the side walls (t_2) is decreased to a minimum that ensures linearity but minimizes the bending stiffness of the joint. Thicker side walls result in a higher bending stiffness. Finally, the upper and lower parts of the hinge were separated (sd_2) to reduce the bending stiffness.

The models are meshed using higher-order tetrahedral elements. In terms of boundary conditions, a Fixed Support is applied at the base of the soft hinge, and a Displacement Support normal to the base of the hinge is applied at the base of the tendon. A displacement of 12.0mm was applied. Moreover, frictional and bonded contact pairs are defined. A frictional symmetric contact pair is defined between the internal walls of the soft chamber. A similar contact pair is defined between the outer walls of the hinge that come in contact upon full closure. Another frictional and symmetric contact pair is defined between the bottom hole of the hinge and the tendon. Additionally, a bonded contact pair is defined between the top hole of the hinge and the tendon.

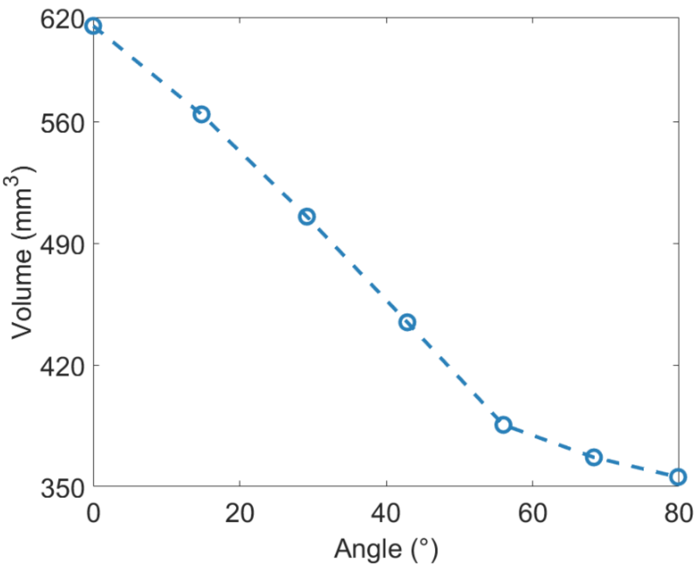

Fig. 12.3. Volume change versus bending angle for the initial hinge design. This initial design is shown in Fig. 6.2.

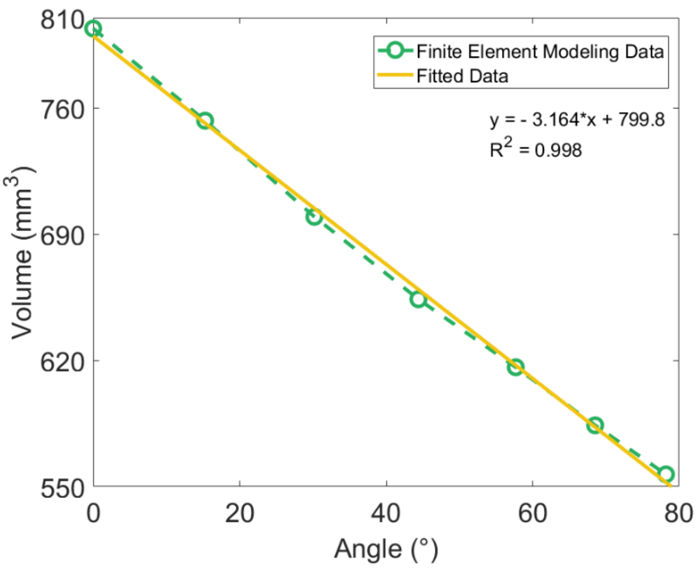

Fig. 12.4. Volume change versus bending angle for the optimized hinge. This final design is shown in Fig. 6.1.

The only challenges encountered were the distortion of some elements due to the large mechanical deformations and the contact between the soft hinge and the tendon. However, this issue was alleviated by incorporating a coarser mesh for the hinge that is suitable for hyperelastic materials and a finer mesh for the tendon. The mesh used was selected to verify that the results are accurate and not affected by its size. Therefore, FEM can be used to predict the behavior of the self-sensing hinges and to optimize their topology to meet specific design requirements quickly and efficiently before developing physical prototypes.

6.5. Characterization

A single optimized self-sensing pneumatic hinge is characterized to assess its performance in terms of linearity, hysteresis, repeatability, reliability, stability over time, and lifetime.

6.5.1. Linearity and Hysteresis

A single self-sensing hinge was activated to assess its linearity and hysteretic behavior. The input mechanical deformation was ramped up and down using a step angle of 10°. Fig. 6.5 shows that there is a linear relationship between the output pressure and the input mechanical deformation. In addition, Fig. 6.5 shows that the hinge has a negligible hysteresis. These features, linearity and negligible hysteresis, are essential for the implementation of direct and simple linear control systems.

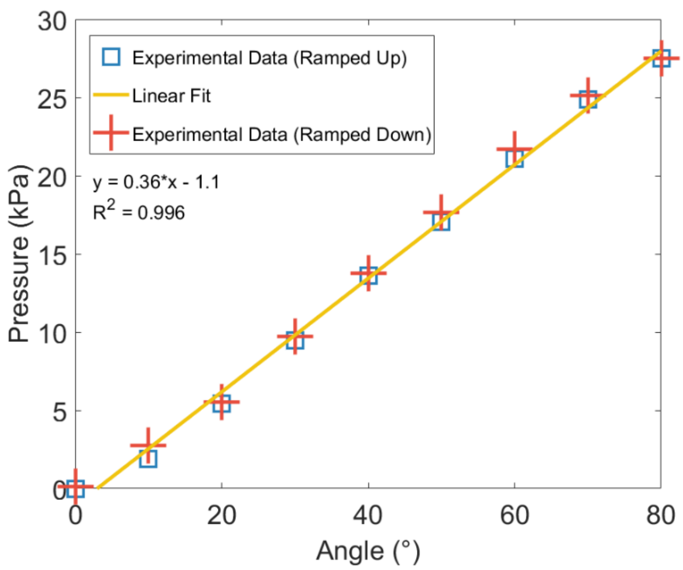

Fig. 12.5. Pneumatic hinge linearity and hysteresis experimental results.

6.5.2. Repeatability and Reliability

A single self-sensing hinge was activated repeatedly for 600 cycles (i.e., 10 minutes) with an activation frequency of 1.0Hz to assess its repeatability and reliability. In each activation cycle, the hinge was fully closed. Fig. 6.6 shows that the hinge generated a consistent and repeatable signal. However, there was a slight change in the pressure upon recovery, as shown in Fig. 6.7. The main reason for this change is that the hinge did not have enough time to recover its initial shape due to the material properties of the TPU. Although NinjaFlex is soft and flexible, it cannot recover its initial shape as fast as soft silicones when thick structures are involved. Therefore, this behavior is observed due to the thick side walls presented in the hinge and the integration of the chamber in the finger. The overall stiffness of the hinge is much larger compared to the stiffness of the structures presented earlier. The previous structures (i.e., SOVA, LSOVA, and SPSC) have thin walls that would quickly and almost completely recover their initial shape when an applied load is removed.

6.5.3. Drift Over Time

A single self-sensing hinge was fully closed for 30 minutes, while its internal pressure was monitored to check for any drift over time. The pressure changed by 2.41% during the actuation period, as shown in Fig. 6.8. The main reason for this slight change over time is that when the hinge was fully closed, the tendon was loosened slightly due to the stretch and relaxation of the TPU at the hole of the hinge where the tendon is running. This effect had only a minor influence on the holding pressure, which is promising as pressure stability is essential to develop reliable control systems for soft robotic systems.

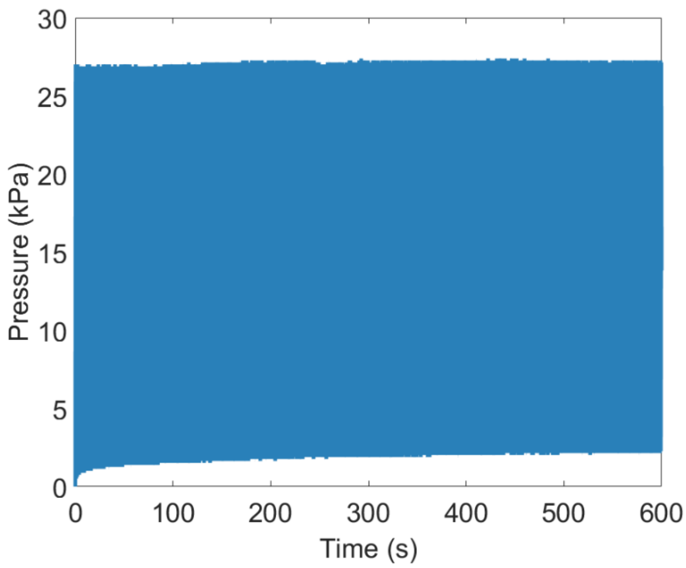

Fig. 12.6. The repeatability of the pressure change in the hinge. The repeatability signal for 600 bending cycles.

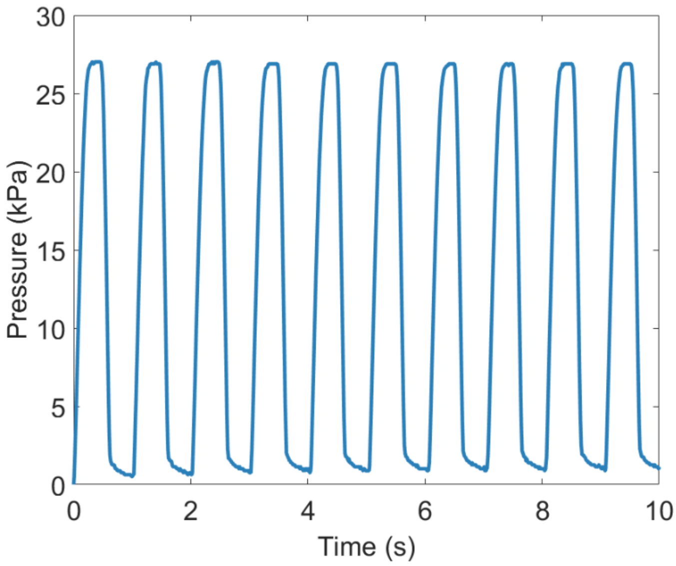

Fig. 12.7. The repeatability of the pressure change in the hinge. The repeatability signal for typical 10 bending cycles.

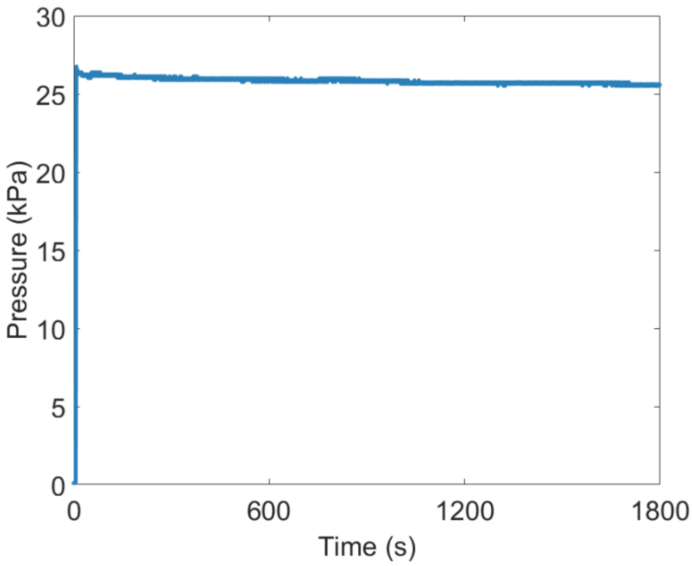

Fig. 12.8. The pressure stability of the self-sensing hinge over time.

6.5.4. Lifetime

A single self-sensing pneumatic hinge was activated repeatedly with a frequency of 1.0Hz to assess its lifetime. In each cycle, the hinge was fully closed and relaxed. The hinge sustained 100,000 cycles without failure and any degradation in performance. In a previous study [132], we have shown that a similar flexure hinge without pneumatic chambers can sustain more than 1.5 million cycles without any degradation in performance or structural damage. Therefore, these self-sensing hinges are ideal for reliable soft robotic applications such as soft robotic hands, soft prosthetic hand, and soft adaptive grippers that require repeatable deformations over sustained periods.

6.6. Soft Robotic Finger Modeling

The soft robotic finger can be modeled using the direct relationship between the output pressure and the angular displacement for each joint (Fig. 6.9) with reference to the experimental result in Fig. 6.5. The angular position of each joint can be obtained directly from the corresponding pressure readings as follows:

$$\theta_1 = \alpha_1 P_1 + \beta_1 \tag{6.1}$$

$$\theta_2 = \alpha_2 P_2 + \beta_2 \tag{6.2}$$

where θ_1 is the angular position of Hinge 1, θ_2 is the angular position of Hinge 2, P_1 is the pressure for Hinge 1, P_2 is the pressure for Hinge 2, and α_1, β_1, α_2 and β_2 are the constants of the linear model, which are experimentally identified to be 2.6548, -5.5752, 2.4931, and -4.9861 °/kPa, respectively.

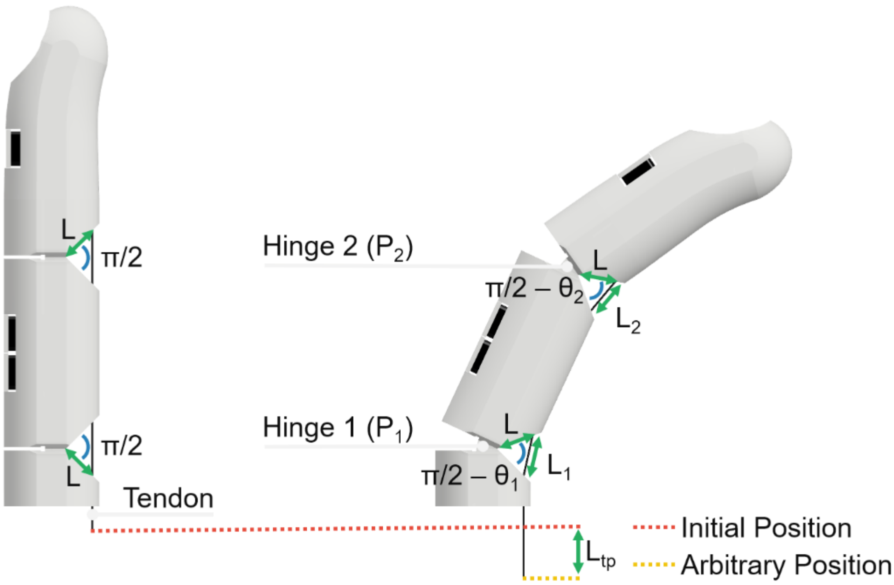

Fig. 12.9. The geometric model parameters for the soft robotic finger.

A geometric model can be derived (Fig. 6.9) to obtain a relationship between the change in the length of the tendon at each joint and the corresponding bending angle as follows:

$$L_1 = L\sqrt{2[1 - \cos(\pi/2 - \theta_1)]} \tag{6.3}$$

$$L_2 = L\sqrt{2[1 - \cos(\pi/2 - \theta_2)]} \tag{6.4}$$

where L_1 is the length of the tendon at an arbitrary position at Hinge 1, L_2 is the length of the tendon at the same arbitrary position at Hinge 2, and L is the distance between the tendon and the pivot point of each hinge. The total change in the length of the tendon, L_{tp}, based on the model of the pressure sensors can be written as follows:

$$L_{tp} = L_1 + L_2 \tag{6.5}$$

The total change in the length of the tendon, L_{te}, can also be derived based on the data obtained from the quadrature encoder as follows:

$$L_{te} = r_p \theta_e \tag{6.6}$$

where r_p is the radius of the pulley to which the tendon is attached and θ_e is its corresponding angular displacement measured by the encoder.

The angular displacements θ_{tp} and θ_e can be expressed as follows:

$$\theta_{tp} = {}^{L_{tp}}\!/_{r_p} \tag{6.7}$$

$$\theta_e = {}^{L_{te}}\!/_{r_p} \tag{6.8}$$

where r_p = 40mm.

6.7. Soft Robotic Finger Control

The real-time position and pressure/force control experiments of the soft robotic finger are conducted using a quadrature encoder and the soft pneumatic self-sensing hinges. Proportional, Integral, Derivative (PID), and PI controllers are employed to perform the position and pressure/force control experiments, respectively. The PID control gains are tuned experimentally.

6.7.1. Position Control Based on Quadrature Encoder

The change in the length of the tendon obtained from the geometric model (i.e., angular displacement, Eq. 6.7) is compared with the change in the length of the tendon derived from the model of the encoder (Eq. 6.8). A trajectory tracking control experiment is conducted with an amplitude of pi/17 (i.e., which corresponds to the length of the tendon, Eqs. 6.7 and 6.8) and a frequency of 1.0Hz. The feedback control signal is obtained from the encoder. Fig. 6.10 shows that the motor can precisely follow the position reference when the encoder feedback is used (i.e., it is the expected result with the PID controller with the gains of k_p = 250, k_i = 5 and k_d = 10). More importantly, the measurement from the pneumatic sensors is verified with this experiment. The length of the cable (i.e., angle of the pulley) can be precisely estimated by using the proposed sensors and their corresponding geometric model (Eqs. 6.1-6.5), as shown in Fig. 6.10. The block diagram of the control loop is shown in Fig. 6.11.

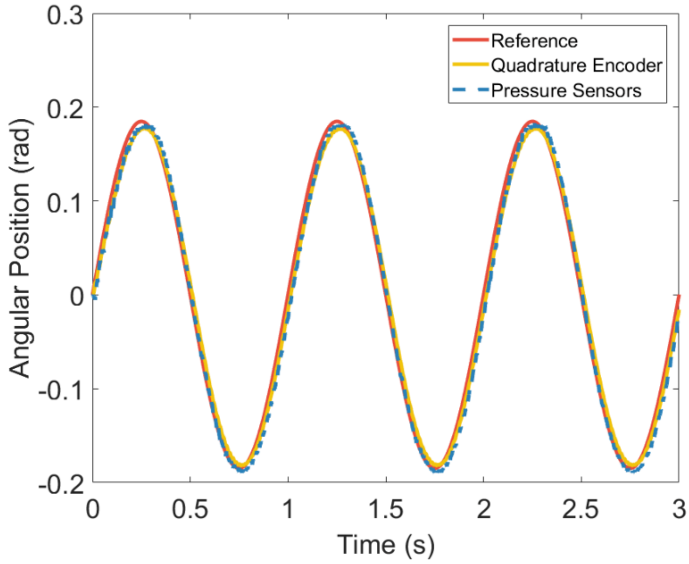

Fig. 12.10. Sensing chambers performance verification. Experimental results verifying the performance of the sensing pneumatic chambers, which provide the joint angle data to estimate the tendon length correctly from Eqs. 5 and 7. The control signal was provided by the motor encoder. Please note the close match between the encoder readings and the corresponding readings of the sensing pressure chambers.

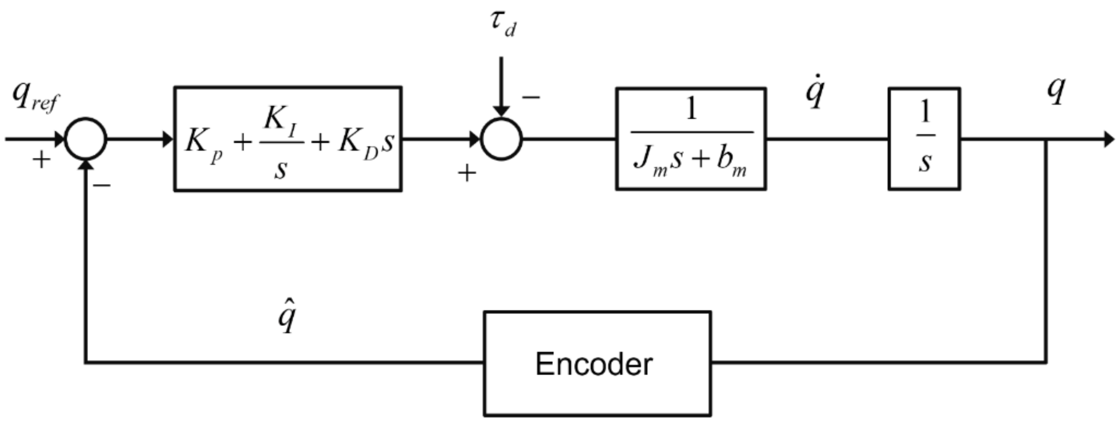

Fig. 12.11. Performance verification control loop block diagram. The performance verification of the sensing pressure chambers based on the feedback provided by the encoder.

6.7.2. Position Control Based on Geometric Model

After the geometric model (Eqs. 6.5 and 6.7) is verified, the same trajectory tracking control experiment is performed with the same applied reference input. However, the feedback signal is obtained from the pressure sensors instead of the encoder. The most significant result in this experiment is that the motor can precisely follow the reference trajectory when the pneumatic sensors' measurements are used, as shown in Fig. 6.12. Fig. 6.12 shows that high-performance trajectory tracking can be performed by using only the pneumatic sensors measurement under the PID controller with the gains of

$k_p = 55$, $k_i = 50$, and $k_d = 1$. Also, Fig. 6.12 shows that the encoder signal accurately follows the pressure sensors signal, which again verifies the accuracy of the geometric model. The block diagram of the control loop is shown in Fig. 6.13.

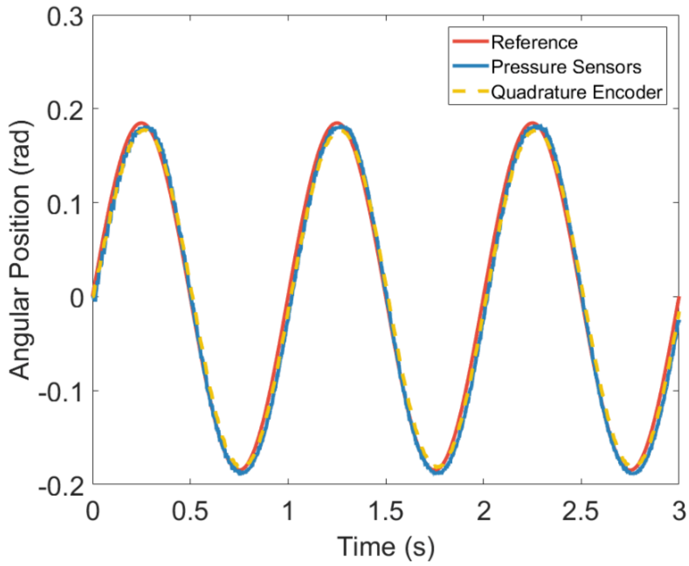

Fig. 12.12. Sensing chambers control performance verification. Experimental results verifying the control performance of the sensing chambers, which provide the joint angle feedback data to control the tendon length. The corresponding encoder readings were used to estimate the tendon length correctly from Eq. 6. Please note the close match between the readings of the sensing pressure chambers and the corresponding encoder readings.

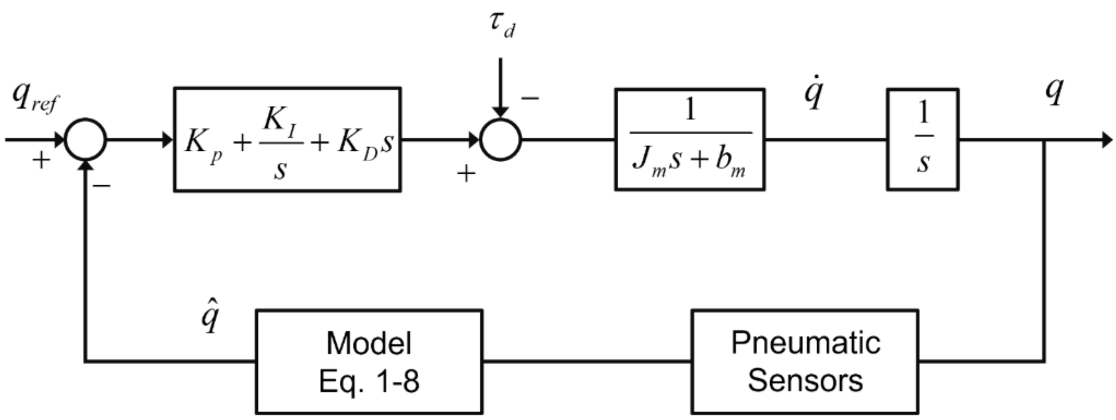

Fig. 12.13. Robotic finger control loop block diagram. Control loop block diagram for the control of the soft robotic finger based on the feedback provided by the pressure chambers.

6.7.3. Step Response Based on Geometric Model

The feedback control is performed by using the measurements from the pressure sensors where the encoder reading is used to verify the performance of the position measurement. Fig. 6.14 shows the step response of the soft finger using the feedback data provided by the sensing chambers embedded in the hinges (≈ 8.55% overshoot, 29.09ms rise time, and < 72ms settling time) under the PID controller with the gains of $k_p = 25$, $k_i = 50$, and $k_d = 1.25$.

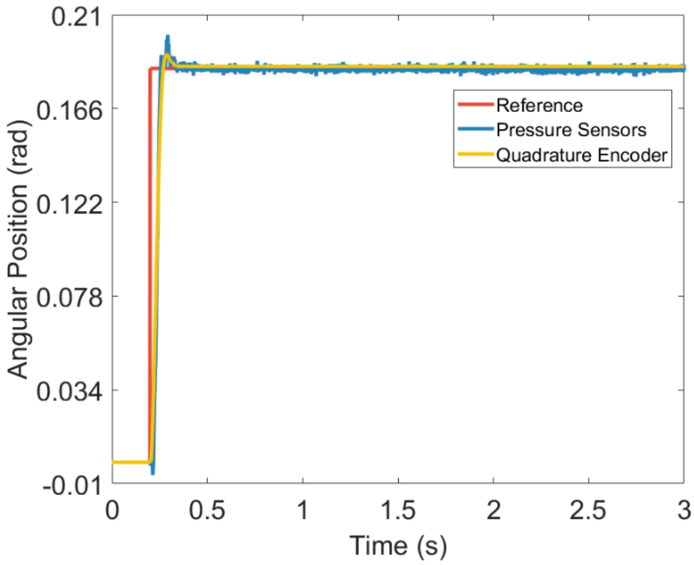

Fig. 12.14. Robotic finger step response. The step response of soft finger with feedback data provided by the sensing chambers embedded in its hinges.

6.7.4. Force/Pressure Control

The proposed pneumatic soft sensors can be used to estimate not only the position of hinges of the soft robotic finger but also its tip force/pressure. To this aim, a soft sensing chamber is embedded at the tip of the soft finger, as illustrated in Fig. 6.1. The position control is performed by using the same step reference input when there is an obstacle. The robotic finger cannot follow the position reference due to the obstacle, as shown in Fig. 6.15. The output of the pressure sensor and the estimated contact force, which is obtained by an observer, are illustrated in Fig. 6.16. This figure shows that the pressure sensor and the disturbance forces have similar characteristic curves. The block diagram of the pressure/force control loop is shown in Fig. 6.17.

As shown in Fig. 6.18, a closed-loop force control could be performed by using the soft touch sensor. The closed-loop force/pressure control is achieved using an experimentally tuned PI controller with the gains of $k_p = 0.75$ and $k_i = 6$. It is proven that soft pneumatic sensors can be modeled and used as force sensors [107, 108]. In this chapter, the main objective is to characterize fully, model, and implement the proposed soft position sensors. The pressure/force sensor introduced in this section showed its potential as a force sensor.

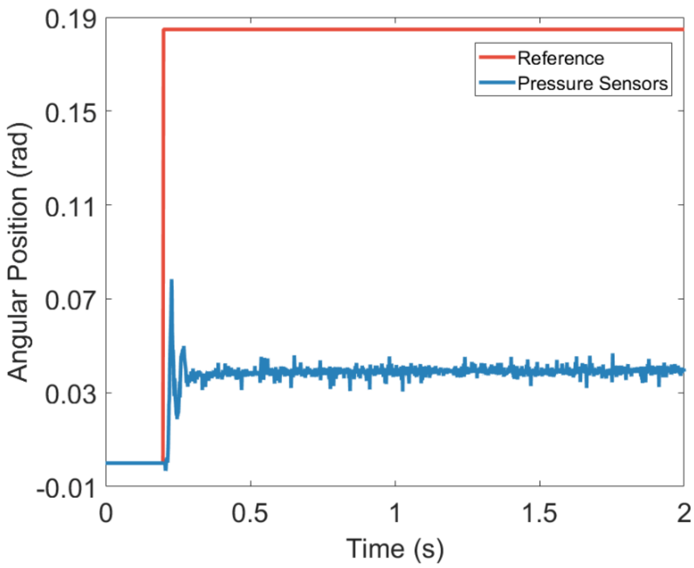

Fig. 12.15. Soft finger position after an obstacle is encountered.

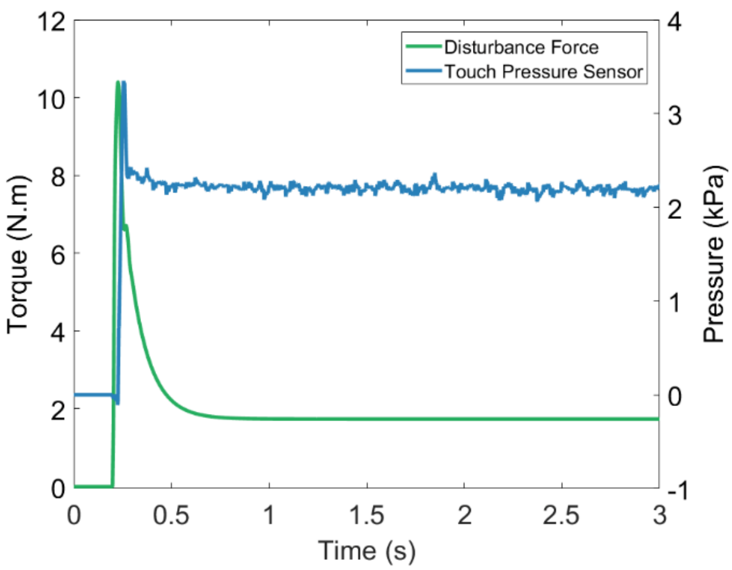

Fig. 12.16. Computed torque and touch sensor characteristic curves.

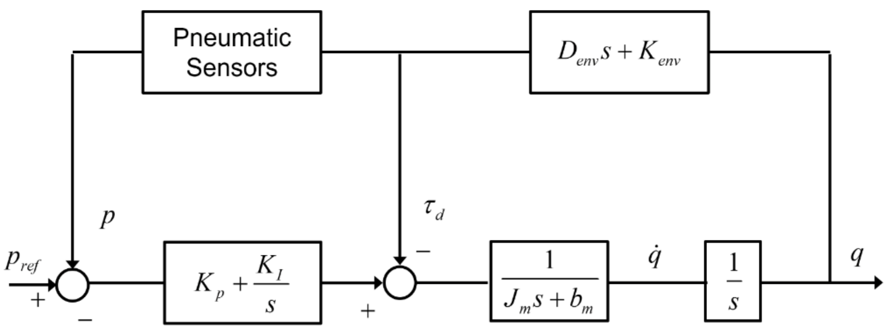

Fig. 12.17. Pressure/force control loop block diagram.

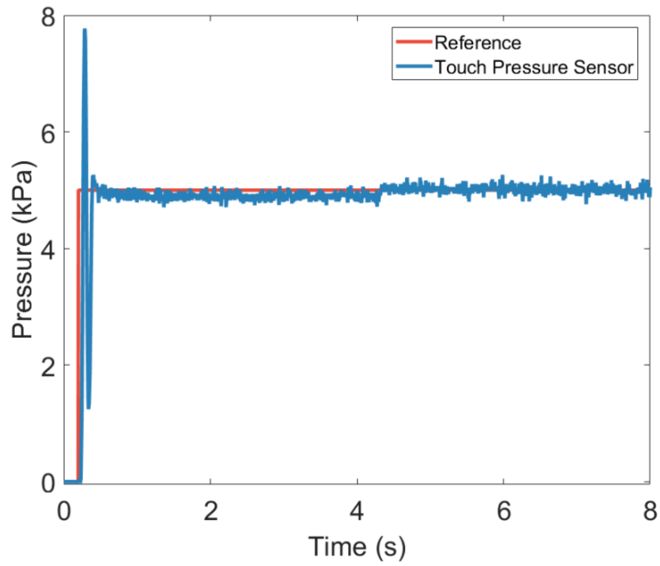

Fig. 12.18. Closed-loop force control based on the touch pressure sensor.

It is important to note that only pressure control is performed (i.e., force control is not directly performed). In order to perform force control, the touch pressure sensor should be modeled to measure the corresponding force. This pressure control result proves that force control can be performed by using the pneumatic touch sensor embedded in the tip of the soft robotic finger.

6.8. Discussion

The self-sensing pneumatic chambers used in this chapter are not by themselves soft sensors [31]. Commercial pressure sensors are employed to measure the pressure in the soft chambers, as shown in Fig. 6.1 and to control the position and force/pressure of the robotic finger. One limitation of the solid pressure sensors is their relatively noisy signal, which needs to be appropriately processed before it can be used for the control purpose. The soft pneumatic self-sensing chambers can be used in soft robotic applications where soft position and force sensors are required [31].

6.9. Conclusions

We have developed a monolithic soft robotic finger embedded with soft pneumatic sensing chambers that can be used for position and force control. The soft finger was 3D printed directly, without requiring any post-processing, using a low-cost and open-source FDM 3D printer. A self-sensing hinge was optimized using FEM to obtain a linear relationship between the internal change in its volume and the input mechanical deformation, to minimize its bending stiffness and to maximize its internal volume. FEM simulations were performed to predict the behavior of the self-sensing hinges accurately. The monolithic self-sensing hinges have multiple advantages, such as fast response to a minimum change of ~0.0026 ml/° in their internal volume due to mechanical deformations, linearity, insignificant hysteresis, repeatability, reliability and long lifetime. A geometric model for the tendon length has been proposed and experimentally verified for the real-time control and actuation of the soft robotic finger. The feedback signals from the soft pneumatic self-sensing hinges and the touch pressure sensor were used to control the position and the tip force of the soft robotic finger in real-time.

This work has demonstrated that these soft pneumatic self-sensing chambers can seamlessly be integrated into soft robotic systems to control their position and force. These robotic fingers can be used in diverse applications, including soft prosthetic hands, robotic hands, and adaptive grippers.

Chapter 7

Conclusions and Future Work

7.1. Conclusions

Based on the work presented in this thesis, the following conclusions are drawn:

This thesis has presented 3D printed soft pneumatic actuators and sensors that can be used in diverse soft robotic applications. The proposed actuators and sensors were fabricated directly, without requiring support material and post-processing, using open-source and low-cost FDM 3D printers that employ an off-the-shelf soft and commercially available TPU. The fabrication technique used was explained, and the optimized printing parameters were presented. The TPU used was characterized to obtain its stress-strain relationship to develop a hyperelastic material model for use in finite element simulations, as described in Chapter 2. The actuators and sensors were characterized, and their performance was optimized and predicted using finite element models and analytical models in some cases. Chapter 3 and Chapter 4 have presented the soft actuators developed, their modeling, characterization, and applications in diverse soft robotic applications. The actuators were designed to be activated using negative pressure instead of positive pressure as in conventional soft pneumatic actuators. Chapter 5 has presented the soft pneumatic sensing chambers developed, their modeling, characterization, and applications in diverse human-machine interfaces. Chapter 6 has presented the design, modeling, fabrication, and control of a soft monolithic robotic finger with embedded soft pneumatic sensing chambers. The soft chambers were implemented as position and touch sensors for position and pressure control. The soft chambers provided a reliable and stable signal that was used to accurately and precisely control the position and contact pressure of the soft robotic finger.

One of the main aims of soft robotics is to design and fabricate soft robotic systems with a monolithic topology embedded with actuators and sensors such that they can safely interact with their immediate physical environment. The results presented in this thesis significantly contribute to the research efforts to achieve this overarching aim. The sensors are seamlessly integrated into the monolithic topology of the soft finger for the position and force control, which ideally require co-located sensors, as demonstrated in this study. Also, our aim is to fabricate low-cost, lightweight, and low-foot-print soft monolithic structures with embedded self-sensing capabilities using low-cost and open-source 3D printing technologies. This thesis has shown that these low-cost soft robotic systems can be easily and rapidly designed, modeled, fabricated, and controlled which make them suitable to be directly implemented by roboticists, engineers and hobbyists in diverse robotic applications such as robotic hands, soft prosthetic hands, soft prosthetic fingers, adaptive grippers, locomotion robots, artificial muscles, modular robots, wearable sensors and interactive human-machine interfaces.

7.2. Recommendations for Future Work

Our future aim is to 3D print the structure, actuators, sensors, and other soft electronic components simultaneously in one manufacturing step. This work is one step towards developing fully 3D printable soft robots in one manufacturing step. However, there is some remaining research work that can be conducted based on the work presented.

- The soft actuators developed can be further optimized to achieve the desired stiffness, to pave the way towards robotic systems with programmable compliance. Their stiffness cannot be changed actively to produce the desired force output. Therefore, variable stiffness structures should be designed as part of the geometry of the actuators or integrated into their main structure to enhance their performance.

- The pneumatic sensing chambers were equipped with commercially available solid air pressure sensors. In future work these solid sensors can be replaced by a soft resistive or capacitive material that acts as a pressure sensor, seamlessly integrated in the robotic mechanism or soft robotic element (e.g., a finger of a prosthetic hand) to measure the air pressure, and subsequently control the contact force between soft robotic systems and their physical environment.

- The nonlinear relationship between the negative input pressure and the stroke (i.e., displacement) of LSOVAs should be addressed, either through optimizing their geometry or modeling their nonlinear behavior so that they can be used in control applications. Although the hysteretic behavior can be modeled and dealt with using proper control algorithms, this approach will make the control work more challenging. Therefore, one of our future aims is to optimize the geometry of the actuators to eliminate their nonlinear behavior so that they can be directly controlled without requiring complicated models and sophisticated control algorithms.

- For the soft robotic monolithic finger, flexible and thin wires were used to connect the pressure sensors to the data acquisition system. These wires can be replaced by conductive traces that can be directly printed on the surface of the structure.

- The TPU used in this study to 3D print the soft actuators and sensors can be replaced by other 3D printable soft materials to optimize further and quantify the performance of the actuators and sensors based on different materials and more importantly establish multi-purpose actuators and sensors, and eventually soft robotic systems.

- The 3D printing technology used can be replaced by other 3D printing methods that use soft materials.

- Various soft robotic technologies can be developed based on the demonstrations presented in this work.

In summary, the soft pneumatic actuators and sensors developed can provide a foundation on which future soft robotic devices for diverse applications can be rapidly and efficiently designed, modeled, built, and controlled.

References

[1] B. Trimmer, "Soft robots," *Current Biology,* vol. 23, no. 15, pp. R639-R641, 2013.

[2] D. Rus and M. T. Tolley, "Design, fabrication and control of soft robots," *Nature,* vol. 521, pp. 467-475, 2015.

[3] B. Guanjun *et al.*, "Soft Robotics: Academic Insights and Perspectives Through Bibliometric Analysis," *Soft Robotics,* vol. 5, no. 3, pp. 229-241, 2018.

[4] S. I. Rich, R. J. Wood, and C. Majidi, "Untethered soft robotics," *Nature Electronics,* vol. 1, no. 2, pp. 102-112, 2018.

[5] C. Lee *et al.*, "Soft robot review," *International Journal of Control, Automation and Systems,* vol. 15, no. 1, pp. 3-15, 2017.

[6] C. Laschi, B. Mazzolai, and M. Cianchetti, "Soft robotics: Technologies and systems pushing the boundaries of robot abilities," *Science Robotics,* vol. 1, no. 1, p. eaah3690, 2016.

[7] D. Trivedi, C. D. Rahn, W. M. Kier, and I. D. Walker, "Soft Robotics: Biological Inspiration, State of the Art, and Future Research," *Applied Bionics and Biomechanics,* vol. 5, no. 3, pp. 99-117, 2008.

[8] S. Coyle, C. Majidi, P. LeDuc, and K. J. Hsia, "Bio-inspired soft robotics: Material selection, actuation, and design," *Extreme Mechanics Letters,* vol. 22, pp. 51-59, 2018.

[9] S. Kim, C. Laschi, and B. Trimmer, "Soft robotics: a bioinspired evolution in robotics," *Trends in Biotechnology,* vol. 31, no. 5, pp. 287-294, 2013.

[10] G. Alici, "Softer is Harder: What Differentiates Soft Robotics from Hard Robotics?," *MRS Advances,* vol. 3, no. 28, pp. 1557-1568, 2018.

[11] C. Majidi, "Soft-Matter Engineering for Soft Robotics," *Advanced Materials Technologies,* vol. 4, no. 2, p. 1800477, 2019.

[12] F. Schmitt, O. Piccin, L. Barbé, and B. Bayle, "Soft Robots Manufacturing: A Review," *Frontiers in Robotics and AI,* vol. 5, p. 84, 2018.

[13] T. J. Wallin, J. Pikul, and R. F. Shepherd, "3D printing of soft robotic systems," *Nature Reviews Materials,* vol. 3, no. 6, pp. 84-100, 2018.

[14] J. Z. Gul *et al.*, "3D printing for soft robotics – a review," *Science and Technology of Advanced Materials,* vol. 19, no. 1, pp. 243-262, 2018.

[15] A. Zolfagharian, A. Z. Kouzani, S. Y. Khoo, A. A. A. Moghadam, I. Gibson, and A. Kaynak, "Evolution of 3D printed soft actuators," *Sensors and Actuators A: Physical,* vol. 250, pp. 258-272, 2016.

[16] M. T. Tolley *et al.*, "A Resilient, Untethered Soft Robot," *Soft Robotics,* vol. 1, no. 3, pp. 213-223, 2014.

[17] H. Lipson, "Challenges and Opportunities for Design, Simulation, and Fabrication of Soft Robots," *Soft Robotics,* vol. 1, no. 1, pp. 21-27, 2013.

[18] F. Iida and C. Laschi, "Soft Robotics: Challenges and Perspectives," *Procedia Computer Science,* vol. 7, pp. 99-102, 2011.

[19] C. Majidi, "Soft Robotics: A Perspective—Current Trends and Prospects for the Future," *Soft Robotics,* vol. 1, no. 1, pp. 5-11, 2013.

[20] G.-Z. Yang *et al.*, "The grand challenges of Science Robotics," *Science Robotics,* vol. 3, no. 14, p. eaar7650, 2018.

[21] R. Pfeifer, M. Lungarella, and F. Iida, "The challenges ahead for bio-inspired 'soft' robotics," *Communication of the ACM,* vol. 55, no. 11, pp. 76-87, 2012.

[22] S. Bauer, S. Bauer-Gogonea, I. Graz, M. Kaltenbrunner, C. Keplinger, and R. Schwödiauer, "25th Anniversary Article: A Soft Future: From Robots and Sensor Skin to Energy Harvesters," *Advanced Materials,* vol. 26, no. 1, pp. 149-162, 2014.

[23] N. Lu and D.-H. Kim, "Flexible and Stretchable Electronics Paving the Way for Soft Robotics," *Soft Robotics,* vol. 1, no. 1, pp. 53-62, 2013.

[24] M. D. Dickey, "Stretchable and Soft Electronics using Liquid Metals," *Advanced Materials,* vol. 29, no. 27, p. 1606425, 2017.

[25] W. Wu, "Stretchable electronics: functional materials, fabrication strategies and applications," *Science and Technology of Advanced Materials,* vol. 20, no. 1, pp. 187-224, 2019.

[26] W.-J. Song *et al.*, "Recent Progress in Stretchable Batteries for Wearable Electronics," *Batteries & Supercaps,* vol. 2, no. 3, pp. 181-199, 2019.

[27] C. Tawk, M. in het Panhuis, G. M. Spinks, and G. Alici, "Bioinspired 3D Printable Soft Vacuum Actuators for Locomotion Robots, Grippers and Artificial Muscles," *Soft Robotics,* vol. 5, no. 6, pp. 685-694, 2018.

[28] C. Tawk, G.M. Spinks, M. in het Panhuis, and G. Alici, "3D Printable Linear Soft Vacuum Actuators (LSOVA): their modeling, performance quantification and application in soft robotic systems," *IEEE/ASME Transactions on Mechatronics,* vol. 24, no. 5, pp. 2118-2129, 2019.

[29] C. Tawk, G.M, Spinks, M. in het Panhuis, and G. Alici, "3D Printable Vacuum-Powered Soft Linear Actuators," in 2019 *IEEE/ASME International Conference on Advanced Intelligent Mechatronics*. 2019, pp. 50-55.

[30] C. Tawk, A. Gillett, M. in het Panhuis, G.M, Spinks, and G. Alici, "A 3D-Printed Omni-Purpose Soft Gripper", *IEEE Transactions on Robot*ics, vol. 35, no. 5, pp. 1268-1275, 2019.

[31] C. Tawk, M. in het Panhuis, G. M. Spinks, and G. Alici, "Soft Pneumatic Sensing Chambers for Generic and Interactive Human–Machine Interfaces," *Advanced Intelligent Systems,* vol. 1, no. 1, p. 1900002, 2019.

[32] C. Tawk, H. Zhou, E. Sariyildiz, M. in het Pnahuis, G. M. Spinks, and G. Alici, "Design, Modeling and Control of a 3D Printed Monolithic Soft Robotic Finger with Pneumatic Self-Sensing Chambers," *IEEE Transactions on Robotics*, Under Review, 2019.

[33] H. K. Yap, H. Y. Ng, and C.-H. Yeow, "High-Force Soft Printable Pneumatics for Soft Robotic Applications," *Soft Robotics,* vol. 3, no. 3, pp. 144-158, 2016.

[34] B. A. W. Keong and R. Y. C. Hua, "A Novel Fold-Based Design Approach toward Printable Soft Robotics Using Flexible 3D Printing Materials," *Advanced Materials Technologies,* vol. 3, no. 2, p. 1700172, 2018.

[35] R. MacCurdy, R. Katzschmann, K. Youbin, and D. Rus, "Printable hydraulics: A method for fabricating robots by 3D co-printing solids and liquids," in *2016 IEEE International Conference on Robotics and Automation (ICRA)*, 2016, pp. 3878-3885.

[36] Z. Wang and S. Hirai, "Soft Gripper Dynamics Using a Line-Segment Model With an Optimization-Based Parameter Identification Method," *IEEE Robotics and Automation Letters,* vol. 2, no. 2, pp. 624-631, 2017.

[37] N. P. Bryan, J. W. Thomas, Z. Huichan, and F. S. Robert, "3D printing antagonistic systems of artificial muscle using projection stereolithography," *Bioinspiration & Biomimetics,* vol. 10, no. 5, p. 055003, 2015.

[38] M. Schaffner, J. A. Faber, L. Pianegonda, P. A. Rühs, F. Coulter, and A. R. Studart, "3D printing of robotic soft actuators with programmable bioinspired architectures," *Nature Communications,* vol. 9, no. 1, p. 878, 2018.

[39] T. J. Wallin *et al.*, "Click chemistry stereolithography for soft robots that self-heal," *Journal of Materials Chemistry B,* vol. 5, no. 31, pp. 6249-6255, 2017.

[40] L. Ge, L. Dong, D. Wang, Q. Ge, and G. Gu, "A digital light processing 3D printer for fast and high-precision fabrication of soft pneumatic actuators," *Sensors and Actuators A: Physical,* vol. 273, pp. 285-292, 2018.

[41] J. Plott and A. Shih, "The extrusion-based additive manufacturing of moisture-cured silicone elastomer with minimal void for pneumatic actuators," *Additive Manufacturing,* vol. 17, pp. 1-14, 2017.

[42] J. Morrow, S. Hemleben, and Y. Menguc, "Directly Fabricating Soft Robotic Actuators With an Open-Source 3-D Printer," *IEEE Robotics and Automation Letters,* vol. 2, no. 1, pp. 277-281, 2017.

[43] D. K. Patel, A. H. Sakhaei, M. Layani, B. Zhang, Q. Ge, and S. Magdassi, "Highly Stretchable and UV Curable Elastomers for Digital Light Processing Based 3D Printing," *Advanced Materials,* vol. 29, no. 15, p. 1606000, 2017.

[44] H. M. C. M. Anver, R. Mutlu, and G. Alici, "3D printing of a thin-wall soft and monolithic gripper using fused filament fabrication," in *2017 IEEE International Conference on Advanced Intelligent Mechatronics (AIM)*, 2017, pp. 442-447.

[45] R. Mutlu, C. Tawk, G. Alici, and E. Sariyildiz, "A 3D printed monolithic soft gripper with adjustable stiffness," in *IECON 2017 - 43rd Annual Conference of the IEEE Industrial Electronics Society*, 2017, pp. 6235-6240.

[46] L. Huai-Ti, G. L. Gary, and T. Barry, "GoQBot: a caterpillar-inspired soft-bodied rolling robot," *Bioinspiration & Biomimetics,* vol. 6, no. 2, p. 026007, 2011.

[47] C. Laschi, M. Cianchetti, B. Mazzolai, L. Margheri, M. Follador, and P. Dario, "Soft Robot Arm Inspired by the Octopus," *Advanced Robotics,* vol. 26, no. 7, pp. 709-727, 2012.

[48] J. Hu, D. Erbao, X. Min, L. Chunshan, G. Alici, and J. Yang, "Soft and smart modular structures actuated by shape memory alloy (SMA) wires as tentacles of soft robots," *Smart Materials and Structures,* vol. 25, no. 8, pp. 085026, 2016.

[49] Y. She, C. Li, J. Cleary, and H.-J. Su, "Design and Fabrication of a Soft Robotic Hand With Embedded Actuators and Sensors," *Journal of Mechanisms and Robotics,* vol. 7, no. 2, pp. 021007-021007-9, 2015.

[50] S. Seok, C. D. Onal, K. J. Cho, R. J. Wood, D. Rus, and S. Kim, "Meshworm: A Peristaltic Soft Robot With Antagonistic Nickel Titanium Coil Actuators," *IEEE/ASME Transactions on Mechatronics,* vol. 18, no. 5, pp. 1485-1497, 2013.

[51] G. Guo-Ying, Z. Jian, Z. Li-Min, and Z. Xiangyang, "A survey on dielectric elastomer actuators for soft robots," *Bioinspiration & Biomimetics,* vol. 12, no. 1, p. 011003, 2017.

[52] N. Kellaris, V. Gopaluni Venkata, G. M. Smith, S. K. Mitchell, and C. Keplinger, "Peano-HASEL actuators: Muscle-mimetic, electrohydraulic transducers that linearly contract on activation," *Science Robotics,* vol. 3, no. 14, p. eaar3276, 2018.

[53] B. Yousef and S. Mohsen, "A Review of Ionic Polymeric Soft Actuators and Sensors," *Soft Robotics,* vol. 1, no. 1, pp. 38-52, 2014.

[54] C. S. Haines *et al.*, "Artificial Muscles from Fishing Line and Sewing Thread," *Science,* vol. 343, no. 6173, pp. 868-872, 2014.

[55] G. M. Spinks, "Stretchable artificial muscles from coiled polymer fibers," *Journal of Materials Research,* vol. 31, no. 19, pp. 2917-2927, 2016.

[56] S. E. Bakarich, R. Gorkin, M. in het Panhuis, and G. M. Spinks, "4D Printing with Mechanically Robust, Thermally Actuating Hydrogels," *Macromolecular Rapid Communications,* vol. 36, no. 12, pp. 1211-1217, 2015.

[57] H. Yuk, S. Lin, C. Ma, M. Takaffoli, N. X. Fang, and X. Zhao, "Hydraulic hydrogel actuators and robots optically and sonically camouflaged in water," *Nature Communications,* vol. 8, p. 14230, 2017.

[58] B. Shin *et al.*, "Hygrobot: A self-locomotive ratcheted actuator powered by environmental humidity," *Science Robotics,* vol. 3, no. 14, p. eaar2629, 2018.

[59] W. Hu, G. Z. Lum, M. Mastrangeli, and M. Sitti, "Small-scale soft-bodied robot with multimodal locomotion," *Nature,* vol. 554, pp. 81-85, 2018.

[60] N. W. Bartlett *et al.*, "A 3D-printed, functionally graded soft robot powered by combustion," *Science,* vol. 349, no. 6244, pp. 161-165, 2015.

[61] K. Suzumori, A. Wada, and S. Wakimoto, "New mobile pressure control system for pneumatic actuators, using reversible chemical reactions of water," *Sensors and Actuators A: Physical,* vol. 201, pp. 148-153, 2013.

[62] M. Wehner *et al.*, "An integrated design and fabrication strategy for entirely soft, autonomous robots," *Nature,* vol. 536, pp. 451-455, 2016.

[63] A. Miriyev, K. Stack, and H. Lipson, "Soft material for soft actuators," *Nature Communications,* vol. 8, no. 1, p. 596, 2017.

[64] J. I. Lipton, S. Angle, R. E. Banai, E. Peretz, and H. Lipson, "Electrically Actuated Hydraulic Solids" *Advanced Engineering Materials,* vol. 18, no. 10, pp. 1710-1715, 2016.

[65] R. Mutlu, G. Alici, M. in het Panhuis and G. Spinks, "3D Printed Flexure Hinges for Soft Monolithic Prosthetic Fingers", *Soft Robotics*, vol. 3, no. 3, pp. 120-133, 2016.

[66] M. Manti, T. Hassan, G. Passetti, N. D'Elia, C. Laschi, and M. Cianchetti, "A Bioinspired Soft Robotic Gripper for Adaptable and Effective Grasping," *Soft Robotics,* vol. 2, no. 3, pp. 107-116, 2015.

[67] C. Ching-Ping and B. Hannaford, "Measurement and modeling of McKibben pneumatic artificial muscles," *IEEE Transactions on Robotics and Automation,* vol. 12, no. 1, pp. 90-102, 1996.

[68] K. C. Galloway, P. Polygerinos, C. J. Walsh, and R. J. Wood, "Mechanically programmable bend radius for fiber-reinforced soft actuators," in *2013 16th International Conference on Advanced Robotics (ICAR)*, 2013, pp. 1-6.

[69] F. Connolly, P. Polygerinos, C. J. Walsh, and K. Bertoldi, "Mechanical Programming of Soft Actuators by Varying Fiber Angle," *Soft Robotics,* vol. 2, no. 1, pp. 26-32, 2015.

[70] M. Robertson, H. Sadeghi, J. Florez Marin, and J. Paik, "Soft Pneumatic Actuator Fascicles for High Force and Reliability," *Soft Robotics,* vol. 4, no. 1, pp. 23-32, 2017.

[71] O. Keiko, S. Wakimoto, K. Suzumori, and N. Yasutaka, "Micro pneumatic curling actuator - Nematode actuator," in *2008 IEEE International Conference on Robotics and Biomimetics*, 2009, pp. 462-467.

[72] G. Alici, T. Canty, R. Mutlu, W. Hu, and V. Sencadas, "Modeling and Experimental Evaluation of Bending Behavior of Soft Pneumatic Actuators Made of Discrete Actuation Chambers*", Soft Robotics*, vol. 5, no. 1, pp. 24-35, 2018.

[73] B. Mosadegh *et al.*, "Pneumatic Networks for Soft Robotics that Actuate Rapidly," *Advanced Functional Materials,* vol. 24, no. 15, pp. 2163-2170, 2014.

[74] S. Terryn, J. Brancart, D. Lefeber, G. Van Assche, and B. Vanderborght, "Self-healing soft pneumatic robots," *Science Robotics,* vol. 2, no. 9, p. eaan4268, 2017.

[75] E. W. Hawkes, L. H. Blumenschein, J. D. Greer, and A. M. Okamura, "A soft robot that navigates its environment through growth," *Science Robotics,* vol. 2, no. 8, p. eaan3028, 2017.

[76] J. D. Greer, T. K. Morimoto, A. M. Okamura, and E. W. Hawkes, "Series pneumatic artificial muscles (sPAMs) and application to a soft continuum robot," in *2017 IEEE International Conference on Robotics and Automation (ICRA)*, 2017, pp. 5503-5510.

[77] R. V. Martinez, C. R. Fish, X. Chen, and G. M. Whitesides, "Elastomeric Origami: Programmable Paper-Elastomer Composites as Pneumatic Actuators," *Advanced Functional Materials,* vol. 22, no. 7, pp. 1376-1384, 2012.

[78] A. Argiolas *et al.*, "Sculpting Soft Machines," *Soft Robotics,* vol. 3, no. 3, pp. 101-108, 2016.

[79] E. W. Hawkes, D. L. Christensen, and A. M. Okamura, "Design and implementation of a 300% strain soft artificial muscle," in *2016 IEEE International Conference on Robotics and Automation (ICRA)*, 2016, pp. 4022-4029.

[80] R. Niiyama, X. Sun, C. Sung, B. An, D. Rus, and S. Kim, "Pouch Motors: Printable Soft Actuators Integrated with Computational Design," *Soft Robotics,* vol. 2, no. 2, pp. 59-70, 2015.

[81] R. V. Martinez, A. C. Glavan, C. Keplinger, A. I. Oyetibo, and G. M. Whitesides, "Soft Actuators and Robots that Are Resistant to Mechanical Damage," *Advanced Functional Materials,* vol. 24, no. 20, pp. 3003-3010, 2014.

[82] E. Brown *et al.*, "Universal robotic gripper based on the jamming of granular material," *Proceedings of the National Academy of Sciences,* vol. 107, no. 44, pp. 18809-18814, 2010.

[83] M. A. Robertson and J. Paik, "New soft robots really suck: Vacuum-powered systems empower diverse capabilities," *Science Robotics,* vol. 2, no. 9, p. aan6357, 2017.

[84] S. Li, D. M. Vogt, D. Rus, and R. J. Wood, "Fluid-driven origami-inspired artificial muscles," *Proceedings of the National Academy of Sciences,* vol. 114, no. 50, pp. 13132-13137, 2017.

[85] D. Yang *et al.*, "Buckling Pneumatic Linear Actuators Inspired by Muscle," *Advanced Materials Technologies,* vol. 1, no. 3, p. 1600055, 2016.

[86] D. Yang, M. S. Verma, E. Lossner, D. Stothers, and G. M. Whitesides, "Negative-Pressure Soft Linear Actuator with a Mechanical Advantage," *Advanced Materials Technologies,* vol. 2, no. 1, p. 1600164, 2017.

[87] A. D. Marchese, R. K. Katzschmann, and D. Rus, "A Recipe for Soft Fluidic Elastomer Robots," *Soft robotics,* vol. 2, no. 1, pp. 7-25, 2015.

[88] G. Gerboni, A. Diodato, G. Ciuti, M. Cianchetti, and A. Menciassi, "Feedback Control of Soft Robot Actuators via Commercial Flex Bend Sensors," *IEEE/ASME Transactions on Mechatronics,* vol. 22, no. 4, pp. 1881-1888, 2017.

[89] K. Elgeneidy, N. Lohse, and M. Jackson, "Bending angle prediction and control of soft pneumatic actuators with embedded flex sensors – A data-driven approach," *Mechatronics,* vol. 50, pp. 234-247, 2018.

[90] J. T. Muth *et al.*, "Embedded 3D Printing of Strain Sensors within Highly Stretchable Elastomers," *Advanced Materials,* vol. 26, no. 36, pp. 6307-6312, 2014.

[91] J. C. Yeo, H. K. Yap, W. Xi, Z. Wang, C.-H. Yeow, and C. T. Lim, "Flexible and Stretchable Strain Sensing Actuator for Wearable Soft Robotic Applications," *Advanced Materials Technologies,* vol. 1, no. 3, p. 1600018, 2016.

[92] S. Kumbay Yildiz, R. Mutlu, and G. Alici, "Fabrication and characterisation of highly stretchable elastomeric strain sensors for prosthetic hand applications," *Sensors and Actuators A: Physical,* vol. 247, pp. 514-521, 2016.

[93] R. L. Truby *et al.*, "Soft Somatosensitive Actuators via Embedded 3D Printing," *Advanced Materials,* vol. 30, no. 15, p. 1706383, 2018.

[94] Y. Park, B. Chen, and R. J. Wood, "Design and Fabrication of Soft Artificial Skin Using Embedded Microchannels and Liquid Conductors," *IEEE Sensors Journal,* vol. 12, no. 8, pp. 2711-2718, 2012.

[95] W. Xi, J. C. Yeo, L. Yu, S. Zhang, and C. T. Lim, "Ultrathin and Wearable Microtubular Epidermal Sensor for Real-Time Physiological Pulse Monitoring," *Advanced Materials Technologies,* vol. 2, no. 5, p. 1700016, 2017.

[96] M. Stoppa and A. Chiolerio, "Wearable Electronics and Smart Textiles: A Critical Review," *Sensors,* vol. 14, no. 7, pp. 11957-11992, 2014.

[97] M. C. Lina and B. F. Alison, "Smart fabric sensors and e-textile technologies: a review," *Smart Materials and Structures,* vol. 23, no. 5, p. 053001, 2014.

[98] K. Elgeneidy, G. Neumann, M. Jackson, and N. Lohse, "Directly Printable Flexible Strain Sensors for Bending and Contact Feedback of Soft Actuators," *Frontiers in Robotics and AI,* vol. 5, p. 2, 2018.

[99] H. Mai, R. Mutlu, C. Tawk, G. Alici, and V. Sencadas, "Ultra-stretchable MWCNT–Ecoflex piezoresistive sensors for human motion detection applications," *Composites Science and Technology,* vol. 173, pp. 118-124, 2019.

[100] V. Sencadas, R. Mutlu, and G. Alici, "Large area and ultra-thin compliant strain sensors for prosthetic devices," *Sensors and Actuators A: Physical,* vol. 266, pp. 56-64, 2017.

[101] O. Atalay, A. Atalay, J. Gafford, and C. Walsh, "A Highly Sensitive Capacitive-Based Soft Pressure Sensor Based on a Conductive Fabric and a Microporous Dielectric Layer," *Advanced Materials Technologies,* vol. 3, no. 1, p. 1700237, 2018.

[102] L. Viry *et al.*, "Flexible Three-Axial Force Sensor for Soft and Highly Sensitive Artificial Touch," *Advanced Materials,* vol. 26, no. 17, pp. 2659-2664, 2014.

[103] L. Bin, G. Yang, F. Adam, and V. Yon, "Soft capacitive tactile sensing arrays fabricated via direct filament casting," *Smart Materials and Structures,* vol. 25, no. 7, p. 075009, 2016.

[104] A. Frutiger *et al.*, "Capacitive Soft Strain Sensors via Multicore–Shell Fiber Printing," *Advanced Materials,* vol. 27, no. 15, pp. 2440-2446, 2015.

[105] H. Zhao, K. O'Brien, S. Li, and R. F. Shepherd, "Optoelectronically innervated soft prosthetic hand via stretchable optical waveguides," *Science Robotics,* vol. 1, no. 1, p. eaai7529, 2016.

[106] K. Kong and M. Tomizuka, "A Gait Monitoring System Based on Air Pressure Sensors Embedded in a Shoe," *IEEE/ASME Transactions on Mechatronics,* vol. 14, no. 3, pp. 358-370, 2009.

[107] H. Yang, Y. Chen, Y. Sun, and L. Hao, "A novel pneumatic soft sensor for measuring contact force and curvature of a soft gripper," *Sensors and Actuators A: Physical,* vol. 266, pp. 318-327, 2017.

[108] H. Choi, P. Jung, K. Jung, and K. Kong, "Design and fabrication of a soft three-axis force sensor based on radially symmetric pneumatic chambers," in *2017 IEEE International Conference on Robotics and Automation (ICRA)*, 2017, pp. 5519-5524.

[109] D. Gong, R. He, J. Yu, and G. Zuo, "A Pneumatic Tactile Sensor for Co-Operative Robots," *Sensors,* vol. 17, no. 11, p. 2592, 2017.

[110] R. Slyper and J. Hodgins, "Prototyping robot appearance, movement, and interactions using flexible 3D printing and air pressure sensors," in *2012 IEEE RO-MAN: The 21st IEEE International Symposium on Robot and Human Interactive Communication*, 2012, pp. 6-11.

[111] M. Vázquez *et al.*, "3D Printing Pneumatic Device Controls with Variable Activation Force Capabilities," in *33rd Annual ACM Conference on Human Factors in Computing Systems*, 2015, pp. 1295-1304.

[112] C. Schumacher, B. Bickel, J. Rys, S. Marschner, C. Daraio, and M. Gross, "Microstructures to control elasticity in 3D printing," in *ACM Trans. Graph.,* vol. 34, no. 4, pp. 1-13, 2015.

[113] O. D. Yirmibesoglu *et al.*, "Direct 3D printing of silicone elastomer soft robots and their performance comparison with molded counterparts," in *2018 IEEE International Conference on Soft Robotics (RoboSoft)*, 2018, pp. 295-302.

[114] T. Kalisky *et al.*, "Differential pressure control of 3D printed soft fluidic actuators," in *2017 IEEE/RSJ International Conference on Intelligent Robots and Systems (IROS)*, 2017, pp. 6207-6213.

[115] X. Noblin, N. O. Rojas, J. Westbrook, C. Llorens, M. Argentina, and J. Dumais, "The Fern Sporangium: A Unique Catapult," *Science,* vol. 335, no. 6074, pp. 1322-1322, 2012.

[116] C. Llorens, M. Argentina, N. Rojas, J. Westbrook, J. Dumais, and X. Noblin, "The fern cavitation catapult: mechanism and design principles," *Journal of The Royal Society Interface,* vol. 13, no. 114, p. 20150930, 2016.

[117] R. Moreno, "Fern sporangia," *Flickr,* 2015.

[118] M. Manti, V. Cacucciolo, and M. Cianchetti, "Stiffening in Soft Robotics: A Review of the State of the Art," *IEEE Robotics & Automation Magazine,* vol. 23, no. 3, pp. 93-106, 2016.

[119] R. Deimel and O. Brock, "A novel type of compliant and underactuated robotic hand for dexterous grasping," *The International Journal of Robotics Research,* vol. 35, no. 1-3, pp. 161-185, 2016.

[120] J. Fraś, M. Maciaś, F. Czubaczyński, P. Sałek, and J. Główka, "Soft Flexible Gripper Design, Characterization and Application," in *Recent Advances in Systems, Control and Information Technology*, 2017, pp. 368-377.

[121] J. Zhou, S. Chen, and Z. Wang, "A Soft-Robotic Gripper With Enhanced Object Adaptation and Grasping Reliability," *IEEE Robotics and Automation Letters,* vol. 2, no. 4, pp. 2287-2293, 2017.

[122] Y. Hao *et al.*, "Universal soft pneumatic robotic gripper with variable effective length," in *2016 35th Chinese Control Conference (CCC)*, 2016, pp. 6109-6114.

[123] P. Glick, S. A. Suresh, D. Ruffatto, M. Cutkosky, M. T. Tolley, and A. Parness, "A Soft Robotic Gripper With Gecko-Inspired Adhesive," *IEEE Robotics and Automation Letters,* vol. 3, no. 2, pp. 903-910, 2018.

[124] A. K. Mishra, E. Del Dottore, A. Sadeghi, A. Mondini, and B. Mazzolai, "SIMBA: Tendon-Driven Modular Continuum Arm with Soft Reconfigurable Gripper," *Frontiers in Robotics and AI,* vol. 4, p. 4, 2017.

[125] R. R. Ma, L. U. Odhner, and A. M. Dollar, "A modular, open-source 3D printed underactuated hand," in *2013 IEEE International Conference on Robotics and Automation (ICRA)*, 2013, pp. 2737-2743.

[126] F. Chen *et al.*, "Topology Optimized Design, Fabrication, and Characterization of a Soft Cable-Driven Gripper," *IEEE Robotics and Automation Letters,* vol. 3, no. 3, pp. 2463-2470, 2018.

[127] R. Deimel and O. Brock, "A compliant hand based on a novel pneumatic actuator," in *2013 IEEE International Conference on Robotics and Automation (ICRA)*, 2013, pp. 2047-2053.

[128] H. Zhang, A. S. Kumar, J. Y. H. Fuh, and M. Y. Wang, "Topology optimized design, fabrication and evaluation of a multimaterial soft gripper," in *2018 IEEE International Conference on Soft Robotics (RoboSoft)*, 2018, pp. 424-430.

[129] L. U. Odhner *et al.*, "A compliant, underactuated hand for robust manipulation," *The International Journal of Robotics Research,* vol. 33, no. 5, pp. 736-752, 2014.

[130] Honeywell Sensing and Internet of Things, 2019.

[131] C. L. Semasinghe, D. G. K. Madusanka, R. K. P. S. Ranaweera, and R. A. R. C. Gopura, "Transradial prostheses: Trends in development of hardware and control systems," *The International Journal of Medical Robotics and Computer Assisted Surgery,* vol. 15, no. 1, p. e1960, 2019.

[132] H. Zhou, A. Mohammadi, D. Oetomo, and G. Alici, "A Novel Monolithic Soft Robotic Thumb for an Anthropomorphic Prosthetic Hand," *IEEE Robotics and Automation Letters,* vol. 4, no. 2, pp. 602-609, 2019.